January 2020

# The Influence Of High Intensity Turbulence And Secondary Flows On Slot Film Cooling Over An Aft Loaded Vane

Loren Soma

# THE INFLUENCE OF HIGH INTENSITY TURBULENCE AND SECONDARY FLOWS ON SLOT FILM COOLING OVER AN AFT LOADED VANE

by

Loren Wesley Soma
Bachelor of Science, North Dakota State University, 2009
Master of Science, North Dakota State University, 2011

A Dissertation

Submitted to the Graduate Faculty

of the

University of North Dakota

In partial fulfillment of the requirements

for the degree of

Doctor of Philosophy

Grand Forks, North Dakota

December
2020

Name: Loren W. Soma

Degree: Doctor of Philosophy

This document, submitted in partial fulfillment of the requirements for the degree from the University of North Dakota, has been read by the Faculty Advisory Committee under whom the work has been done and is hereby approved.

DocuSigned by:
Dr. Forrest Ames
3536B543AC3C48C...
Dr. Forrest Ames

DocuSigned by:
Clement Tang
86F84C3C25CE48C...
Dr. Clement Tang

DocuSigned by:
Dr. krishnamoorthy Gautham
A40697C554F347C...
Dr. Krishnamoorthy Gautham

DocuSigned by:
Bora Suzen
BB825705F996430...
Dr. Bora Suzen

DocuSigned by:
Howe Lim
E2D755C3824A4F5...
Dr. Howe Lim

This document is being submitted by the appointed advisory committee as having met all the requirements of the School of Graduate Studies at the University of North Dakota and is hereby approved.

DocuSigned by:
Chris Nelson
2E0AF088C733403...
Chris Nelson
Dean of the School of Graduate Studies

12/3/2020
Date

PERMISSION

Title THE INFLUENCE OF HIGH INTENSITY TURBULENCE AND SECONDARY FLOWS ON SLOT FILM COOLING OVER AN AFT LOADED VANE

Department Mechanical Engineering

Degree Doctor of Philosophy

In presenting this dissertation in partial fulfillment of the requirements for a graduate degree from the University of North Dakota, I agree that the library of this University shall make it freely available for inspection. I further agree that permission for extensive copying for scholarly purposes may be granted by the professor who supervised my dissertation work or, in his absence, by the chairperson of the department or the dean of the Graduate School. It is understood that any copying or publication or any other use of this dissertation or part thereof for financial gain shall not be allowed without my written permission. It is also understood that due recognition shall be given to me and to the University of North Dakota in any scholarly use which may be made of any material in my dissertation.

Loren W. Soma
November 2020

TABLE OF CONTENTS

LIST OF FIGURES

Figure Page

LIST OF TABLES

# NOMENCLATURE

| | |
|---|---|
| Cp | specific heat at constant temperature, kJ/(kg*K) |
| d | coolant hole diameter, m |
| D | leading edge cylinder diameter, m |
| h | convective heat transfer coefficient, W/($m^2$*K) |
| I | electrical current, amps |
| k | thermal conductivity, W/m/K |
| L | hole length, m |
| Lu | energy scale, $Lu = 1.5u'^3/\varepsilon$ |
| Lx | integral length scale, m |
| M | blowing ratio based on the combined area of hole minimum diameter , $\rho_c U_c/\rho_\infty U_\infty$ |
| Nu | Nusselt number; dimensionless number, ratio of convective heat transfer to conductive heat transfer, Nu=hDk |
| p | pitch or spanwise hole spacing, m |
| P | pressure, Pa |
| Pr | Prandtl number; dimensionless number, ratio of viscous diffusion rate to thermal diffusion rate, $Pr=C_p\mu k$ |
| q" | heat flux, kJ per unit time per unit area |
| R | resistance; ohms, Ω |

$Re_C$ Chord Reynolds number; dimensionless number, ratio of inertial forces to viscous forces, $Re_C = \rho U_C/\mu$

$Re_D$ Diameter Reynolds number; dimensionless number, ratio of inertial forces to viscous forces, $Re_D = \rho U_\infty/\mu$

S space between rows, m

St Stanton number; dimensionless number, ratio of heat transferred to a fluid over the thermal capacity of the fluid, $St = h/\rho C p U_{ex}$

T Temperature, K

$T_R$ Recovery Temperature, K

Tu turbulence intensity, Tu = |u'|/U∞

U velocity, m/s

## Greek Letter Symbols

α Inclination or injection angle, degrees

β Lateral expansion angle, degrees

Δ Delta, difference

ε turbulent dissipation, $m^2/s^3$

η Adiabatic effectiveness

μ Absolute viscosity, Pa*s

ν Kinematic viscosity, $m^2/s$

ρ Rho; fluid density, mass per unit of volume, $kg/m^3$

Subscripts

| | |
|---|---|
| ac | refers to the air conditioner |
| atm | refers to atmospheric conditions |
| aw | adiabatic wall |
| AW | adiabatic wall |
| brkt | refers to the mounting bracket |
| co | coolant out |
| cw | cooled wall |
| D | diameter |
| ex | refers to exit conditions |
| in | refers to inlet conditions |
| orf | refers to the orifice |
| out | refers to outlet conditions |
| plen | refers to the plenum |
| R | recovery |
| s | refers to static conditions |
| PS1 | suction surface slot |
| SS1 | upstream suction surface slot |
| SS2 | middle suction surface slot |
| SS3 | aft suction surface slot |
| t | refers to total conditions |
| $\infty$ | evaluated in the free stream |

# ACKNOWLEDGEMENTS

The help of several people has made this project possible. I would like to thank the University of North Dakota Mechanical Engineering Department for providing me the opportunity to continue my studies in the graduate program. I would also like to thank Dr. Ames for advising me throughout this project. The knowledge and guidance he provided during my graduate career at UND was very important to me and supremely appreciated. Thank you also to my advisory committee members, Dr. Nanak Grewal, Dr. Clement Tang, Dr. Krishnamoorthy Gautham, Dr. Yildirim Suzen, Dr. Howe Lim and Dr. Nels Forsman. Many thanks to the National Energy Technology Laboratory (NETL), the Department of Energy, and the University Turbine Systems Research (UTSR) program for providing the funding for this work.

Fellow graduate students Abdulqadir Sheikhmohamed, Justin Varty, and Maliha Yelmahi deserve a great deal of gratitude for their knowledge and assistance. Additionally, undergraduate students Zachariah Dean, Forrest Langseth, Wilson Lysford, Andrey Baydak, and Michael McShane contributed human-power and insight, which merits acknowledgment. For assistance and guidance with the fabrication of components for this project, I would also like to thank Jay Evenstad and my father David Soma. Thank you also to Kristie Wolff and Pamela Burkes for your administrative help.

To my wife Lashonda and my daughters Zora and Mila,
You are my world!

# ABSTRACT

The purpose of this study is to experimentally investigate the effects of high turbulence and secondary flows on slot film cooling over an aft loaded vane (turbine blade) with a large leading edge. Turbine nozzle component cooling methods are challenged by very high combustor discharge temperatures, turbulence effects, and high acceleration requiring cooling methods to provide reliable and acceptable component life. Throughout the development of gas turbines, film cooling has become one of the most prevalent techniques to protect high pressure turbine airfoils and endwalls. Film cooling works by supplying a film of cooler than the freestream gas onto the external surface through internal means without significantly increasing turbulence or capturing hot freestream gas. Unfortunately, leading edge and pressure surface film cooling is susceptible to particulate deposition and clogging [1] which slot film cooling is known to significantly mitigate [2]. Understanding the influence of secondary flows in sweeping away film cooling coverage is also important in developing a reliable cooling design.

This study investigates a vane designed to be resistant to particulate deposition while providing a highly effective and efficient cooling method. An internal cooling scheme was implemented instead of showerhead cooling arrays in the leading-edge region and shaped holes on the pressure surface, both of which are susceptible to clogging due to particulates in the fuel or air. To accommodate for the internal cooling method, the leading-edge region must be designed with more room; a characteristic that

also helps to reduce the leading-edge heat transfer coefficient [3]. Conventionally, the spent internal coolant air is discharged from the vane in a way that can be detrimental to external cooling mechanisms. However, the present approach is to collect the spent internal flow and use it for slot film cooling, a near optimum cooling method which has also been found to be tolerant to particulate deposition. Additionally, film cooling studies have discovered that acceleration inhibits mixing and delays laminar to turbulent transition which enhances the resulting film cooling effectiveness. Conversely, acceleration also inhibits boundary layer growth which contributes to aerodynamic losses. Accordingly, this study uses an aft loaded vane which accelerates the flow over most of the suction surface.

Film cooling distributions were acquired in UND's large scale low speed cascade wind tunnel facility. Relevant inlet turbulence conditions were generated using grids or simulated aerocombustors. Two vanes were constructed and tested over a range of Reynolds numbers; one for the pressure side measurements and one for the suction side measurements. Vane film cooling locations are consistent with modern vane cooling application. Cooling air for each slot was fed by individual plenums with controls to measure and regulate film cooling blowing ratios. The film cooling supply and measurement system consisted of an existing blower, heat exchanger, a window air conditioning unit, a thermal inertia system, and an orifice tube for each plenum. Flow from the blower was directed into a duct connected to the evaporator of the air conditioning unit. A similar duct was connected to the exit of the evaporator and directed air into the thermal inertia system. The thermal inertia system consists of stacked aluminum plates spaced to allow air to flow in between the plate surfaces. The purpose of

the thermal inertia box is to keep the cooling air supply temperature constant during the experiment.

The study has been well documented and analyzed for further development of predictive models. The comprehensive film cooling database generated in this study has improved our understanding of the influence of turbulence and secondary flows on film cooling. This work will be highly useful in grounding high fidelity computational methods and help cooling system designers implement slot cooling throughout the industry.

# CHAPTER I

# INTRODUCTION

The desire for more efficient power generation grows with the world's increasing thirst for energy. Higher efficiencies in gas turbines, in part, are achieved by having higher turbine inlet temperatures, and accordingly, turbine vanes must be capable of withstanding higher temperatures. Even with the use of high-tech ceramic coatings and alloys, high temperature thresholds are reached in the pursuit of higher efficiencies and advanced cooling schemes must be developed. The goal is to produce maximum efficiencies by reaching higher temperatures without damaging the structural integrity of the vane. In industry, film cooling in the nozzles of gas turbines is a common method to maintain the temperatures below material temperature limits.

Conventionally, film cooling is employed with showerhead cooling in leading edge region and rows of shaped holes on the pressure side of the vanes in the first stage [3]. Film cooling works by supplying cooler than the freestream gas onto the external surface through internal means without significantly increasing turbulence or capturing hot freestream gas. Though traditional film cooling methods satisfy surface cooling criteria, they often face challenges due to clogging. Slot cooling is a method that is proven to significantly reduce deposition of particulates downstream and in the region of the slot [2]. Until recently, due to structural considerations, slot cooling in turbine blades has usually been reserved for downstream of the pressure side cutback. Contemporarily,

the emergence of high solidity double walled internal cooling designs is providing mechanical integrity to accommodate slots throughout the vane [1]. Internal cooling involves flow of cooling air through passages inside each vane prior to discharge usually near the trailing edge [4], which is less than ideal use of spent cooling air. Vane shape also influences surface heat loads and secondary flows. Although leading edge regions are typically laminar, the heat load can be high especially at moderate to low chord Reynolds numbers. It is less of an issue at higher Reynolds numbers as turbulent region heat transfer grows at $Re^{0.8}$ and laminar at $Re^{0.5}$. Leading edge regions of vanes also have a low coolant supply to local surface static pressure ratio, which drives the cooling method. In addition to allowing for more double wall internal cooling and slot cooling access, a broader leading-edge produces lower surface heat loads. The logical approach is to design large leading edge aft loaded vane with slot film cooling using spent cooling gas from double wall internal cooling. Understanding the influence of "high" intensity turbulence and secondary flows for this type of vane geometry is necessary to maximize this design and is the topic of this research.

The development of engineering models to predict heat loads has improved the understanding of boundary layer development on. A recent numeric study using Large Eddy Simulations (LES) by Kanani et al. [4] was conducted to obtain a "better understanding of the flow physics and heat transfer" of slot film cooling under conditions corresponding experimental measurements of Busche et al. [1] The experimental and numeric results corresponded well, showing increased decay of film cooling effectiveness with higher turbulence intensities. Similarly, this study is expected to correlate untested numeric models and previous work by Varty and Ames [3] which characterized heat

transfer distributions over an aft loaded vane with a large leading edge at very high turbulence levels, with the absence of cooling schemes. Varty's vane was subjected to high levels of simulated combustor turbulence, which significantly enhanced the stagnation region heat transfer, augmented laminar heat transfer downstream, and caused early transition on the suction surface. With the addition of slot film cooling, this research subjects Varty's airfoil geometry to similar turbulence intensities and slot film cooling blowing ratios used by Busche and Ames [1]. The goal is to use collected data to characterize heat distributions and cooling effectiveness levels for comparison to the uncooled model and numerical simulations.

Objectives of research. This research is designed to examine the influence of high intensity turbulence and secondary flows on slot film cooling over an aft loaded vane. The goal is to produce methods of lowering surface heat transfer loads. Also, this research addresses how realistic internal cooling geometries influence slot film cooling distributions. Additionally, the influence of Reynolds number and film cooling jet to free-stream blowing (mass flux) ratio on surface heat transfer distributions will be investigated.

# CHAPTER II

# LITERATURE REVIEW

Nearly 60 years ago, film cooling was introduced as a practical way to allow for higher turbine inlet temperatures that ultimately lead to higher turbine efficiencies. The desire to improve film cooling methods has been researched extensively since implementation; thus, a large literature base of film cooling studies exists. Additionally, many variables affect film cooling performance and structural viability. Therefore, the scope of this chapter will focus on shaped hole film cooling, slot film cooling, and the effects of turbulence intensity as it pertains to this study.

By in large, round hole film cooling has been the industrial standard as it is the least costly to implement. However, it is often outperformed by other geometries and is susceptible to particulate clogging. Continuous two-dimensional (2D) slot geometry is preferred as it performs well and is less susceptible to clogging. Unfortunately, by incorporating a slot into a vane design, the structural integrity is often comprised to the point at which it is no longer viable during operation. Slot cooling performance is nearly matched by shaped holes without sacrificing as much strength, but the manufacturing cost is large and the hole shapes are still vulnerable to particulate clogging. High turbulence exists in the first stage of turbines, providing increased heat transfer and decreased adiabatic effectiveness. Leading edge heat transfer levels are lower on vanes with a large leading edge when compared to vanes with a smaller leading edge [3].

Recently, Varty and Ames designed a vane with a large enough area in the leading edge to allow for internal cooling using a double wall cooling design which additionally provides the structural support for 2D slot film cooling [3].

## Slot and Round Hole Film Cooling

Ideal film cooling is achieved by dispersing coolant across the entire surface it is intended to cool utilizing a 2D continuous slot perpendicular to the direction of mainstream flow. This continuous slot method produces challenges: low flow resistance leads to harder to control flow rates, and lack of structure lends itself to mechanical failure [5]. The goal of the current study is to integrate slot film cooling, that does not sacrifice strength, instead of showerhead cooling arrays in the leading-edge region and shaped holes on the pressure surface to accomplish adiabatic effectiveness levels.

In a previous study at the UND, the effects of increasing free-stream turbulence on a 2D slot film cooling scheme in an accelerating boundary layer was examined by Busche et al. [1]. For comparison in a later chapter, flow conditions for this this study conditions were set to closely match their study. At a given blowing ratio (M), Busche et al. found adiabatic effectiveness levels to essentially order on turbulence. In almost every scenario, they noted an increase in effectiveness when blowing ratios were increased. For increases in turbulence intensity, their study showed a moderate increase in heat transfer which they attributed to earlier transition.

Bunker [6] investigated mesh-fed slot film cooling as a method to produce a more structurally sound means to implement slot film cooling. Bunker's mesh-fed slot consisted of an array of pedestals with height/diameter ratios of 0.2 followed by 20° inclines prior to discharge at surface. The pedestals improved strength and caused

mixing to increase flow uniformity. When compared to a row of shaped holes, the mesh-fed slot film cooling outperformed by 25% in the near slot region and by 100% in the downstream region. In the present study, each coolant slot includes 3 rows of pedestals prior to a 30° incline prior to discharge to emulate these effects.

Simon [7] developed equations based on turbulence intensity, temperature, and flow to predict slot film cooling efficiency. His model consisted of an initial region with the potential for highly efficient film cooling, and a fully developed region where the coolant and the free-stream fluid are completely mixed. With his equations, Simon calculated values within 4% of experimental results.

Discrete hole film cooling remains the most widely used geometry despite not the most effective film cooling geometry. Consequently, there has been many studies conducted to improve this type of film cooling. Exploring several articles related to the subject of density ratio effect on discrete hole film cooling, L'Ecuyer and Soecthing [8] noticed the occurrence of three distinct regimes and centered them on velocity ratio. At a given injection angles, below velocity ratios of 0.25, in the mass addition regime, effectiveness levels rise due to greater coolant thermal capacity. The mixing regime occurs at velocity ratios between 0.25 and 0.8, where effectiveness levels are affected by the contrasting mechanisms of added mixing and increased coolant thermal capacity. Coolant jets penetrate the free-stream flow and increase turbulent diffusion of the coolant in the penetration regime, which exists above a velocity ratio of 0.8. Using data from Pederson et al [9], who examined density ratios extensively, L'Ecuyer and Soecthing developed a correlation for discrete hole cooling performance. They discovered cooling effectiveness at a given blowing ratio is impacted by density ratio, which is attributed to

differences in normal momentum. A similar study by Sinha et al. [10] produced comparable results. In their study, jet detachment and reattachment grew with momentum flux ratio and became more critical at higher blowing ratios. Reduced coolant spreading is associated with lower density ratios and higher momentum flux ratios and thus, reduced spanwise effectiveness.

Cooling effectiveness was characterized with pressure sensitive paint in previous experimental research by Liu et al. [11]. During testing, the pressure and suction side of a vane was exposed to several momentum flux ratios, density ratios, turbulence intensities, and blowing ratios. Though turbulence was shown to be detrimental in all situations, the results showed improved cooling effectiveness with higher blowing ratios for both the suction side and higher density ratios for the suction side.

The effects of modifying injection angle, hole spacing, and upstream boundary layer thickness were explored by Foster and Lampard [12]. Their models consisted of a single row of round holes. They found improved cooling effectiveness as injection angles where increased at higher blowing ratios and lower injection angles at low blowing ratios. Lateral mixing near the wall and jet penetration were augmented as the boundary layer levels were amplified, which provided for reduced cooling effectiveness. Improved coolant coverage was observed when spacing was decreased, which was also contributed to diminished jet detachment.

Leiss [13] discovered cooling effectiveness significantly decreased as displacement thickness was elevated in a study examining a flat plate with a single row of round injection holes. During his studies, he compared displacement thickness to hole diameter ratios ($\delta^*/d$) ratios at numerous pressure gradients. At higher $\delta^*/d$ ($> 0.2$) he

found a precipitous drop in cooling effectiveness even though there was no considerable change in other heat transfer measurables. He also found sizable reductions in effectiveness produced at smaller blowing ratios under a favorable pressure gradient. Qin et al. [14] also found strong favorable pressure gradients to lead to higher cooling effectiveness when he performed similar studies on convex surfaces

To predict overall film cooling effectiveness, Muska et al. [15] developed a method using superposition on successive rows of cylindrical ejection holes. They added the test results from different sets of hole sizes together to emulate an array of previously tested arrangements. The results correlated well with previous empirical data and mathematical modeling for cooling slots as well as different configurations of rows of holes. Validating the superposition approach has allowed researchers to predict the behavior of many film cooling arrangements with only the testing of few configurations as long as the fluid dynamics of the flow remains largely unchanged.

## Shaped Hole Film Cooling

Extensive research has been conducted to optimize the size and shape of film cooling holes. Manipulating these features to the design of a particular turbine blade can be highly beneficial [16].

Comparing cylindrical to shaped cooling holes, Laveau and Abhari [17] focused on vortical structures. Their studies display round holes having vortical structures with four times the magnitude of shaped holes. The higher momentum flux ratios for round holes suggests higher levels of jet lift-off and jet penetration which a detrimental to in film cooling.

A synopsis of a career worth of study on this subject is provided in "A Review of Shaped Hole Turbine Film Cooling Technology" by Bunker [18]. He suggested the momentum flux of the coolant can be reduced by having shaped holes with diverging exits. This type of geometry acts as a diffuser, slowing down the cooling air to limit penetration into the boundary layer. Divergent holes may also enhance coolant coverage as the air passing through can more easily spread spanwise. However, too much diffusion can be detrimental if produces excess free-stream mixing, which reduces downstream effectiveness. Diffusing designs, such as “fan” and “laid back” shaped holes, produce an anti-kidney flow structures that has the converse momentum effect of jet-like flow structure produced by round coolant holes. Unfortunately, these shaped holes are known to cause separation of the coolant layer leading to the degradation of downstream effectiveness. In another article by Bunker, the high cost and challenging manufacturing processes are mentioned as barriers to more wide spread use of shaped cooling holes [19]. Shaped holes are known cost more than quadruple the price of cylindrical holes.

Angled fan shaped holes, fan shaped holes, discrete holes and discrete slots, among other coolant passage geometries, were analyzed by Dittmar et al. [20] by looking at spanwise averaged effectiveness. At the lowest blowing ratios, the performance of fan shaped holes was marginally better than the other geometries. Conversely, after the blowing ratio was increased to an intermediate level, the advantage of fan shaped holes over round holes became much clearer. Also, past approximately 10 hole diameters distance streamwise, the discrete slots surpassed the effectiveness all other geometries tested. Additionally, they noticed the discrete slots did not display the type of jet

separation that discrete shaped holes are known for which was attributed to the coolant remaining closer to the vane surface. This effect allows for much higher downstream effectiveness values.

In a shaped cooling hole study by Saumweber and Schulz [21] , the cooling performance was analyzed while changing lateral expansion angle, injection angle, and hole length. A broader spread of coolant was achieved by increasing the expansion angle; however, the cooling performance improvement was limited due to the formation of a separation bubble that causes a fork-shaped cooling pattern. This fork shaped pattern was found to be mitigated by increasing the hole length to diameter ratio by a magnitude of 1.67. Smaller blowing ratios displayed little change in effectiveness when the inclination angle was varied. Conversely, a large difference in effectiveness was noted when the inclination angle was changed at intermediate to high blowing ratios. When comparing cylindrical and shaped holes, they found effectiveness trends in opposite directions when inclination angle is changed. The performance of diffusion shaped holes over cylindrical holes increased by factor of 1.3 to 1.5 according to research by Yu et al. [22]. In a comparable study on endwall cooling, Colban et al. [23] attained similar outcomes.

In another research project by Saumweber and Schulz [24], an additional row of fan shaped or cylindrical holes was added at assorted increments downstream of the first row. Downstream performance was largely dependent on the flow parameters of the most aft row while downstream effectiveness was significantly improved by increasing coolant through the first row of holes.

Brauckmann and Wolfersdorf [25] discovered a negligible impact on adiabatic effectiveness when varying the compound angle for a row of fan shaped film cooling holes. However, at high blowing ratios they found a significant rise in heat transfer values much further downstream (20 hole diameters) which they attributed to mixing via jet interactions with the free stream.

Colban et al. [26] constructed a complete model of a stationary vane with showerhead and fan-shaped film cooling holes. They conducted a series of tests on the vane with coolant passing through both cooling mechanisms and with the fan shaped holes only. The vane was designed with aggressive curvature which is thought to have caused the notable separation observed on the suction side of the vane. Showerhead cooling contributed modest gains in cooling effectiveness on the concave pressure side of the vane, which would largely be considered negligible in most applications. Overall, the immoderate curvature of the vane design resulted in a harsh cooling challenge. Mhetras et al. [27] tested a vane with a similar set up. The coolant film decomposed much slower on the suction side when jet detachment was not present.

After a copious review of shaped hole geometries, Schroeder and Thole [28] developed a "baseline" hole for future researchers and designers alike. With a 30° inclination angle, 7° layback, and 7° lateral expansion, this "baseline" hole eliminates in-hole separation and permits much higher blowing ratios with not risk of jets detaching.

## Effects of Turbulence

Throughout the years, gas turbines have been produced in all sorts of shapes and sizes to meet their intended purposes. Accordingly, the flow characteristics have varied depending on the type of engine and operating conditions. However, some traits are

common regardless of design. This is the case with turbulence intensity, which tends to peak in the primary zone of the combustor. High turbulence intensity values are known drive up heat transfer values and decrease adiabatic effectiveness.

Free-stream turbulence effects on both round and shaped cooling holes were examined in two studies by Saumweber and Schulz [29] and Saumweber et al. [30]. Surprisingly, both studies suggested only a slight advantage when shaped hole designs were subjected to higher turbulence intensities. Additionally, at higher blowing ratios turbulence intensity was shown to actually improve effectiveness, which was attributed to an increase in fluid mixing that corrals some coolant back towards the vane surface. Consequently, the shaped cooling hole performance was always shown to be detrimentally effected by higher intensities. Nevertheless, shaped holes always outperformed round holes in every scenario.

Meyhew et al. [31] studied the effects of turbulence on a three-hole flat plate with with a 3 to 1 spacing to holes diameter ratio. Using liquid crystal thermography with blowing ratios set to 0.5, 1.0 and 1.5, they found the two former settings to display a decrease effectiveness at high free-stream turbulence while the latter proved to increase spanwise coverage. Building on this study, Mayhew et al. [32] examined heat transfer under the same test conditions. The results of this study showed higher heat transfer values with elevated levels of turbulence for all blowing ratios. They also noted better heat transfer values for sets of holes as opposed to singular holes. This effect was attributed to strengthening effect of the kidney vortices caused by having holes adjacent to each other.

Ames has experimentally studied vane cooling schemes extensively. In a series of his studies [33] [34] he examined single and double rows of film cooling holes exposed to high (12.4%) and low (0.09%) levels of turbulence. The influence of turbulence on the pressure side of the experimental vane was found to be much greater than on the suction side. Characterizing the effects of turbulence on showerhead cooling, Cutbirth and Bogard [35] tested a vane at turbulence intensities set to 20%. Their trends were the same as the studies by Ames with and without film cooling applied.

In a study characterizing the effects of turbulence on film cooling at several blowing ratios, Mayhew et al. [36] observed the flow structure of the vortices breaking down behind cooling holes to transition from double to single counter-rotating vortices. Their results displayed lower and higher effectiveness at lower and higher blowing ratios, respectively.

Wright et al. [37] studied the effects of turbulence on film cooling with a row of fan-shaped cooling holes. Unlike the results of Meyhew's study, they noticed the flow structure maintaining its integrity at higher turbulence intensities, thus helping to shield the vane surface from the hotter free-stream air. This behavior was noted over a wide range of turbulence intensities suggesting fan-shaped holes are a very robust geometry for film cooling applications. A very comparable study by Davidson et al. [38] echoed these results. Maintaining the vortex structure of the cooling air adjacent to the vane wall limits the interaction between the free-stream and the vane surface. This feature is decisive advantage for selecting fan-shaped holes over other film cooling hole geometries

# CHAPTER III

# EXPERIMENTAL APPROACH

The University of North Dakota's large-scale low-velocity cascade wind tunnel facility and the experimental procedures used to acquire film cooling effectiveness measurements are described in the present chapter.

An aft loaded large leading edge vane geometry configured in the linear cascade was subjected to a myriad of turbulence intensities inside of a cascade wind tunnel. Two scaled model vanes with identical surface profiles were fitted with slot cooling inserts to simulate the film cooling geometry on the leading edge of a first stage vane or blade. The inserts provided a path for cooling air to be supplied from the exterior of the test section to the inside of the vane and finally onto the surface of the vane through a film cooling slot. The "Pressure Side" vane had one film cooling slot placed on the pressure side of the vane while the "Suction Side" vane had three film cooling slots placed on the suction side of the vane. Five well documented turbulence intensities ranging from 0.7% to 13.7% were implemented on the pressure side test surface at exit chord Reynolds numbers of .5, 1 and 2 million and cooling air blowing ratios of M = 0.4, .7, and 1.0. With three film cooling slots, the suction side test surface had a much more complex test scheme, which is noted in Table **1**. Using four of the same turbulence intensities, the suction side test vane was subjected to as many as ten different blowing ratio

configurations with exit chord Reynolds numbers again set to 500,000, 1,000,000 and 2,000,000.

Table 1. Suction Surface Blowing Ratio Combinations.

| Blowing Ratio Combination # | Slot 1 (M) | Slot 2 (M) | Slot 3 (M) |
|---|---|---|---|
| 1 | 0.50 | 0.15 | 0.15 |
| 2 | 0.50 | 0.30 | 0.30 |
| 3 | 1.00 | 0.15 | 0.15 |
| 4 | 1.00 | 0.30 | 0.30 |
| 5 | 0.50 | 0.00 | 0.00 |
| 6 | 0.00 | 0.15 | 0.00 |
| 7 | 0.00 | 0.00 | 0.15 |
| 8 | 1.00 | 0.00 | 0.00 |
| 9 | 0.00 | 0.30 | 0.00 |
| 10 | 0.00 | 0.00 | 0.30 |

Low-Velocity Cascade Wind Tunnel

The University of North Dakota's large-scale low-velocity cascade facility was originally developed by Dr. Forrest Ames and has been continually updated by him and his graduate students. Over the years it has been utilized for experimental research to acquire heat transfer and other aerodynamic measurements related to gas turbine cooling schemes. From right to left, the facility components can be viewed in Figure 1: a filter box, a large blower, diffusers, a heat exchanger, a flow mixer and flow straightener, a flow conditioning section, a series of nozzles, and the test section that contains the film cooling test vane in a linear cascade.

Before entering the wind tunnel, air is entrained through a filter box containing eight Air Handler 6B640 industrial air filter to prevent particulates from reaching the test surface that may lead to erroneous data readings. Measuring 60.96 cm x 60.96 cm (24 in

x 24 in), these filters rated at 95% filtering efficiency. After the filter box, a New York Blower 274-AF is installed. The blower is capable of pushing 6.6 $m^3/s$ of air at a 5000 Pa static pressure rise through the rest of the test apparatus. For the control needed to make the small adjustments that allow targeted exit chord Reynolds numbers to be achieved, a Hitachi variable frequency drive (VFD) is used to control the 45 kW electric induction motor. A simplified schematic of the blower attached to a test section can be seen in Figure 2.

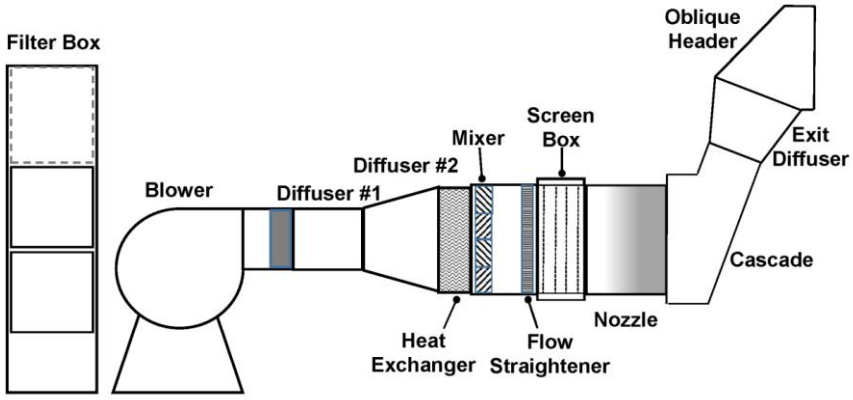


Figure 1. Large scale low velocity cascade wind tunnel [3].

Figure 2. New York Blower used for wind tunnel [39].

To recover static pressure downstream of the blower, a two stage multi-vane diffuser has been installed. The diffuser works by expanding and slowing down the airflow. At higher exit chord Reynolds numbers, the blower adds a significant amount of energy to the flow, which consequentially raises the temperature of the fluid. To remove some of this energy and regulate the temperature to within an acceptable range, the air is channeled through a 91.44 cm x 121.92 cm (36 in x 48 in) heat exchanger. A 1/2 hp common pool pump is used to circulate water from a 100 gallon tank through the heat exchanger. Cold make-up water is supplied to the reservoir from one of the main supply pipes within the building and excess water expelled through an overflow tube directly to a floor drain. A schematic of the heat exchanger and related components can be viewed in Figure 3.

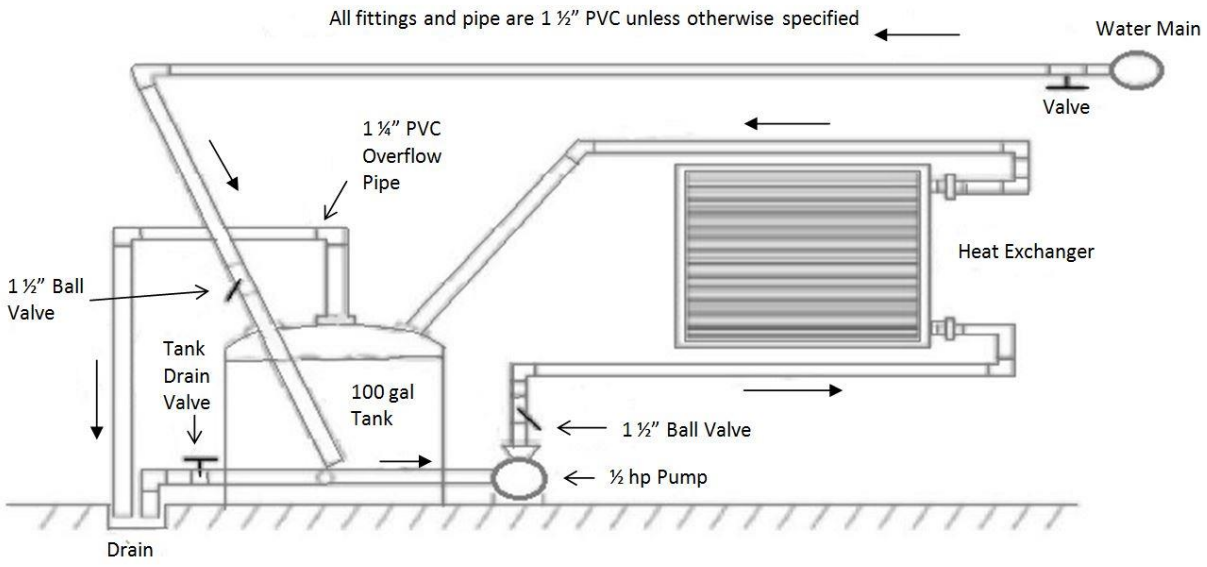


Figure 3. Schematic of wind tunnel heat exchanger [40].

Aft of the heat exchanger, a flow mixer was added to reduce spanwise temperature differences. Previous studies showed spanwise temperature stratification

when running at low turbulence levels and relatively high exit chord Reynolds numbers. At these high exit chord Reynolds numbers, more cool make-up water is needed to reach steady state wind tunnel temperatures. A spanwise temperature stratification was found to be present. Contrarily, this uneven temperature spread was not observed in high free-stream turbulence cases when elevated mixing takes place downstream of the heat exchanger. To cancel the uneven spanwise temperature effect at the lower turbulence cases, a flow mixer was added. The flow mixer is fixed approximately 33 cm (13 in) downstream from the heat exchanger where the full tunnel height begins. Ten rows of five fins were fabricated from 16 gauge steel. The rows alternate 60° to left and right from parallel to the approaching main stream flow. The mixer panel size is 91.44 cm x 127 cm (36 in x 50 in) and is shown in Figure 4 as mounted in the wind tunnel aft of the heat exchanger.

Figure 4. Flow mixer installed downstream of heat exchanger [39].

To realign and smooth the flow after the mixer, a flow straightener follow the flow mixer. Swirl is eliminated from the flow by passing through 2 inches (5.08i cm) of 1/8 in (0.3175 cm) diameter honeycomb aluminum. After the honeycomb aluminum, four nylon screens spaced 2 in (5.08cm) apart additionally condition the flow by reducing variations in velocity to improve uniformity. Seen in Figure 5 [39], the honeycomb aluminum and nylon screens provide for more uniform temperature and velocity throughout the flow.

Figure 5. Flow straightener (left) and sceenboxes (right) [39].

## Turbulence Generation

Three different turbulence generators (nozzles) were utilized to produce five distinct levels of turbulence ranging form ~0.7% to 17.4% during this study. By name,

the nozzles were known as the “low turbulence nozzle” (LT), “high turbulence nozzle” (HT) and “aerocombustor” (AC). To augment turbulence and create even more turbulence variations, a spool with two different sized grids were placed between the low turbulence nozzle and the test section.

The lowest turbulence level (0.7%) used during this study was generated by means of the low turbulence nozzle. Seen in Figure 6, the low turbulence nozzle has smooth inside surfaces and a 3.6 to 1 flow area reduction. In the low turbulence configuration, the small end of the nozzle is clamped directly to the cascade while the large end is bolted to the end of the screen box.

Figure 6. Low turbulence nozzle [41]

A spool with grid was installed in conjunction with the low turbulence nozzle to generate the second and third lowest turbulence levels used in this study. The small grid (SG) or a large grid (LG) are installed inside the decay spool between the nozzle and the

test section. The 25.4 cm x 127 cm rectangular constant cross section spool is constructed of 1.91cm (3/4 in) acrylic. Perpendicular to the flow, the grids are bolted to the inside of the spool, at respective locations, through holes drilled along the sides. The small grid consists of 0.635 cm (1/4 in) square aluminum bars spaced vertically and horizontally at 3.175 cm (1-1/4 in) intervals while the large grid is similarly constructed with 1.27 cm (1/2 in ) square aluminum bars with 6.35cm (2-1/2 in) spacing as depicted in Figure 7. When installed, the small and large grid are placed 32 mesh lengths (101.6 cm) and 10 mesh lengths (63.5 cm) , respectively, upstream of the beginning of the cascade. The small grid turbulence condition (SG), which has been referred to as the "small grid far" (SGF) in previous research [40, 39, 3], produces a turbulence intensity of 3.5% while the large grid yields a turbulence level of 8.1%. When referring to turbulence intensities, SG and SGF will be used interchangeably in this document.

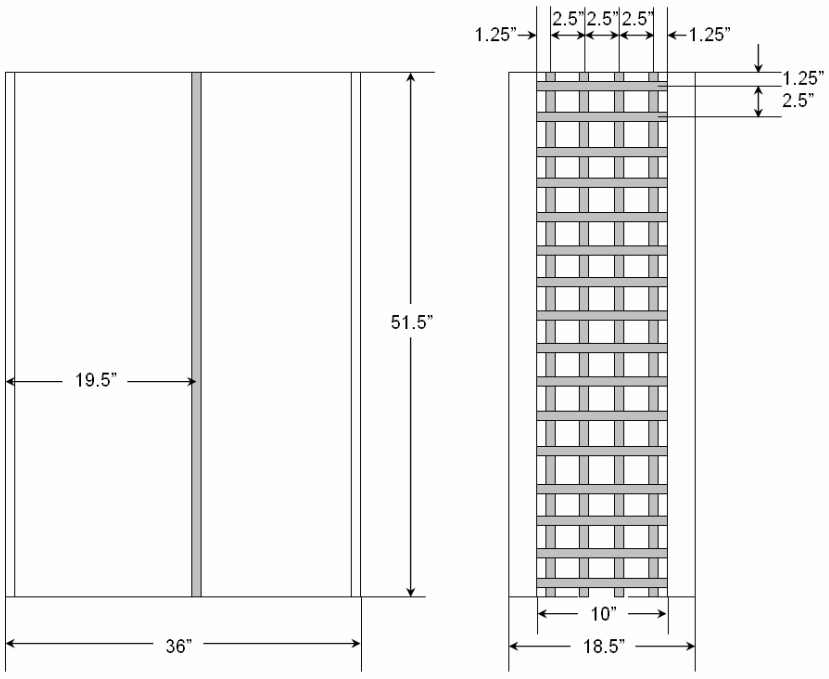


Figure 7. Large grid schematic with dimensions in inches [42].

The second highest turbulence intensity is created using the mock "aerocombustor". The nozzle has a 3.6:1 area reduction from inlet to end. A schematic of the aerocombustor can be viewed Figure 8. Flow passed through two sets of slots in the back panel before being pushed through a series of holes in the side panel. The air jets created from these apertures emulate recirculation and dilution zones that would be present in a modern gas turbine combustor. As with the low turbulence nozzle, the aerocombustor is placed in-between the screen box and cascade when installed. Turbulence intensities as high as 13.7% are achieved with the aerocombustor is in place. A picture of the mock aerocombustor can be seen in Figure 9.

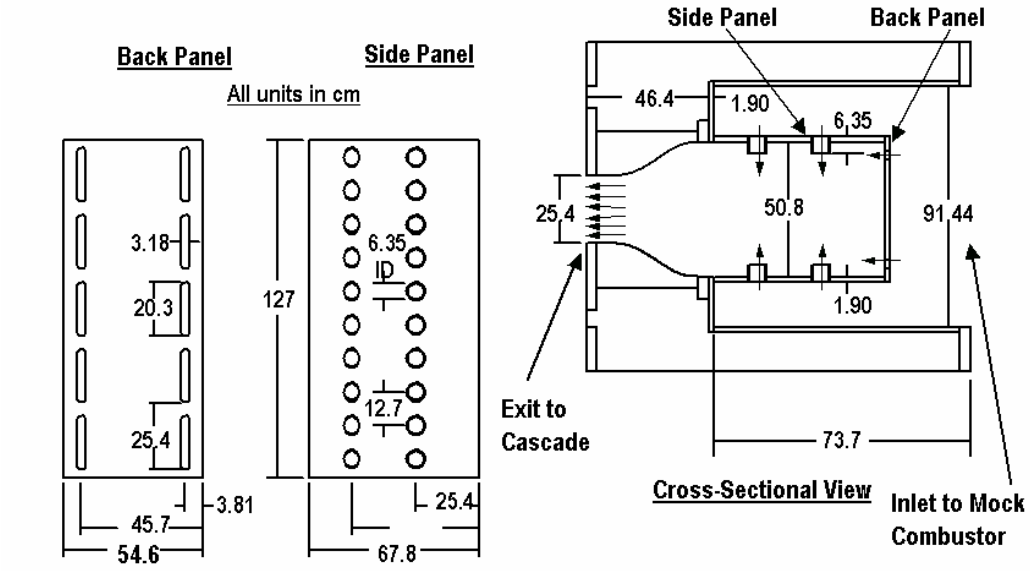


Figure 8. Aerocombustor schematic with dimensions in inches [43].

Figure 9. Image of Aerocombustor [41].

A high turbulence aerocombustor (HT) was constructed to produce an even higher level of turbulence. The elements within the high turbulence nozzle mimic those of the aerocombustor with slightly altered geometry designed to produce more turbulence. The exit area is the same as with the other nozzles used in this study. The HT nozzle is installed in the same manner as the AC nozzle and generates turbulence as high as 17.4%. Images of the high turbulence generator can be viewed in Figure 10.

Figure 10. Images of high turbulence generator [3].

The turbulence intensity associated with each generator has been well documented in a previous work conducted by a series of graduate students: Indrajit Jaswal; Mitchell Busche; Joseph Kingerly; and Justin Varty. These scholars were all working with Dr. Forrest Ames at University of North Dakota. Table 2 summarizes the turbulence intensities at the cascade exit chord Reynods numbers used for the present study.

Table 2. Turbulence level characteristics [43, 40, 44, 41].

| Turbulence Condition | U (m/s) | $Re_C$ | Tu | Lx (cm) | Lu (cm) | ε ($m^2/s^3$) |
|---|---|---|---|---|---|---|
| High Turbulence (HT) | 4.89 | 0.5mil | 0.1744 | 3.76 | 6.66 | 13.95 |
| | 9.72 | 1.0mil | 0.1744 | 3.91 | 7.22 | 101.3 |
| | 19.34 | 2.0mil | 0.1718 | 4.00 | 7.69 | 715.9 |
| Aerocombustor (AC) | 4.84 | 0.5mil | 0.1235 | 3.68 | 7.24 | 4.41 |
| | 9.11 | 1.0mil | 0.1302 | 3.52 | 6.36 | 39.4 |
| | 18.11 | 2.0mil | 0.1259 | 3.58 | 7.35 | 241.8 |
| Large Grid (LG) | 4.93 | 0.5mil | 0.0792 | 2.00 | 3.25 | 2.75 |
| | 9.94 | 1.0mil | 0.0798 | 2.04 | 3.34 | 22.41 |
| | 18.95 | 2.0mil | 0.0811 | 2.35 | 3.36 | 162.15 |
| Small Grid Far (SGF) | 4.70 | 0.5mil | 0.0384 | 2.38 | 3.81 | 0.232 |
| | 9.08 | 1.0mil | 0.035 | 1.73 | 3.23 | 1.49 |
| | 17.61 | 2.0mil | 0.0348 | 2.13 | 2.85 | 12.1 |
| Low Turbulence (LT) | 4.96 | 0.5mil | 0.0069 | 8.12 | 127.0 | 0.00005 |
| | 9.65 | 1.0mil | 0.0076 | 5.02 | 154.5 | 0.00038 |
| | 18.71 | 2.0mil | 0.0060 | 3.58 | 15.5 | 0.0139 |

## Linear Cascade Test Section

The linear cascade test section connects to the aft end of the nozzle configuration selected for a given test. The cascade in the present study was designed and constructed

by Justin Varty. He based his vane design on a modern mid-sized industrial gas turbine but created on an 11:1 scale [41]. The intent of the cascade is to produce a periodic flow around the vane-airfoil simulating the conditions commonplace in industrial gas turbine applications. The current configuration has four scaled large leading edge aft loaded vanes with three full passages in between vanes. These vanes are constructed having foam cores with cast epoxy outer surfaces and are bolted to the cascade. The test vane is instrumented to collect desired data while the remaining three vanes are not instrumented and are intended to provide the proper flow conditions that would exist due to adjacent vanes in a gas turbine. The instrumented vane, or "test vane", is interchangeable. For the current study, the pressure side vane and suction side vane are the test vanes. Two endwall heater foils and three endwall coolers are added to modulate endwall temperatures, which was not needed during the current research. Other features include a row of inlet pressure taps and a row of exit pressure taps, two adjustable tailboards, and an upper and lower bleed flow adjustment. The features and layout of the cascade can be seen in Figure 11.

The walls of the test cascade were fabricated from 2.54 cm (1 in) thick acrylic sheet that allows the researchers to view the test vane, and associated instrumentation, while in operation. The acrylic is rigid and provides solid platform while providing negligible media for heat transfer to the environment outside of the test section. Appendix A displays the dimensions of the cascade. There are rows of 30 inlet and exit static pressure ports that were used to characterize pressure distributions during previous investigations by Justin Varty [41] involving the same vane geometry. The inlet and exit pressure ports are placed at one-quarter axial chord upstream and downstream from the

leading and trailing edge of the of the vanes, respectively. Additionally, 10 probe access ports were drilled through the endwall to help monitor the inlet total pressure and temperature conditions of the cascade. Overall, the cascade turns the flow 74° to 75° prior to entering the exit diffuser. The cascade is depicted in Figure 11.

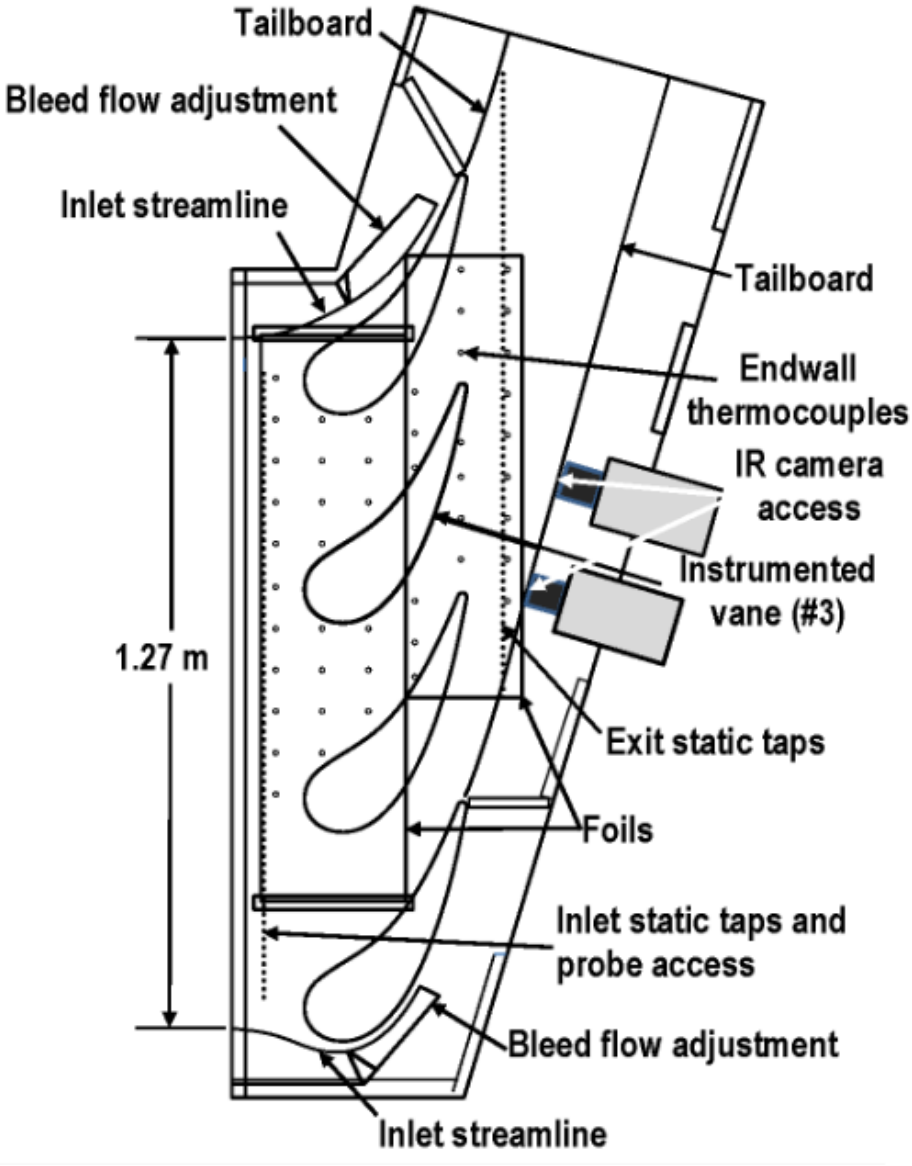


Figure 11. Layout of cascade test section [41].

On the top and bottom of the cascade are two are bleed flow adjustments to set boundary conditions that would exist if there were blades above and below the upper and lower vanes. The bleed flow adjustments were designed to remain flexible. For each these components, 10 individual pieces isocyanurate foam were routered to size using a mold created earlier in the process. The foam pieces were glued to a 1/64 in flexible epoxy fiberglass (G-10) board. Flow rates on the top and bottom of the cascade are controlled by manipulating the bleed flow adjustments that also helps maintain desired flow paths along the bottom and top vanes [41].

In order to manipulate the bottom bleed flow, a slot was cut near the bottom of the primary curve and rods were attached to the back of the fixture. Using plumbing fittings, the rod can be locked in place after being adjusted to meter flow. For the top bleed flow adjustment, a piece of adjustable acrylic is able to slide in or out to meter flow. The bleed flow adjustments can be viewed in Figure 12 [41].

Figure 12. Picture of bottom (left) and top (right) bleed flow adjustments [41].

Tailboards are attached to the trailing edges of the upper and lower vanes to ensure that there is exit periodicity in the flow. These tailboards are flexible and fine-tuned to follow the streamlines of the flow while taking into account boundary layer growth. The tailboards are 3/16 inch polycarbonate imbedded into a 1/4 inch machined slot located on the trailing edge of both the to the top and bottom vane. 3/8 inch nylon rods and compression plumbing fixtures are used to adjust the tailboards and lock them in place.

The tailboard facing the suction side test vane surface has two access ports for IR cameras to be placed to record surface temperatures during data runs. The two ports are sized such that a zinc selenide IR camera lens can be quickly switched out with a Plexiglas® cover. The upper and lower IR access ports allow the cameras to capture a temperature profile for the last 15 inches of the suction side of the vane. Two data runs are required under the same conditions to create a complete image. The camera is moved from one position to the next in between the runs and data is merged to form one surface plot for a given condition. The two windows cut directly into the tailboard and can be viewed in Figure 13.

Figure 13. Upper and lower IR camera port on bottom tailboard [41].

The IR camera can be mounted directly to the cascade at two separate positions that correspond to each access port. In each position, bolts protrude from the cascade such that the camera bracket it fastened with washers and nuts. Once mounted the IR camera bracket may be adjusted three dimensionally to set desired distance from the vane surface optimal camera angle. The picture of the IR camera mounted to the cascade can be seen in Figure 14. The camera will be discussed further in a later section of this document.

## Turbine Vane Geometry

The shape for all test vanes used in the research were identical with coolant slots being added test slot film cooling. The vane was designed by Ames and Varty [3] with a 13.208 cm (5.2 in) diameter leading edge and a 49.76 cm (19.590 in) chord length, which is a relatively high ratio for common airfoils. This design was selected to help reduce the heat transfer levels in the leading edge and also to allow space for internal cooling schemes. The suction surface of the blade is aft loaded, a shape that accelerates the boundary layer delaying transition from laminar to turbulent flow. The idea is to keep flow laminar as long as possible so the slot film cooling air is not mixed away by turbulent flow.

When mounted into the cascade, each vane sits at a 54.42° angle from horizontal and is vertically spaced 38.486 cm (15.152 in) from adjacent vanes. From leading to trailing edge, the axial chord distance, is 28.443cm (11.198 in). From endwall to endwall, the vanes have a span of 25.4 cm (10 in) exposed within the cascade. Three vanes are installed inside the cascade with through bolts and are not meant to be

interchangeable. The test vane position is the third from the bottom. The test vanes were outfitted with flanges so they could be easily installed by inserting them through a window cut into the endwall and bolting them down. There are currently four test vanes: pressure vane, heat transfer vane, pressure side film cooling vane and suction side film cooling vane. The two foremost vanes were used by Varty [41] to characterize pressure and heat transfer characteristics. The thermal efficiency for the latter two vanes was evaluated during this study at the same flow conditions used by Varty. Appendix A gives the general dimension of the vane geometry used.

## Internal Vane Plenums

Four plenums were designed to reproduce the fluid dynamics of the incremental impingement and counter cooling [21, 22] internal cooling schemes prior to the slot discharge. Due to geometry constraints, not all four plenums were able to fit into a single model vane. Three plenums were produced for the suction side vane and one for the pressure side vane. For simplicity, the pressure side coolant slot is referred to as PS1 while the first (or upstream), second (or middle), and third (or downstream) suction side coolant slots abbreviated to SS1, SS2, and SS3, respectively. When a respective test vane was installed, each vane plenum was connected to the outlet of an orifice tube using flexible tubing. Prior to the orifice tubes, flow is fed through an air conditioning unit and metered with gate valves. All components downstream from the evaporator are insulated.

Figure 14. Solid model of pressure side vane model [45].

The internal cooling scheme emulated with the plenums is a double wall high solidity pedestal arrangement. To mimic coolant passages, each plenum has three rows of 1.59 cm (5/8 in) diameter pedestals. Sheltered impingement jets set in a backside cutback of the last row of pins of the PS1 and SS1 plenums. The pin height to diameter ratio (H/D) is nominally 0.5 while the spacing spanwise to diameter ratio (Z/D) is 1.625. The streamwise spacing to diameter ratio (X/D) is 1.074. A solid model cutaway of the pressure side vane plenum is presented in Figure 14. For the pressure side plenum and the suction side plenum nearest the stagnation point, the exit is angled at 30° from the surface. The coolant air undergoes a 120° turn before exiting the second and third plenums on the suction side. The plenums slots have a nominal height (S) of 0.254 cm (0.1 in) and width of 23.5 cm (9.25 in). The transitions from the 0.8 cm high plenums to the slot begins 1.2 diameters downstream from the back of the last row of pedestals. The internal geometry is expected to produce flow that genuinely represents inflow turbulence

and vorticity that would be seen in an actual high solidity pedestal arrangement. This similarity is crucial in replicating the slot flow and unique mixing between the film cooling flow and freestream that would be found in this type of cooling scheme. A picture of the three suction side plenums can be viewed in Figure 15.

Figure 15. Picture of suction side vane plenums.

Each plenum had fine wire thermocouples slightly inside the cooling slots to monitor coolant discharge temperatures, For the pressure side vane plenum, five thermocouples were placed 0.7 cm (.27 in) upstream from the intersection of the downstream slot with the surface. Similarly, each suction side plenum had three thermocouples placed .38 cm (.15 in) to monitor coolant temperature at discharge.

## Pressure Side Vane

Polyisocyanurate foam was routered to the vane shape to fabricate the pressure side film cooling vane, and outfitted with the 3D printed plenum with pipe coupling as seen in Figure 16. The plenum acts to channel coolant through a .254 cm (0.1in) slot to the surface of the turbine blade. Prior to casting, the plenum was filled with wax to inhibit infiltration of the low viscosity epoxy. After 44 fine wire thermocouple were meticulously placed on the surface and inside the plenum, the vane was cast inside a

precision mold having a 0.16 cm gap filled with epoxy between the foam-plenum core and the mold walls. Once the epoxy cured, the vane was placed in an oven set just high enough to melt and drain the wax from inside the plenum. Any surface voids were filled with epoxy and the entire surface was sanded smooth.

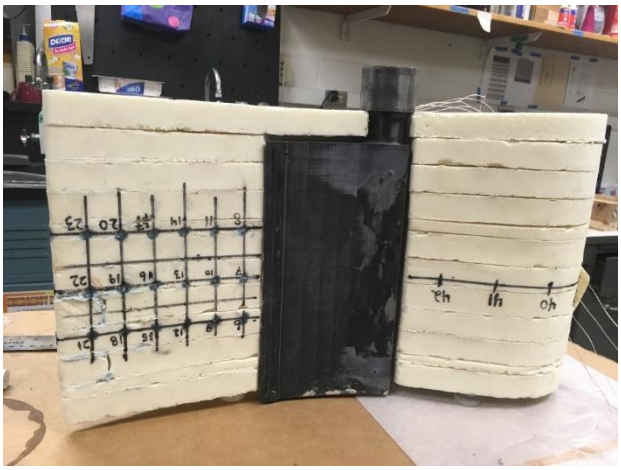

Figure 16. Pressure side vane routered from foam and fitted with 3-D Printed plenum.

To monitor vane surface temperatures, eight streamwise rows of three fine wire thermocouples were imbedded in the surface of the vane. The first row was placed 2.5 slot heights (X/S) downstream from the rear edge of the coolant slot followed by the second row another 6.3 X/S downstream. The successive rows were set apart at 10 slot heights until the last row was positioned on the rounded trailing edge about 12.3 X/S from the seventh row. Spanwise the placement of the thermocouple in each row was directly downstream of the pedestals, bisecting the space between pedestals and in between these positions. Figure 17 is a schematic of the vane from plenum insert to trailing edge and displays the thermocouple layout along with pedestal-jet positioning.

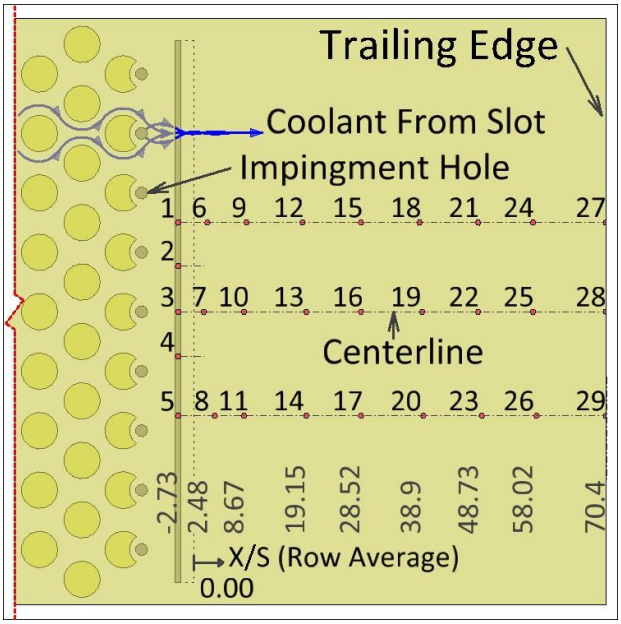


Figure 17. Pressure side vane thermocouple instrumentation.

## Suction Side Vane

The suction side film cooling vane was fabricated in a similar fashion to the pressure side vane. Polyisocyanurate foam was routered to shape and equipped with three 3D printed plenums as seen in Figure 18. Each plenum acts to deliver coolant through .254 cm (0.1in) slots to the surface of the turbine. The plenums were filled with wax prior to casting to avoid seepage of low viscosity epoxy into cavities intended to remain open for coolant airflow. A total of 89 fine wire thermocouples were set on the vane surface and inside the plenums before the vane was cast in a precision mold. A 0.16 cm gap was left between the foam-plenum core and the mold walls to create and epoxy skin. Once the epoxy had cured, the vane was placed in an oven and the temperature was

set to melt the wax out of the plenums without damaging the vane. The surface of the vane was manicured by filling voids with epoxy and sanding rough surfaces.

Figure 18. Suction side vane routered foam fitted with 3-D Printed plenums.

From the exit of the first coolant slot to the trailing edge, 26 rows of three fine wire thermocouples were imbedded in the coolant slots or in the surface of the vane. The streamwise row spacing from discharge at the rear of the slot edge to vane trailing edge ranged from 1 to 201.13, 1 to 188.5 and 1.1 to 117.9 for the first, second and third film coolant slot respectively. Figure 88 in Appendix B displays a diagram of the streamwise spacing with respect to each slot. The spanwise the placement of the thermocouple in each row was the same as the pressure side spacing. Figure 19 is a schematic of the vane from third plenum slot to trailing edge and displays the thermocouple layout along with pedestal-jet positioning.

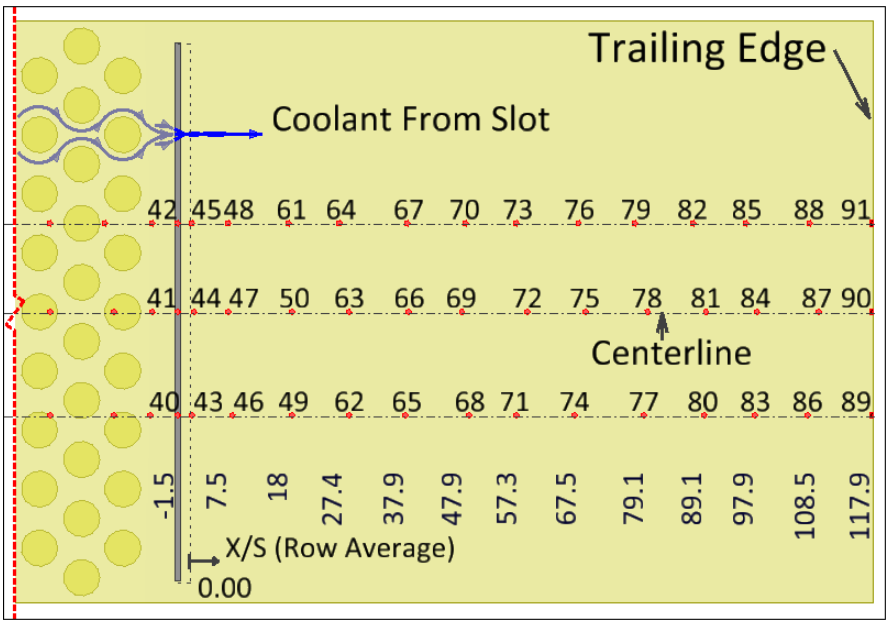


Figure 19. Suction side vane thermocouple instrumentation from third slot.

## Infrared Camera Measurements

Infrared (IR) camera thermography data was recorded to better visualize the film cooling effectiveness on the suction side vane. A FLIR SC500 camera was used to capture 320 x 240 pixel images. The system is capable of generating live temperature distributions of the vane surface when used in conjunction with the FLIR Systems ThermaCam Researcher. As discussed in a previous section, the SC500 was mounted to the rear of the test section, placed at an angle that gives the best view of the vane directly downstream of the third suction side film cooling slot. To have a clear view while maintaining the cascade flow boundaries, a zinc selenide coated glass window is placed in the camera access ports. Having low absorptivity and ability the transmit infrared images, Zinc selenide (ZeSe) is ideal for use with an IR camera for this application. The ZnSe lens measures 7.62 cm (3 in) in diameter fits snuggly into either access port cut into

the bottom tailboard directly to the top of the test section. Figure 20 shows the adjustable the IR camera and ZeSe lens mounted in the lower access port of the bottom tailboard.

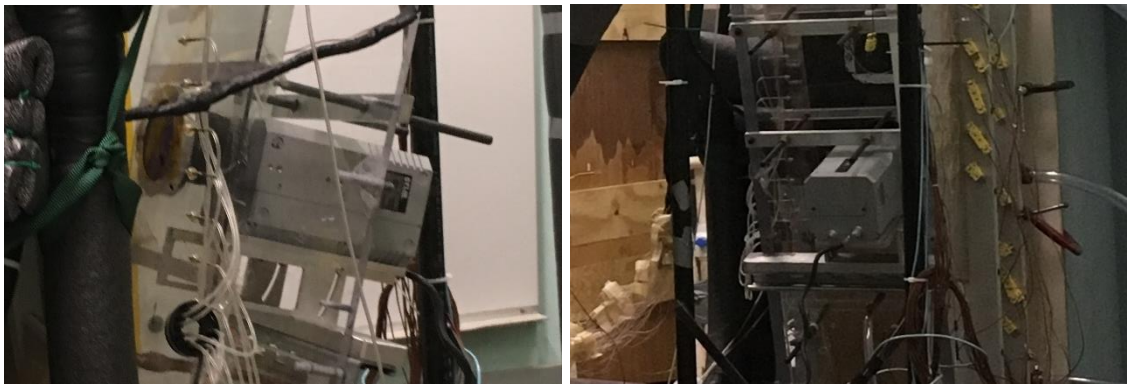

Figure 20. Mounted IR camera and zinc selenide lens.

The test surface was painted matte black and gold flake reference dots were added to calibrate the IR images with thermocouple measurements. The gold dots appear as bright spots in the captured IR image, allowing known positions to be identified. Black acrylic paint with a known emissivity of .96 was applied with a small airbrush to give a smooth finish. After the black paint dried, a paper template with apertures spacer in a 5.08 cm (2in) square pattern was taped to the surface of the vane. The apertures were then dabbed with a gold flake pen creating small circles of 0.437 emissivity paint the desired location. The process of painting the gold dots can be seen on the left of Figure 21.

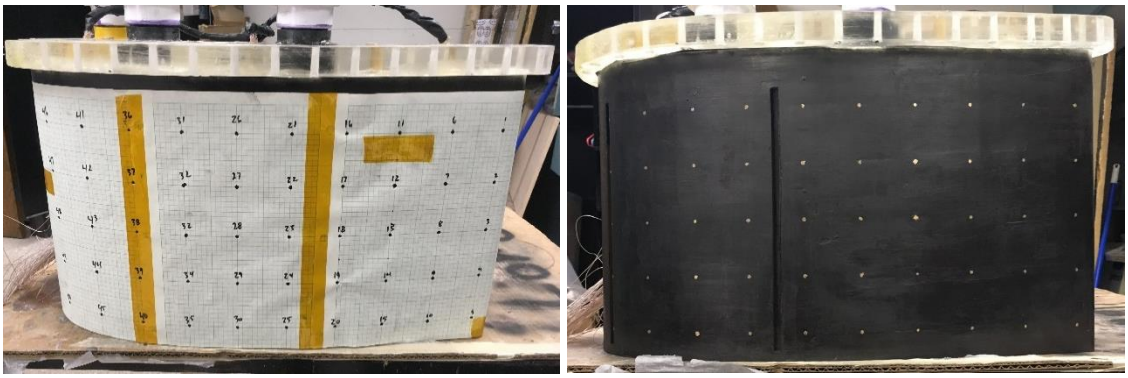

Figure 21. Test vane with paper template (left) and completed test surface (right).

## Coolant Supply System

Cool air for the film cooling slots is pushed through the system using a New York 1704A Blower. The blower speed is controlled with an AC Tech variable frequency drive. Similar to the larger wind tunnel, the film coolant air becomes challenging to manage without a heat exchanger. For instance, on a hot day the lab environment can reach temperature of nearly 90°F, which does not allow for a large difference in temperature between the coolant and cascade free-stream temperatures. The smaller temperature differential produces larger error and poor film cooling measurements. To remove heat, a heat exchanger is installed immediately downstream of the blower before the air conditioning unit as seen in Figure 22. The heat exchanger consists of a motorcycle engine oil cooler, 5 gallon water reservoir and a 1/4 hp submersible water pump. Cold make-up water taken from a building water main can be introduced to the reservoir through an inlet at the bottom while the warmer water is pushed out through an overflow line at the top of the reservoir. At 25 GPM, the submersible pump circulates water through the 22.23 cm x 18.42 cm (8.75 in x 7.25 in) heat exchanger. A picture of

the small blower, heat exchanger (black box) and the reservoir (white 5 gallon bucket) can be viewed on the left of Figure 22. The inside of the heat exchanger is seen with lid removed on the right side of Figure 22. The heat exchanger plenum was sealed with foam tape, wooden screws and silicone.

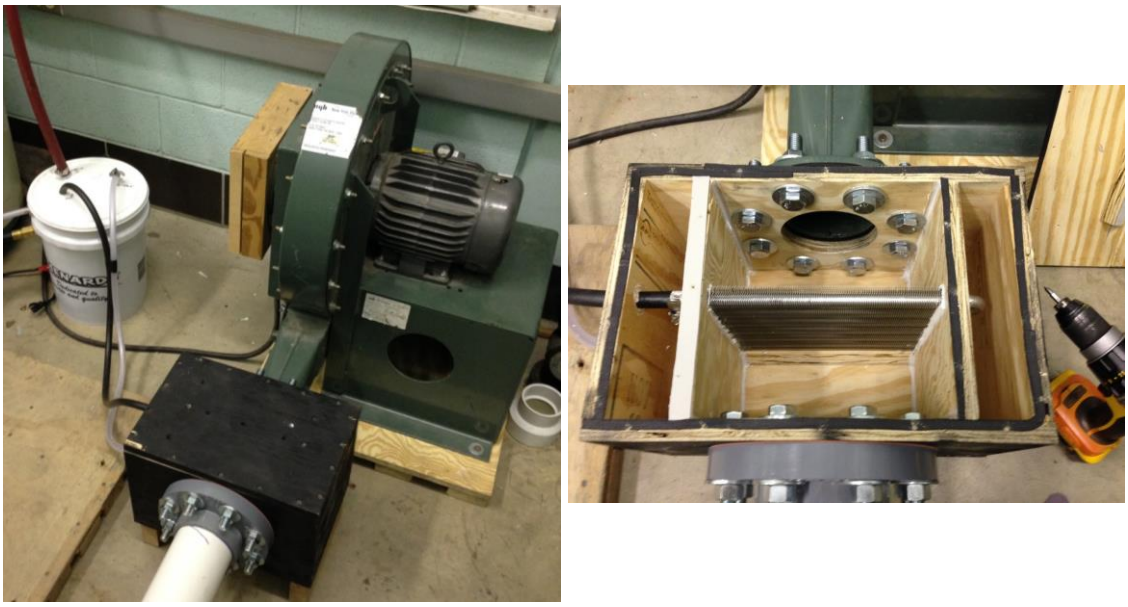

Figure 22. Small blower (Left) with heat exchanger system (Right).

**Air Conditioning Unit.** To cool the film cooling air, a large Haier America window air condition unit was modified and installed downstream from the heat exchanger. Rated at 24000 Btu/hr, the AC unit is advertised to cool a room as big as 1500 $ft^2$. Ductwork was fabricated from steel siding and sheet metal screws to direct flow from the heat exchanger directly into intake. After the air is conditioned the ductwork channels the air out of the evaporator to the orifice tube systems. The interior fan was removed, to prevent losses, as it was not cable of pushing at the same volumetric rate as the small blower. All metal ductwork was secured with sheet metal screws and sealed with silicon and aluminum tape. As much as possible, the outside of the ductwork along with the flexible tubing

from the heat exchanger was insulated with expanding window foam and preformed pipe foam. Pictures of the AC unit before and after modification can be seen in Figure 23.


Figure 23. Haier America 24000 Btu/hr AC unit before and after modification.

**Thermal Inertia Box.** To maintain consistent coolant temperatures, a thermal inertia box is implemented downstream of the AC unit. For a given setting, the AC's internal thermostat sends a signal to "kick-on" at a high limit and "cut-out" at a low limit temperature. To moderate these cyclical temperature fluctuations, the coolant air is routed through a sealed box containing thirteen 2.54 cm x 25.4 cm x 55.88 cm (1 in x 10 in x 22 in) aluminum plates. To create room for coolant to pass by each plate, small pieces of 0.3175 cm (1/8 in) particle board are placed in between each surface. Made of 1.27cm (1/2 in) thick plywood, the box is insulated with 2.54 cm (1in) polyisocyanurate foam insulation and sealed with silicone caulk. The aluminum plates were originally used as a mold for a previous turbine blade design. They have now been repurposed to function as heat sinks, or thermal masses, by cooling off air passing through when the AC unit has cycled off. When the AC unit is cycled on, the plates are cooled to the desired temperature. Thermocouples were added before and after the thermal inertia box to

monitor coolant temperature. It takes about 45 minutes for the plates to reach thermal equilibrium after the blower and AC unit is turned on. Viewing Figure 24, the thermal inertia box can be seen with the lid removed (left) and installed underneath the AC unit (right).

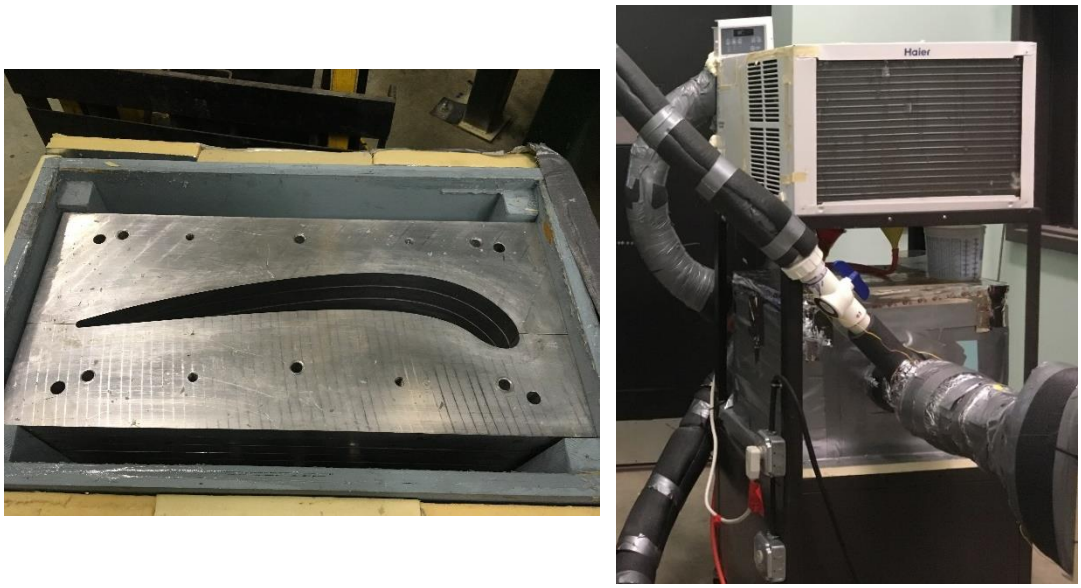


Figure 24. Thermal inertia box with lid removed (left) and installed in system (right).

Air exits the thermal inertia box into a 7.62 cm (3 in) PVC pipe that connects to the to the downstream orifice tube system. Midway down this pipe is a 5.08 cm (2in) branch pipe with ball valve used to bleed air. At lower blowing ratios, not as much coolant air is required. Without bleeding air, the blower runs well below its power range to push air at these lower flow rates. When the bleed valve is opened, the some of the air is released and the blower can run at higher speeds alleviating this problem. Additionally, at lower blower ratios, the aluminum plates are maintained at much lower temperatures. This effect allows for a larger difference between the coolant temperatures and wind tunnel temperatures which leads to smaller error in calculated thermal effectiveness.

**Orifice Plates.** Four orifice plates were sized to allow the desired range of blowing ratios for a given coolant slot. Each orifice plate disk is machined from 0.635 cm (0.25 in) thick aluminum and has a 15.24 cm (6 in) outside diameter. The orifice plates are referred to by the coolant slot they are assigned to. The inner diameters orifice for PS1, SS1, SS2, and SS3 are 3.226 cm (1.270 in), 3.556 cm (1.400 in), 2.550 cm (1.004 in), and 2.741 cm (1.079 in), respectively. The orifice itself forms a 90° sharp edge with the upstream surface, has a constant diameter for .102 cm (0.04 in) and tappers out at a 45° angle until it terminates at the downstream edge.


Figure 25. Thermal inertia box with lid removed (left) and installed in system (right).

**Orifice Tubes.** The orifice tubes are coupled with a flange to the PVC pipe that extends from the thermal inertia box. Shortly after the flange coupling, a 7.62 (3 in) PVC wye fitting creates three separate paths for flow. For each branch, the diameter is reduced from 7.62 cm to 5.08 cm (3 in to 2 in) and connected to a gate valve. Following the gate valves, sections of 5.08 cm (2 in) PVC pipe were installed such that at least 22 and 14.29 orifice diameters lengths (78.74 cm and 50.8 in) proceed and succeed the orifice plates, respectively. The intent of the extended pipe length is to promote smooth and fully developed flow. Inserted perpendicular to the flow fore and aft of each orifice plate are 0. 0.15875 cm (1/16 in) diameter brass tubing lengths that act as upstream and

downstream pressure taps. The brass tubing has brass pipe nipples soldered at the far end so rubber tubing can easily be attached. The orifice tube system was covered with preformed pipe insulation and mounted on a custom-built movable cart as seen in Figure 26.

Figure 26. Orifice Tubes mounted insulated and mounted on movable cart.

The mass flow rate through each tube is calculated from individual pressure differentials measured using an upstream and downstream pressure taps. The series of blowing ratios tested required the use of all four orifice plates in two different configurations. For testing the pressure side vane, flow through the top two orifice tubes is cut off by shutting gate valves # 2 and 3. The remaining gate valve is adjusted to produce the desired blowing ratio with the respective tube having the PS1 orifice plate installed. This configuration can be viewed on the left side of Figure 27. The suction surface vane requires the use of all three orifice tubes. Gate valves 1-3 are adjusted to meter flow through orifice plates SS1, SS2 and SS3 producing the desired blowing ratios

to respective slots on the vane surface. The suction side orifice configuration can be seen on the right side of Figure 26.

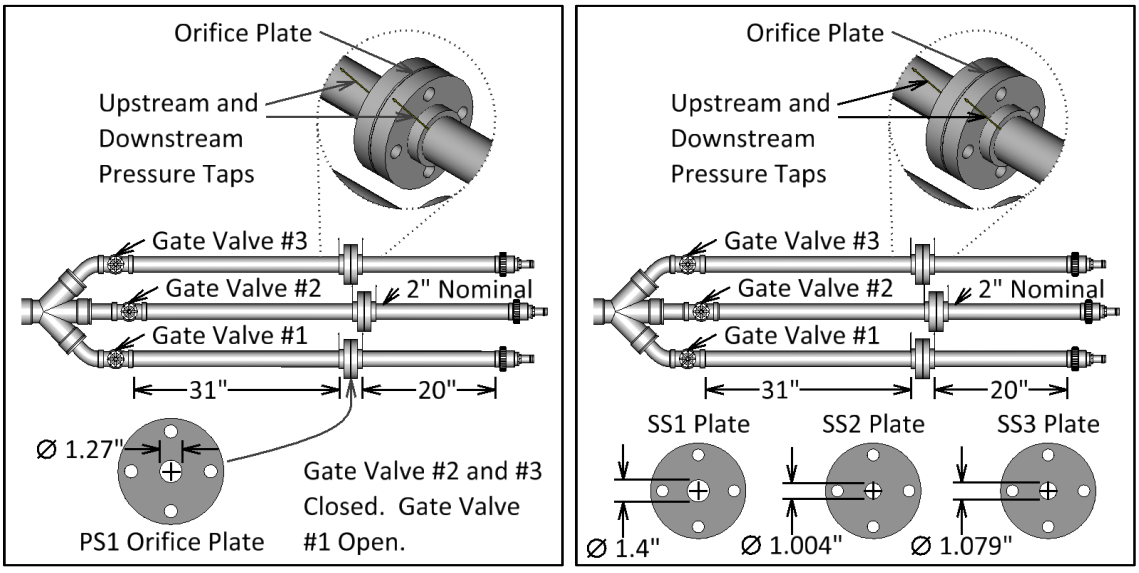


Figure 27. Orifice Tubes for Pressure Side (left) and Suction Side (right) configurations.

The system is contracted to be modular, and is able to be broken for removal. The tubes themselves rest on a three-wheeled wooden cart allowing the system to move to accommodate the size and shape of different turbulence generators. Flexible tubing was used to connect the coolant system to the various test section configurations. Figure 28 shows the small blower with the heat exchanger, the thermal inertia box, the bleed valve and the orifice plate.

Figure 28. Entire coolant supply system.

## Data Acquisition

Fort this study, a Hewlett Packard 3497A data acquisition system was used to acquire thermocouple data while thermal camera data was captured in using the FLIR Systems ThermaCam program for processing through Microsoft Excel and Matlab. The Hewlett Packard 3497A is capable of reading 100 channels with a sensitivity of one microvolt and was connected to a computer running Microsoft QuickBasic on DOS. The FLIR program delivered a 240 x 320 matrix of temperatures in a .cvs file.

**Temperature Measurement.** K-type fine wire thermocouples were used to acquire temperature inside the vane plenums, coolant system and on the vane surfaces. The thermocouple wire was ordered from Omega Inc. and is composed of chromel and alumel

strands that are individually insulated. Together the strands comprise 36 gauge wire nominally. Having a small footprint and being extremely malleable, the thin wire has been ideal for this application. After being cut to length, the last cm of wire was stripped of insulation at both ends. On the sensing end, the chromel and alumel strands were welded together to form a small ball-type junction with a Therm-X thermocouple welder. The other end was fitted with a male plug suitable for connecting to the board on the front of the data acquisition tower. The data acquisition tower can be seen in Figure 29.

Figure 29. Data acquisition tower [39].

The thermocouples were carefully placed on the vane test surfaces, in the cascade free stream, inside the coolant plenums, before and after the air conditioner, in the orifice tube system, and in the external environment. For a reference temperature, a thermocouple was maintained at 0° Celsius using a fresh ice-bath during testing. The ice bath consisted of a Cabella's brand thermos filled with ice water having a glass tube snuggly fit through the drinking orifice to separate the thermocouple from the ice water itself. One end of the glass tube was heated and closed in the chemistry department. Through the open end, a thermocouple was fished into the tube until the junction end of the wire hit the closed end. To provide a uniform temperature, mineral oil was added into the tube until it matched the level of the surrounding ice bath.

Figure 30. Suction side vane with instrumented with thermocouples.

**Pressure Measurement.** Two Rosemount pressure transducers were used to acquire pressure measurements during this study. The smaller and larger transducers are capable of measuring differential pressures up to 250 Pa and 5000 Pa, respectively. Rated to full scale, both transducers have a documented accuracy of ±0.1%. The transducers are connected to the computer via the pressure sensor scanner board that is also located on

the data acquisition tower. A system of tubing connects 48 12 volt pressure solenoids to the MC computing CIO-ERB48 electromagnetic relay board. Four of the solenoids were routed to the high side port on the transducers while the other 44 were connected to the low side.

**Procedure.** The procedure for collecting data for the suction and pressure side tests vanes is very similar. However, the suction side vane proved to be much more challenging due to two primary differences: Achieving and maintaining steady state conditions while testing the suction side vane proved to be more challenging due to managing blowing ratios for three plenums and repositioning of the thermal camera to capture images in the "top" and "bottom" position. The rest of the steps were essentially the same for each test configuration and will be explained in the following section.

To prepare equipment for testing a sequence was followed. The first preliminary step, was to turn on the AC unit and small blower at least 5 hours prior to acquiring film cooling data sets to cool down the plates in the thermal inertia box. The next step is highly important! Prior to starting up any additional component of the test facility, the ice bath was inspected to ensure ample ice was present. Skipping this step often lead to an incorrect reference temperature and nonsensical data, which is usually discovered after several iterations of testing. To limit frustration and lost work, it is imperative to ensure the ice bath is fresh. The next step is to record the barometric from the lab manometer. This step, along with room temperature and general room conditions, is recorded in the research logbook for future reference. The ball valves controlling the water supply to the heat exchanger reservoir and small blower heat exchanger are then actuated to the flow position to ensure the pumps have adequate net positive suction head prior to being

turned on. Finally, the master breaker for the large blower was energized and the VFD adjusted to a position known to produce desired exit chord Reynolds numbers.

It is then time to start up the lab equipment, which includes the water pumps for heat exchangers, AC unit, blowers, data acquisition system and computer with correct Quickbasic (QB) program opened. The QB program prompts the user to enter the barometric pressure and dimensionless pressure at the relevant slot locations. The dimensionless pressures were calculated from data, obtained by Justin Varty, characterizing the pressure profile of the same vane geometry under the same test conditions [41]. Once these key parameters were entered, the program displayed a menu. The option to re-zero the pressure sensors was always selected to ensure the transducers were freshly zeroed prior to testing. After each routine, the program returns to the main menu. Once the re-zeroing sequence was complete, the monitoring routine was chosen and the VFD for the large blower was adjusted until the exit chord Reynolds number read the desired value. Meticulously, the coolant system valves and VFD for the small blower were manipulated until the targeted exit chord Reynolds number and blowing ratios for each coolant slot were displayed. Small adjustments were made until system was observed to be at steady state for reasonable increment of time.

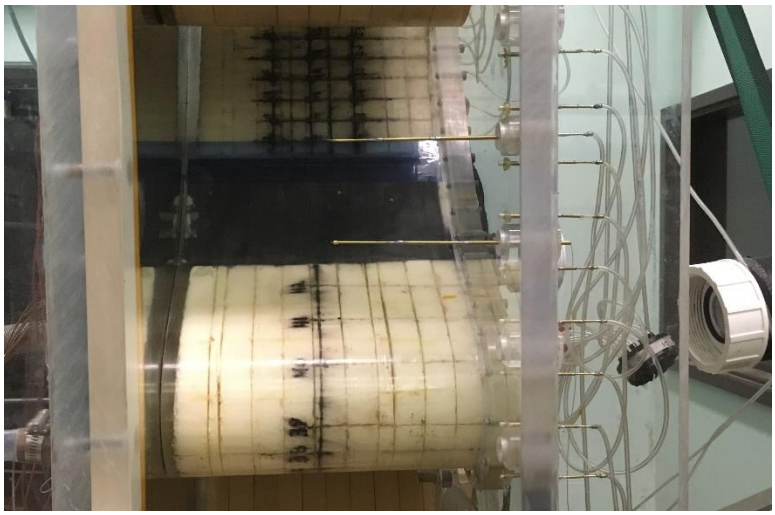

Figure 31. Pressure side vane with SS1 coolant slot taped over.

For each individual film cooling configuration, two types of data were taken; with and without (adiabatic) film cooling. The adiabatic data runs were performed with all valves closed on the coolant system and the slots taped over as seen in Figure 31. Steady state was considered to have been reached when coolant plenum discharge temperatures ($T_{SS1}$, $T_{SS2}$ and $T_{SS3}$) and Total Cascade Inlet Temperature ($T_{total}$) changed less than 0.05 °C in a ten minute time period. Three data sets were acquired with no coolant flow through the plenums and then with coolant flow according to prescribed scheme. When lower blowing ratios were applied, the goal for data sets was to have a minimum of 5 °C $\Delta$T between the plenum inlet temperatures and the first row of surface thermocouples that followed each coolant slot. At higher blowing ratios, a higher goal of approximately a $\Delta$T of 10 °C was assigned. Figure 32 displays the suction side test vane configured to provide film cooling through three coolant slots.

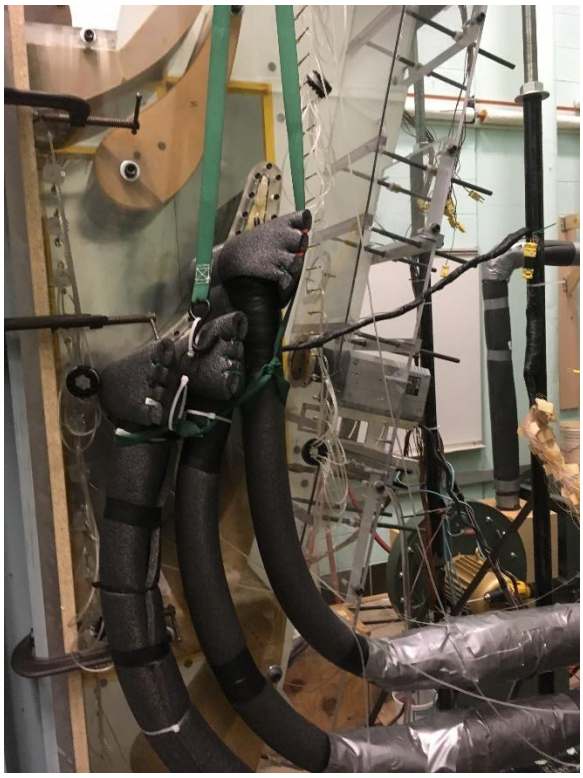

Figure 32. Suction side vane with three supplied coolant plenums.

At the end of the the data collection sequence, the QB program prompted the user to enter an eight digit file name. QB is limited to eight digit file names as it is a 16 bit programing language. The files store as .PRN files which are able to be opened by Microsoft Excel and re-saved as .xlsx files. The user is able to change the last character of the extension when saving, which is how each data runs was tracked. Table 3 displays the file labeling nomeclature used in this study. For example, when the third data run for the suction side vane, in the second blowing ratio configuration, with a cascade Re of 500,000, and having the high turbulence generator installed, the data was recorded as BRS2r5HT.pr3. Blowing ratio configurations are annotated in the test matrices for the pressure and suction side vanes can be viewed in Table 6 and Table 7 of Appendix C, respectively.

Table 3. Quick Basic data file labeling nomenclature.

| Character Positions | Character Meanings |
|---|---|
| 1 and 2 | BR - Blowing ratio vane heat transfer |
| 3 | S - suction surface vane or P - pressure surface vane |
| 4 | 0 - Adiabatic no Blowing Ratio. 1,2,3…z - Blowing ratio configuration number (see matrix) |
| 5 and 6 | r5 - $Re_C$ = .5mil, r1 - $Re_C$ = 1mil, r2 - $Re_C$ = 2mil |
| 7 and 8 | HT - high turbulence, LT - low turbulence, LG- large grid, SM - small grid, AC - aerocombustor |
| Extension | Enter run number in extension - .prn (ie pr1,pr2.....prn) |

For the suction side testing IR camera data was acquired simultaneously as all other data acquisition procedures remained the same. Due to tube-pressure settling times and a high number of thermocouples, the acquisition sequence takes about four minutes to complete. This provided ample time for both a physical image in the ThermaCam Researcher program and a temperature array (.csv) file to be recorded for each data set taken on the suction side test vane. To cover a larger surface area of the vane, arrays and images were recorded from the top and bottom camera port. The images were later processed into one image. For each blowing ratio configuration, three images and temperature arrays were recorded in the top and bottom positions. The file naming nomenclature mirrored the method used for storing QB .prn files with the exception of additional two digits prior to the .cvs extension. The two digits designated weather the top (t) or bottom (b) camera access port was used and during which data run (1,2,3….n) the arrays and images were recorded. For example, when the bottom port was used during the third data run for the suction side vane, in the second blowing ratio configuration, with a $Re_C$ of 500,000, and having the high turbulence generator installed,

the temperature was recorded as BRS2r5HTb3.cvs. A full test configuration wind tunnel test configuration is displayed in Figure 33.


Figure 33. Full tunnel setup in small grid far suction side test configuration.

# CHAPTER IV

# EXPERIMENTAL RESULTS

This chapter will discuss the results found in the study regarding film cooling effectiveness on the suction and pressure side vane. Discussions will include the effects of blowing ratio, turbulence and Reynolds number often plotted as film cooling effectiveness ($\eta$) as a function of slot distance normalized with respect to slot height (X/S). Film cooling effectiveness was calculated using Eq. 1, seen in appendix D. This chapter will also include a discussion on the findings of the IR camera measurements on the suction side surface to give insight to the spanwise coolant coverage past the third coolant slot.

## Pressure Surface Results

The vane geometry for pressure side testing was constructed with a cooling scheme intended to reduce temperatures on the leading edge and near suction surface while including a double wall for internal flow to cool almost 60% of the pressure surface [46]. The incremental impingement incorporated into the pressure surface serves as an effective means to cool the vane surface from within by using coolant air, intended to protect the trailing edge, prior to its discharge at downstream slots. This cooling methodology eliminates the need for showerhead cooling schemes greatly reducing the risk of deposition clogging. Additionally, the trailing edge region is shielded with

thermally protective cooling. The present vane geometry allows coolant to discharge from the pressure side slot (PS1) in a region of high acceleration (-0.3 m surface distance) as noted in Figure 34 and Figure 35. Within the plenum, coolant passes between three rows of high solidity pedestals followed by a row of impingement jets prior to discharge from the slot. This arrangement is meant to emulate incremental impingement [47, 48]. Data sets consist of three blowing ratios (0.4, 0.7, and 1.0), at five turbulence conditions ranging from $0.7\% \leq Tu \leq 17.4\%$, and over exit chord Reynolds numbers of approximately 500,000, 1,000,000, and 2,000,000. Slot Reynolds numbers (slot height as a characteristic dimension) ranged from 1260 to 5030 at a nominal blowing ratio of 1.00 for the three chord Reynolds numbers.

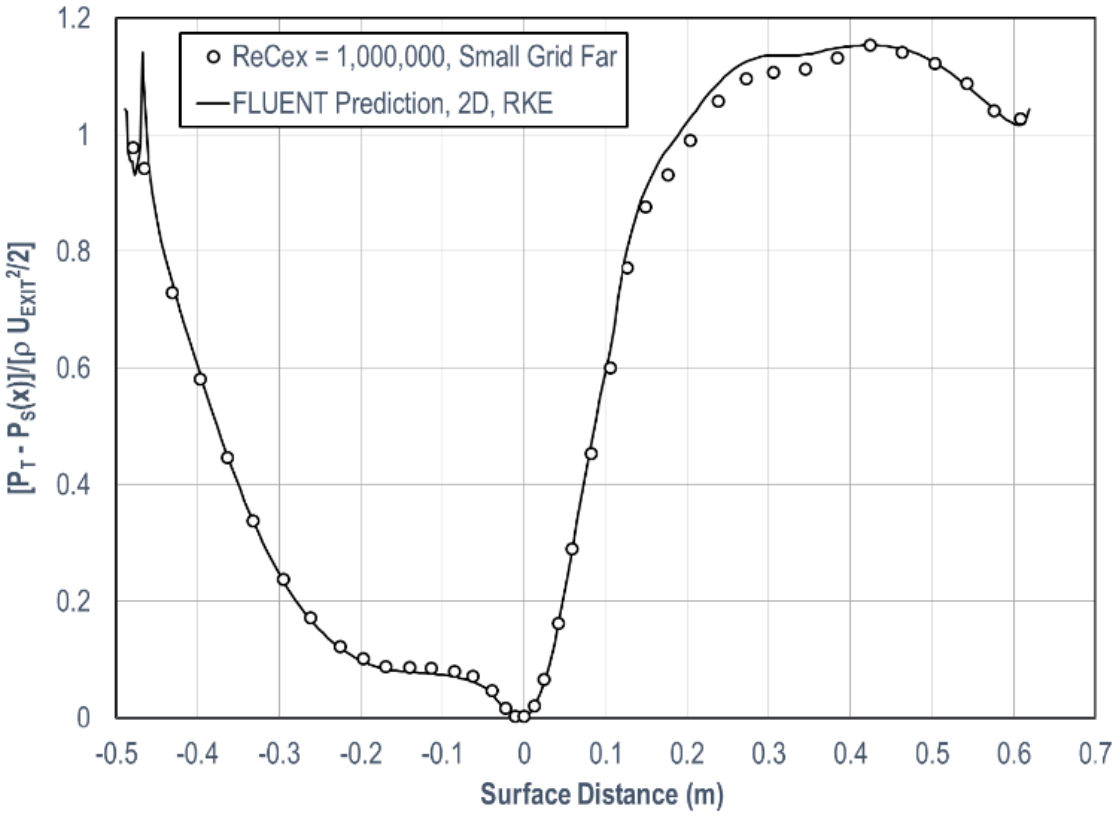


Figure 34. Vane surface $P_{stat}$ distribution normalized on exit $P_{dyn}$ [47, 48].

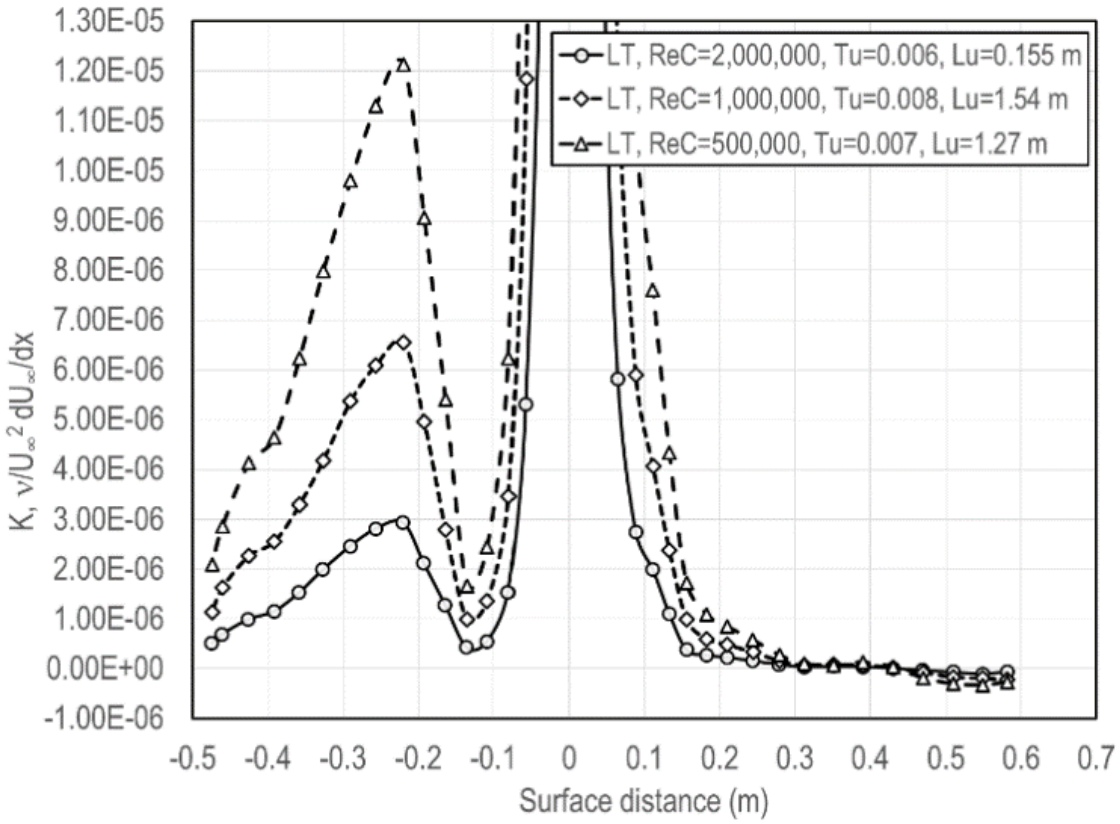


Figure 35. Acceleration v.s. surface distance for vane surfaces [47, 48].

Upstream of the coolant slot, the thickness of the boundary layer is presumed to be small as the behavior of the flow in that region is an accelerating laminar and transitional boundary layer. Exit condition Stanton number distributions for the base vane are plotted against exit chord Reynolds number set to 1,000,000 can be viewed in Figure 35. Starting from zero and moving left (negative distance) represents the pressure surface form the stagnation point to trailing edge for which the Stanton number initially decreases sharply and levels out. This is trend is characteristic of laminar heat transfer. In a previous study by Varty and Ames [49] there was distinct differences in heat transfer augmentation at the same five turbulence intensities investigated in this study. The same trends were observed for Stanton number distributions at an exit chord Reynolds number

of 500,000; however, over the pressure surface at an exit chord Reynolds number of 2,000,000, the distributions displayed indications of transitional behavior upstream of the slot.

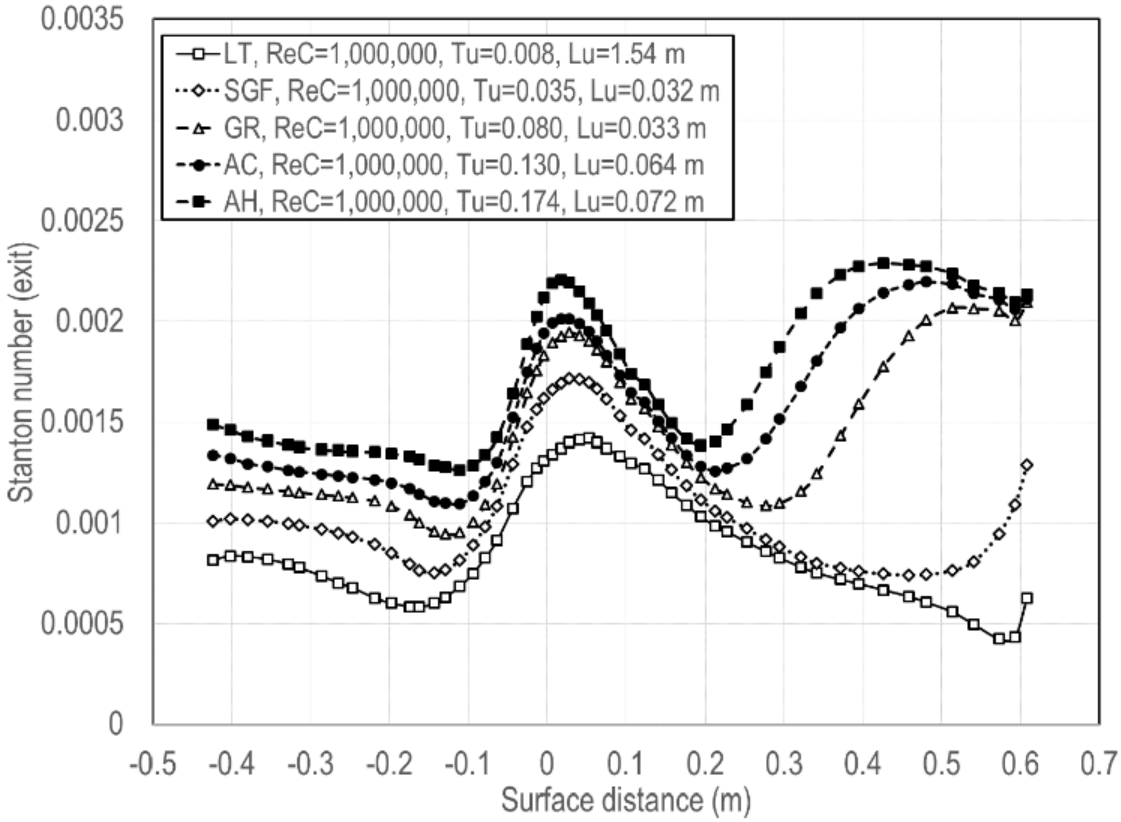


Figure 36. Surface Stanton number based on exit conditions w/no film cooling [49].

**Pressure Side Vane Spanwise Uniformity Measurements.** Flow traverses inside the PS1 plenum through three rows of high solidity pedestals prior to discharge. Impingement jets are incorporated into the aft end (with respect to flow) of the final row pedestals. Downstream surface temperature measurements were acquired at spanwise locations: the center impingement jet (center), the center breadth of the last row (right) and in between these two positions (left) as shown in 17 on page 34. These positions are

approximated based on different periodic flow locations. The average of the spanwise temperature readings at each streamwise location were plotted to create the streamwise film cooling distributions. These distributions are nearly uniform and thought to be more exact than the uncertainty estimate associated with the incremental placement of the thermocouples. A spanwise comparison of film cooling distributions can be seen in Figure 37, which displays the three spanwise positions with a nominal blowing ratio of 0.7 and the small grid far turbulence condition. Downstream effectiveness from the impingement jet (center) and the mid-breadth (right) was elevated compared to the between position (left). This variation in spanwise effectiveness reveals the tendency for vorticity from impingement jets and horseshoe vortices from the pins to cause some notable unevenness in the spanwise film cooling coverage at higher blowing ratios. The subsequent effectiveness distributions are calculated as an average of the three adjacent spanwise positions for each streamwise position, which is assumed to be and accurate representation of spanwise average effectiveness.

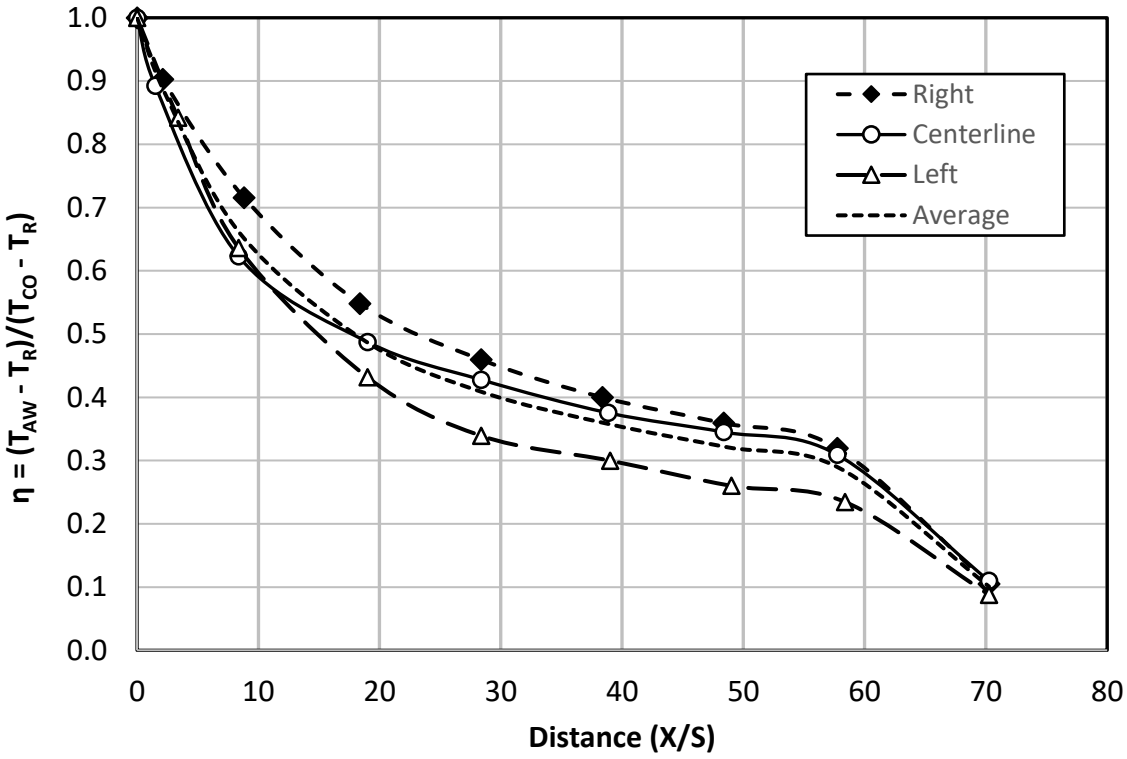


Figure 37. SGF pressure side streamwise distribution, $Re_C$ = 1,000,000, $M_{PS1}$ = 0.69.

**Effects of blowing ratio at increasing turbulence levels.** Figure 38 displays adiabatic film cooling effectiveness at blowing ratios of $M_{PS1}$ = 0.4, 0.7 and 1, at the lowest turbulence condition (Tu = 0.76%) with an exit chord Reynolds number of 1,000,000. Initially, the film cooling effectiveness decays rapidly which implies a great degree of interaction with the free stream. The highest effectiveness is displayed at the smallest blowing ratio (M = 0.40) close to the coolant slot (X/S of about 9), but decays more rapidly thereafter compared to effectiveness at higher blowing ratios. Moving away from the slot, at about X/S of 17, the lower blowing ratio crossed the two higher blowing ratios. Data recorded at all three blowing ratios shows precipitous decline until roughly X/S of 30, then levels off. This is especially notable for a blowing ratio of $M_{PS1}$ = 1.0. Subsequently, the degree of effectiveness for a blowing ratio of $M_{PS1}$ = 0.7 is remains

around 0.03 to 0.04 lower than that of a blowing ratio of $M_{PS1}$ = 1.0; however, the effectiveness of the lowest blowing ratio continues to decay at a greater rate. Approaching the trailing edge, the spline fit curves display a continual drop for all blowing ratios. This trend presumably continues until the rounded off end of the vane (X/S ~ 65 or 66), an area at which the film cooling coverage begins to wear away due to the effects of periodic shedding.

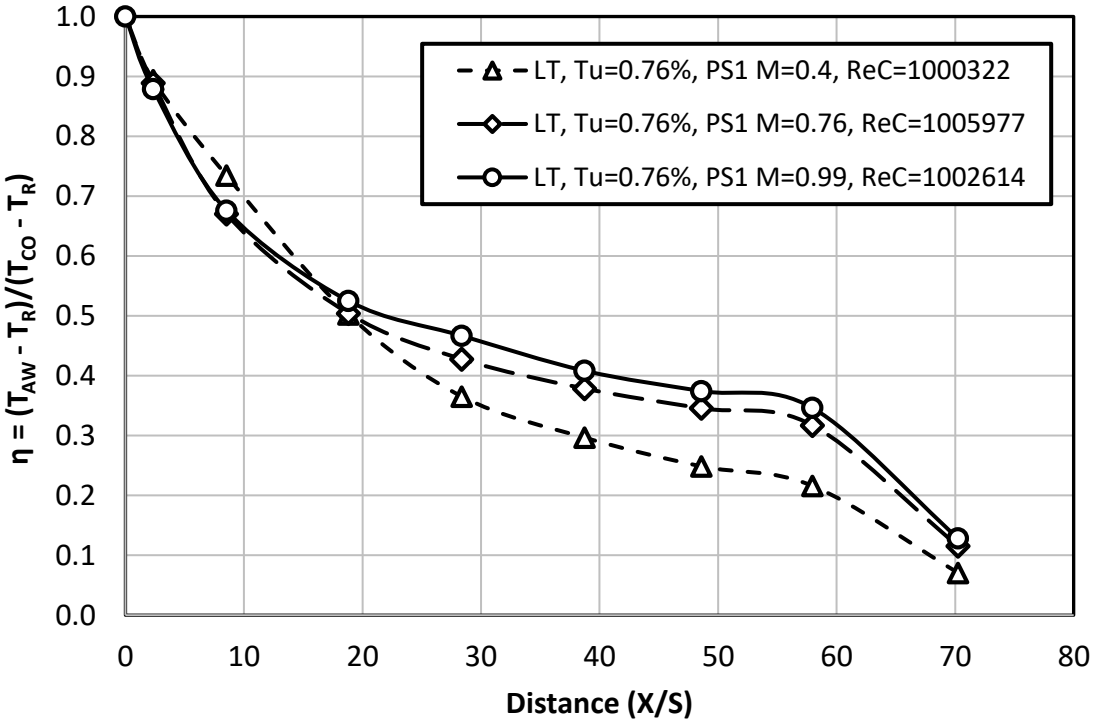


Figure 38. LT pressure side distributions showing influence of BR, $Re_C$ = 1,000,000.

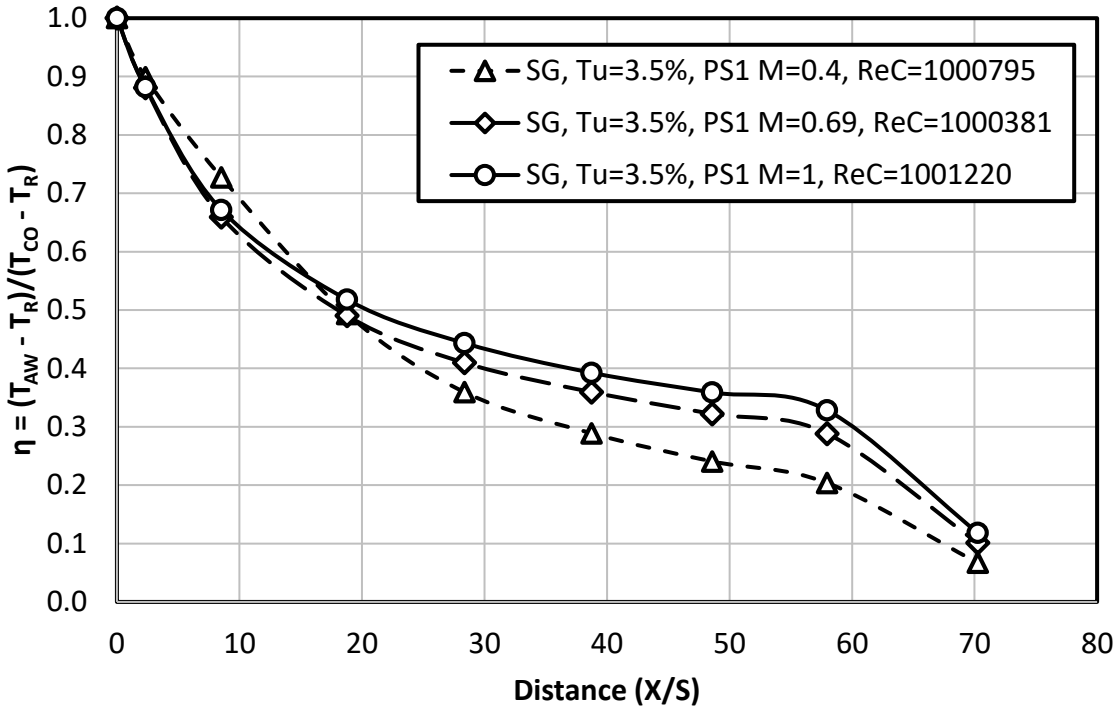


Figure 39. SGF pressure side distributions showing influence of BR, $Re_C$ = 1,000,000.

Adiabatic effectiveness distributions recorded at a $Re_C$ of 1,000,000 with the small grid far turbulence condition (Tu = 3.5%) can be viewed in Figure 39

. Similar to the low turbulence condition, initial rapid decay downstream of the slot is observed. Although the behavior downstream of the slot appears the same as at the low turbulence condition, the effectiveness levels are somewhat lower in Figure 39 than those in Figure 38 are. The difference is subtle but quantifiable which suggest the turbulence is influencing the flow regime at this modest turbulence level. Examining Figure 40, the film cooling distributions at the large grid turbulence condition (Tu = 8.0%) are hardly differentiable when compared to those seen in Figure 38 and Figure 39. However, the overall effectiveness values are slightly lower and the difference between the values for the lowest blowing ratios compared to the highest blowing ratios can be

interpreted as widening.

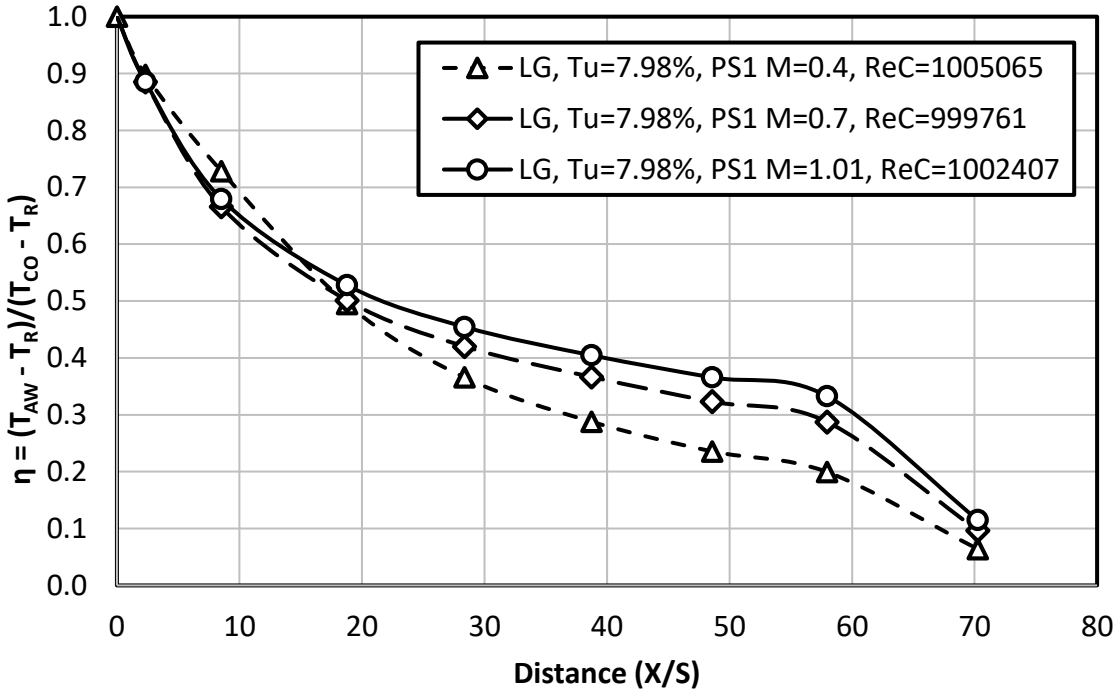


Figure 40. LG pressure side distributions showing influence of BR, $Re_C$ = 1,000,000.

The turbulence influence on effectiveness distributions at $Re_C$ of 1,000,000 and the aerocombustor (AC) turbulence condition (Tu = 13.0%) are more pronounced, as seen in Figure 41. The immediate drop in effectiveness near the slot is more consistent from one blowing ratio to another and further away from the slot the distributions fan out a greater amount than at lower turbulence levels. Figure 42 displays the effectiveness distributions for the high turbulence (HT) mock combustor (Tu = 17.4%) at a $Re_C$ = 1,000,000. The general trend of initial rapid decay and greater impact of turbulence associated with variation in blowing ratio as previously noted with increases of turbulence level is also observed here.

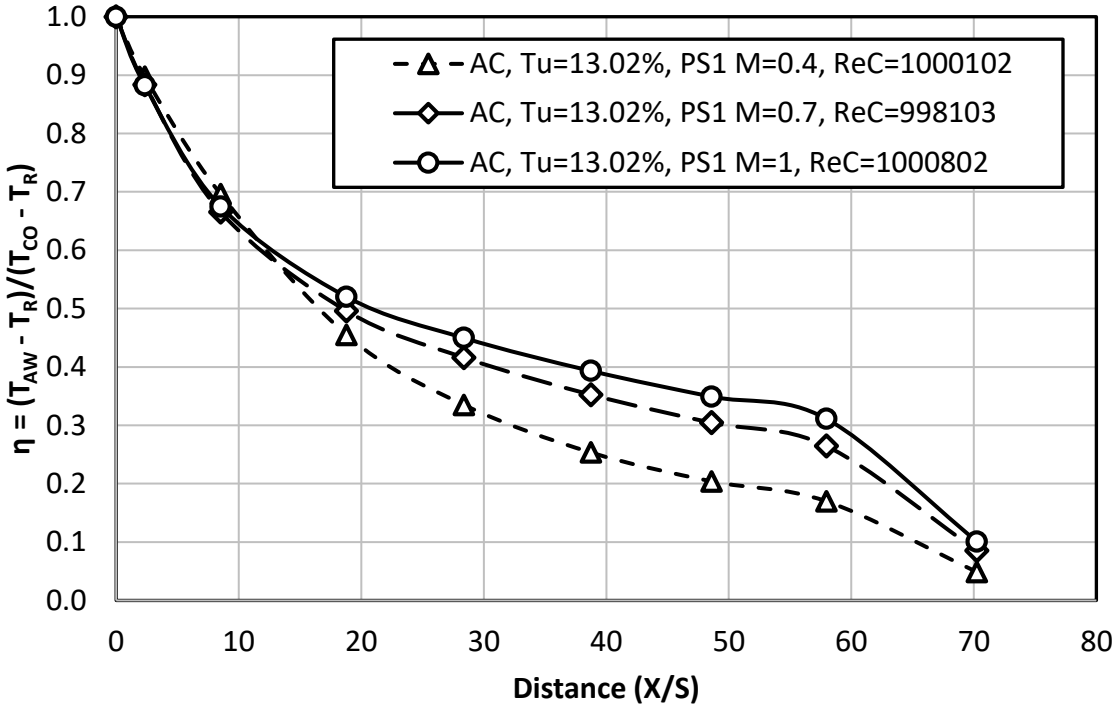


Figure 41. AC pressure side distributions showing the influence of BR, $Re_C$ = 1,000,000.

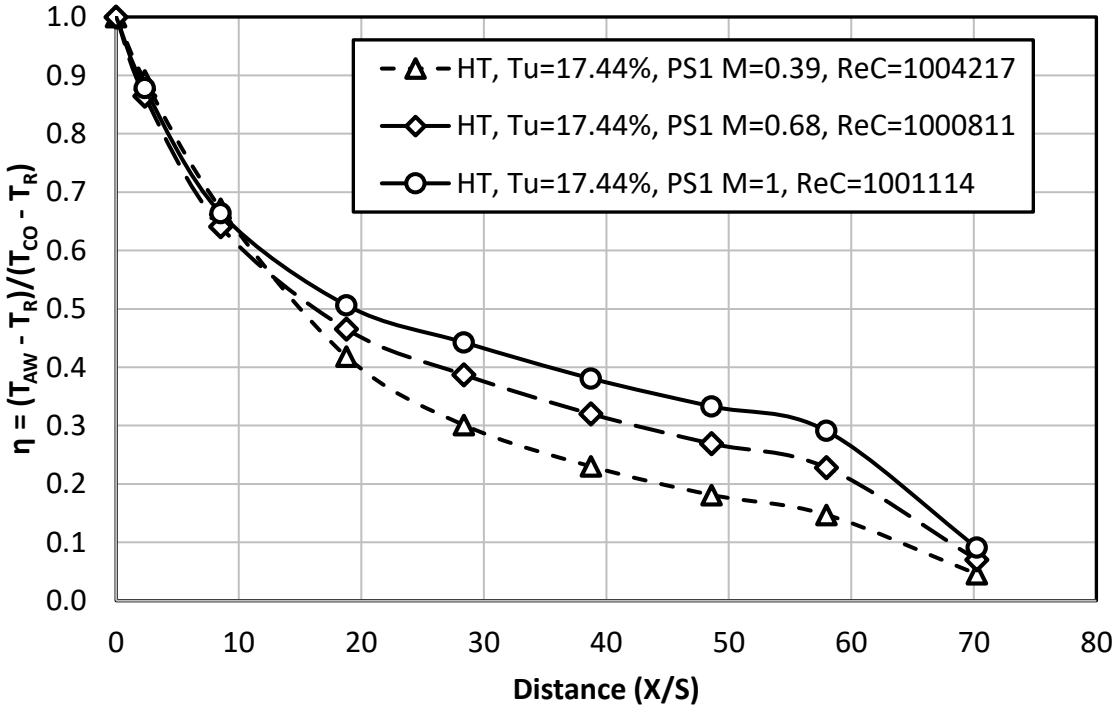


Figure 42. HT pressure side distributions showing the influence of BR, $Re_C$ = 1,000,000.

The preceding figures display a rapid decay of film cooling effectiveness downstream of the coolant slot, which indicates a lack of an initial jet region and that there is and the seemingly immediate interaction of the freestream across the film layer. Using LES calculations, Kanani et at. [4] described how rapid dissipation of the downstream film layer of Busche et al. [1] was due to the inner structures within the plenum. Vital to keeping the downstream ledge of the plenum cool, the current study includes impingement jets following the last row of pedestals that further manipulate flow. Conversely, one can envision the impingement jets producing wall jets interacting with horseshoe vortices originating from the leading edge of upstream pins to bolster the vortical motion while augmenting discharge slot velocity variations. Ostensibly, the vorticity, velocity variations and turbulence in discharged flow from the slot creates an initial mixing region controlled by inflow conditions from the slot. The effectiveness distribution may also be effected by the turbulence external to the plenum. In any case, the influence of the external turbulence seems to be graduated and continuous over the complete surface.

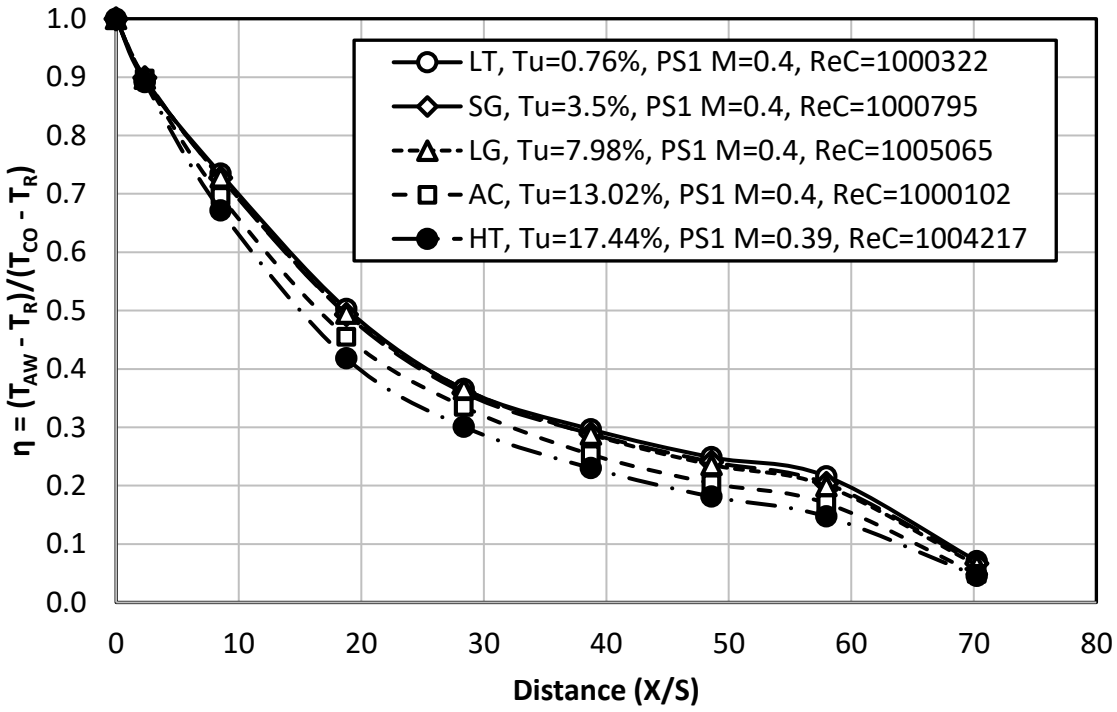


Figure 43. Influence of turbulence on suction side, $Re_C$ = 1,000,000, $M_{PS1}$ = 0.4.

The influence of turbulence becomes more apparent when investigating all five turbulence conditions at one blowing ratio and exit chord Reynolds number. Figure 43 displays the effectiveness distributions plotted over dimensionless distance from the slot (X/S) at blowing ratios set nominally to 0.4 and Reynolds numbers maintained at 1,000,000. The reduction of film cooling effectiveness increases with distance from the slot, which is most apparent when viewing the two highest turbulence levels. The ratios of the two highest turbulence levels compared to those of the lowest turbulence levels are 0.95, and 0.91 near the slot exit and 0.69, and 0.64 near the trailing edge, respectively. The film cooling distributions are visibly more effected by the large scale and high intensity of the mock aerocombustor turbulence case than the grid-generated turbulence. The dynamic mixing of the inflow conditions stemming from the slot is likely responsible for the greater influence. Analogous effectiveness trends at the next higher blowing ratio

of 0.7 are shown in **Error! Reference source not found.** on the following page, having ffectiveness ratios of 0.88, 0.84, 0.74, and 0.61 between the higher and low turbulence condition. Compared to Figure 43, there is a noticeable difference in the initial decay region, where the external turbulence seemingly has a less significant influence on effectiveness distributions. Figure 45 displays the uppermost tested blowing ratio, M = 1.0. The effectiveness decreases, but to a lesser degree than those at lower blowing ratios having higher to lower effectiveness ratios of 0.92, 0.90, 0.79, and 0.71. The effectiveness in the initial decay region for the conditions is influenced less than those observed at the next lower blowing ratio. The effectiveness trends were contrasted over the full range of external turbulence levels tested and suggest the effect of the inflow turbulence and vorticity from the slot is the predominate influence. The inflow fluid dynamics appears control the initial mixing between the coolant discharge and the freestream. Inlet turbulence seemingly has an additive impact as blowing ratios are increased.

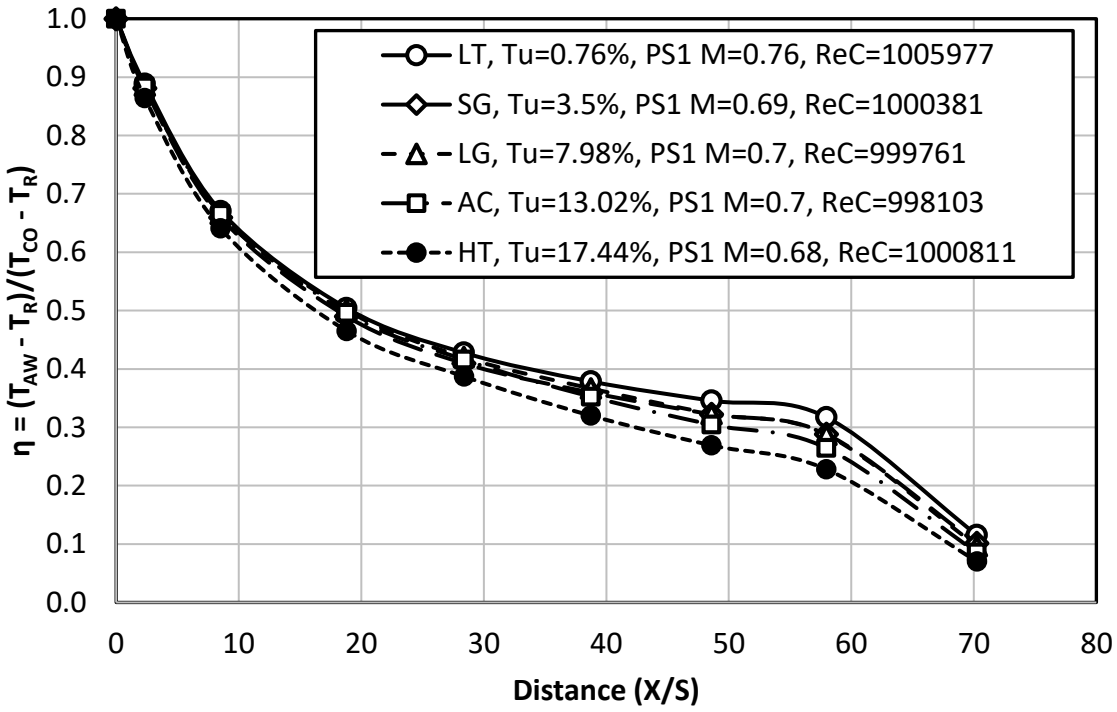


Figure 44. Influence of turbulence on pressure side, $Re_C$ = 1,000,000, $M_{PS1}$ = 0.7.

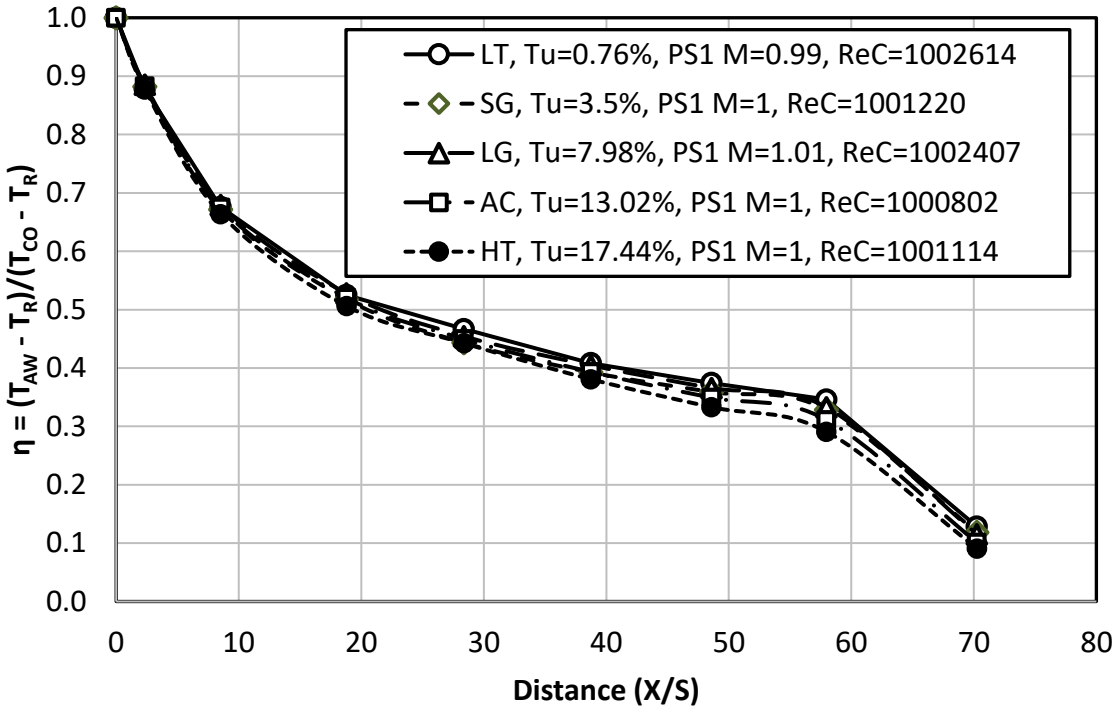


Figure 45. Influence of turbulence on pressure side, $Re_C$ = 1,000,000, $M_{PS1}$ = 1.0.

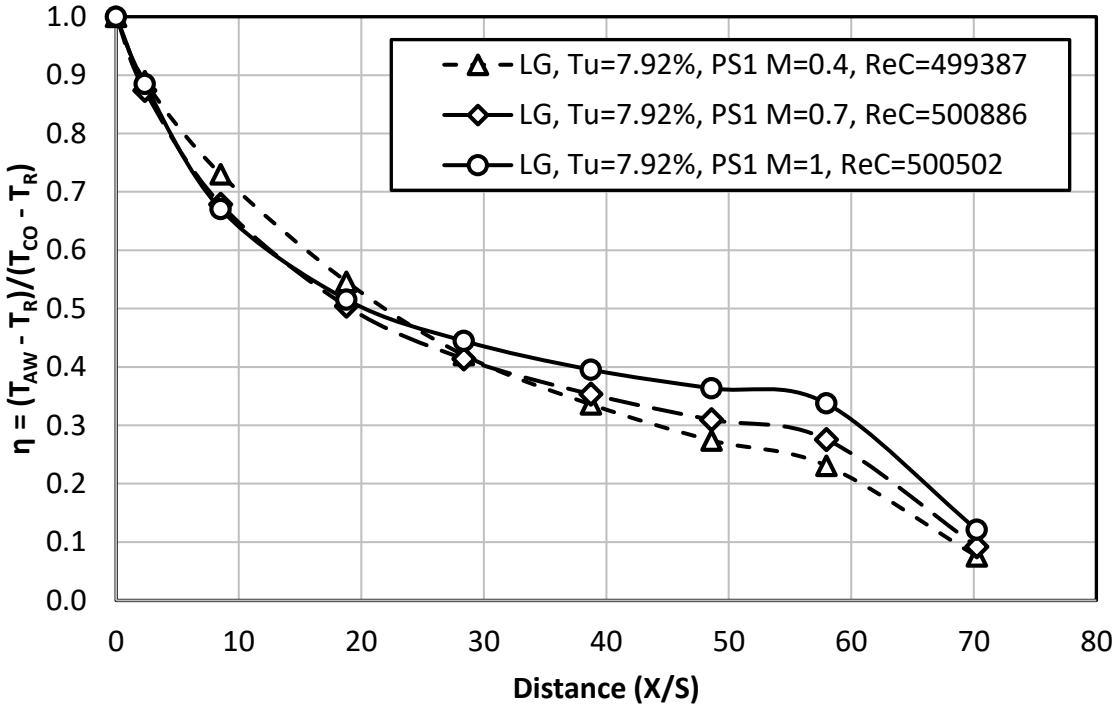


Figure 46. LG distributions showing the influence of BR at $Re_C$ = 500,000.

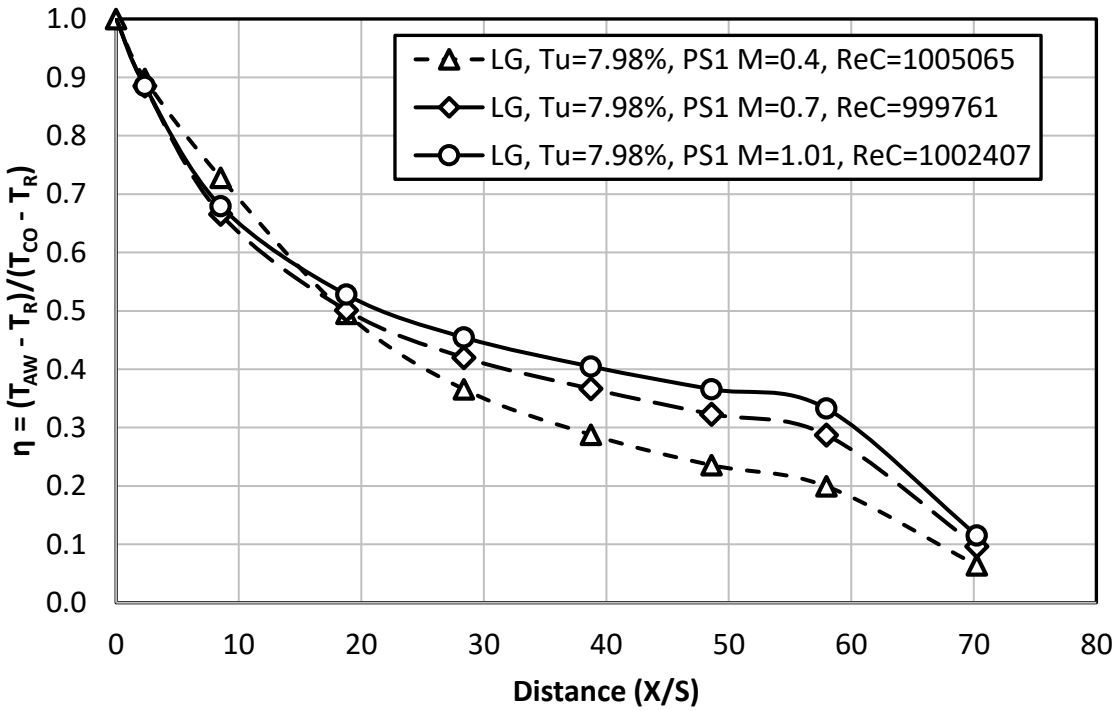


Figure 47. LG distributions showing the influence of BR at $Re_C$ = 1,000,000.

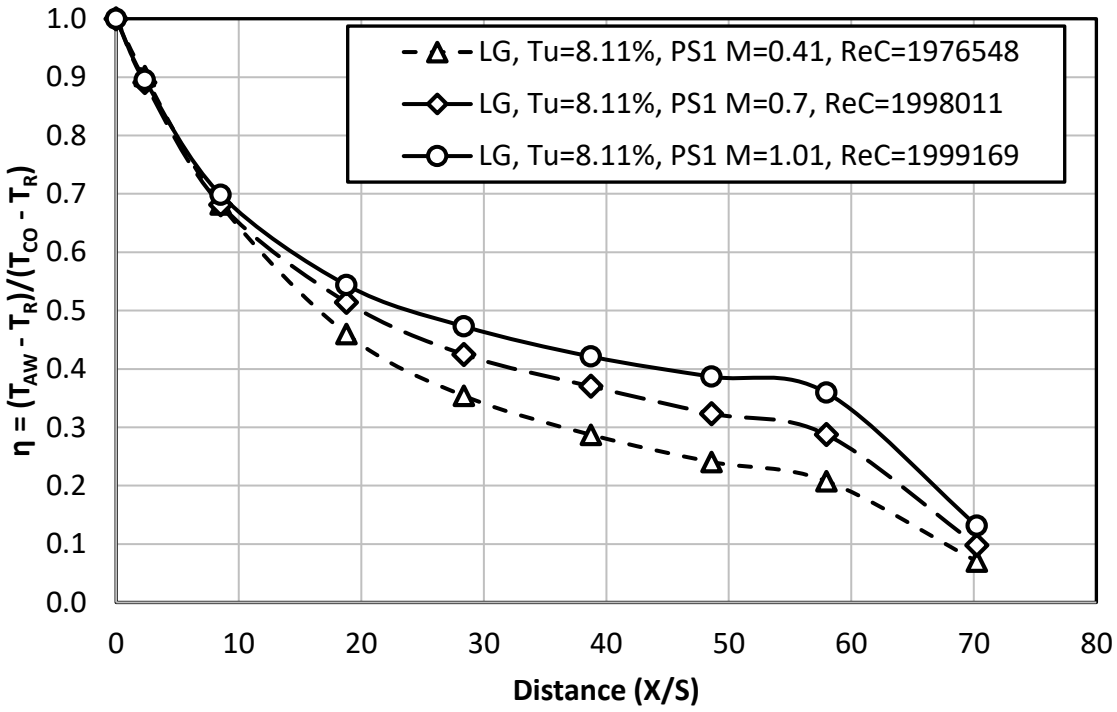


Figure 48. LG distributions showing the influence of BR at $Re_C$ = 2,000,000.

In a previous study by Busche et al. [1], the effectiveness distributions near the slot discharge area were substantially impacted by Reynolds number. Busche observed that near slot film cooling levels were improved by presence of laminar and transitional boundary layers when contrasted to turbulent flow. Effectiveness distributions at three blowing ratios ($M_{PS1}$ = 0.4, 0.7 and 1.0), and the large grid turbulence condition (Tu = 7.9%) are plotted separately at three Reynolds numbers ($Re_C$ = 500,000, $Re_C$ = 1,000,000 and $Re_C$ = 2,000,000 ). The data recorded at $Re_C$ = 500,000 is displayed in Figure 46 showing the effectiveness level at the smallest blowing ratio ($M_{PS1}$ = 0.4) is heightened which may be due to surface flow with laminar characteristics. A more modest variation in effectiveness with respect to blowing ratio is noted at a $Re_C$ = 1,000,000 as seen in Figure 47; however, the near slot region shows an improvement in effectiveness at the

lowest blowing ratio. Data for the highest Reynolds number (2,000,000) is presented in Figure 48, which shows more uniform effectiveness levels near the slot and a wider separation in downstream effectiveness. This is expected, as larger Reynolds numbers are associated with thinner boundary layers that normally generate higher levels of effectiveness.

An understanding of the effect of Reynolds number on effectiveness is made clearer by contrasting all three Reynolds numbers at the same blowing ratio and turbulence condition. The film cooling distributions for the lowest blowing ratio of 0.4 and the small grid far turbulence condition can be viewed **Error! Reference source not ound.**. The lowest Reynolds number (500,000) yields the highest cooling effectiveness, which is explained well by the mass addition conceptual model in which the film cooling is intermingled through the expanding boundary layer. The boundary layer is laminar at $Re_C$ = 500,000 that allows for the 0.4 blowing ratio to have a stabilizing effect by providing a shearing velocity gradient. Laminar boundary layer thickness increases with distance less than that of turbulent flow, which provides a mechanism for effeteness to remain higher. The variance in effectiveness displayed in **Error! Reference source not ound.** is very analogous with the other turbulence conditions tested. Conversely, for the aerocombustor turbulence (AC) condition seen in **Error! Reference source not found.**, he relatively high blowing ratio ($M_{PS1}$ = 1.0) becomes destabilizing to the boundary layer and increases the turbulence and vorticity from the slot. In addition, looking closely at this figure as surface distance increases, there is a subtle but visible gain for the highest Reynolds number cases which is what is predicted by widely accepted film cooling

models that connect higher Reynolds number to improved film cooling by way of turbulent boundary layer growth.

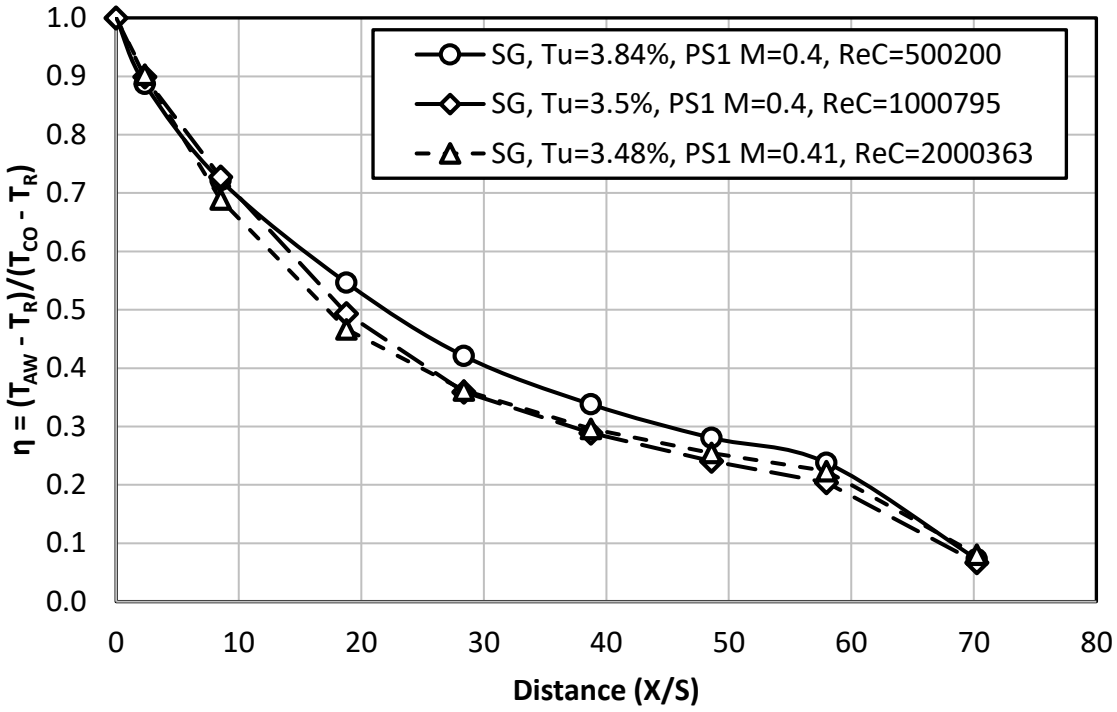


Figure 49. SGF distributions showing influence of $Re_C$ at $M_{PS1}$ = 0.4.

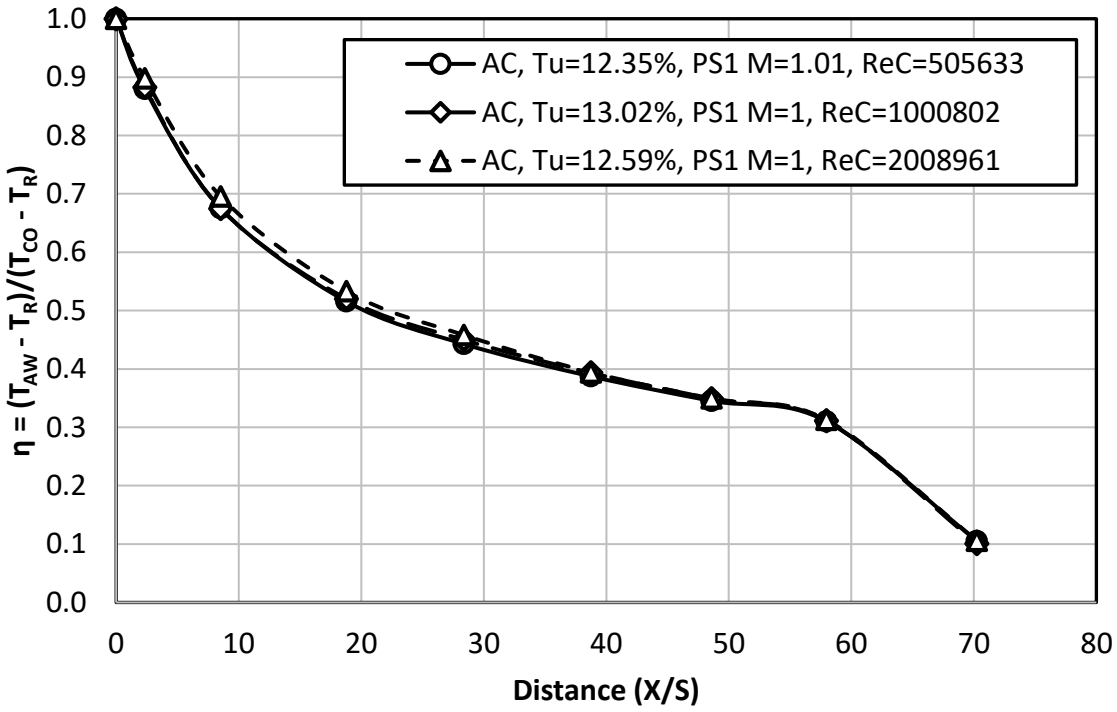


Figure 50. AC distributions showing influence of $Re_C$ at $M_{PS1}$ = 1.0.

Suction Surface Results

In an identical fashion to the pressure side, the flow through each coolant slot plenum must traverse three rows of high solidity pedestals prior to discharge. However, only the plenum nearest the leading edge (SS1) has a row of impingement jets integrated behind the last row of pedestals. Downstream, the second and third plenums (SS2 and SS3) emulate the internal geometry of the counter cooling sections of the representative vane design. Spanwise surface temperature measurements were acquired at the center impingement jet (center), the center breadth of the last row (right) and in between these two positions (left) as shown in shown in Figure 19 on page 36. As with the pressure side vane, these positions are approximated from different periodic flow locations. These distributions are almost uniform and thought to be more exact than the uncertainty

estimate associated with the incremental placement of the thermocouples. Therefore, the centerline temperatures accurately represent the average of the spanwise temperature readings and were plotted to create the streamwise film cooling distributions for the suction side.

**Suction Side Vane Spanwise Uniformity Measurements.** Spanwise Uniformity of Measurements were acquired over the span of the suction surface to verify centerline temperature are representative of spanwise averaged effectiveness. Suction side film cooling distributions at the three spanwise positions are presented in Figure 51 for the SGF turbulence condition at a nominal blowing ratios of $M_{SS1} = 0.5$, $M_{SS2} = 0.15$, and $M_{SS3} = 0.15$. Downstream effectiveness from the impingement jet (center) and the mid-breadth (right) was elevated compared to the between position (left). This variation in spanwise effectiveness reveals the tendency for vorticity from impingement jets and horseshoe vortices from the pins to cause some notable unevenness in the spanwise film cooling coverage at higher blowing ratios. After a distance of X/S of 150, only centerline data was acquired. For this reason, the following effectiveness distributions are based on the centerline locations and are believed to be closely representative to the spanwise averaged effectiveness.

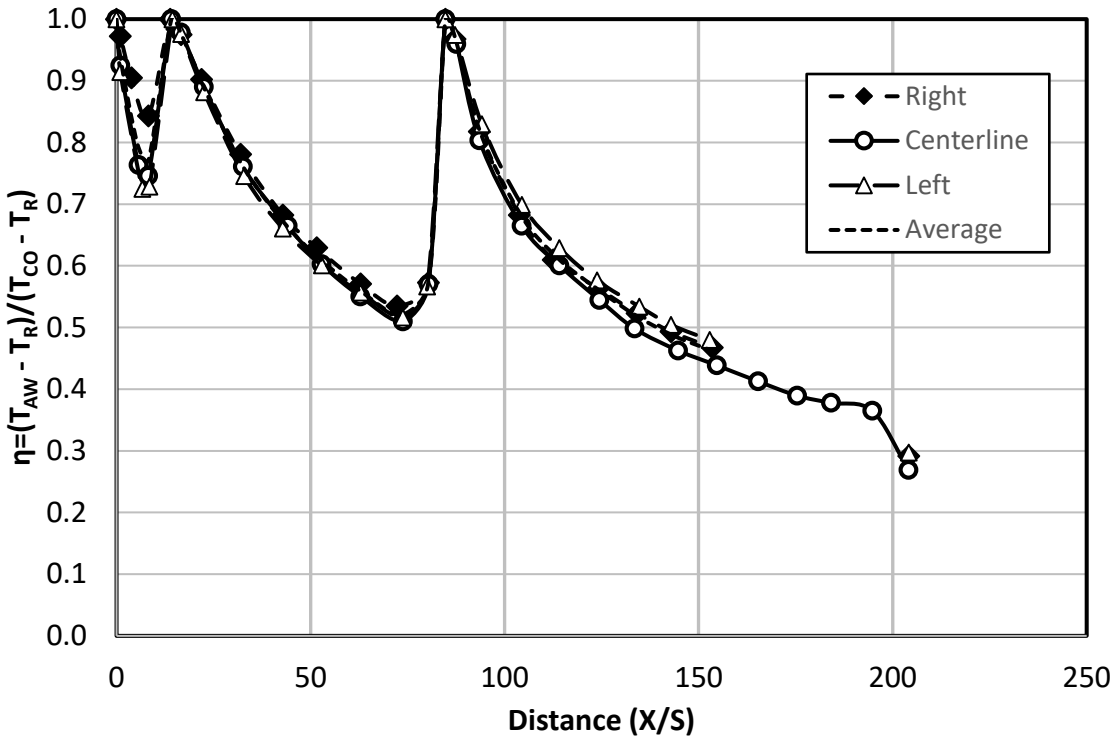


Figure 51. Suction side SGF streamwise distribution at $Re_C$ = 1,000,000, $M_{SS1}$ = 0.5, $M_{SS2}$ = 0.15, and $M_{SS3}$ = 0.15

**Effects of Blowing Ratio at Increasing Turbulence levels.** Suction surface adiabatic film cooling effectiveness distributions downstream of three coolant slots were recorded. These data were acquired to analyze the stagnation area that is aft of the exit of the incremental impingement section slot and the remaining downstream suction surface cooled by cooled by two counter cooling sections. Four inlet turbulence levels (0.7%, 3.5%, 7.9%, and 12.6%) and three exit chord Reynolds numbers (500,000, 1,000,000 and 2,000,000) were chosen for testing. To limit the number of tested permutations, only two blowing ratios were tested for each slot and data for individual slot film cooling effectiveness was limited to two turbulence levels. The film cooling results are presented as spanwise average cooling distributions to capture the trends within this generous amount of data. Cooling distributions covering the entire span that were acquired with

the IR cameras are presented to depict the comparative spanwise uniformity and capture the impact of the passage vortex on suction surface film cooling effectiveness.

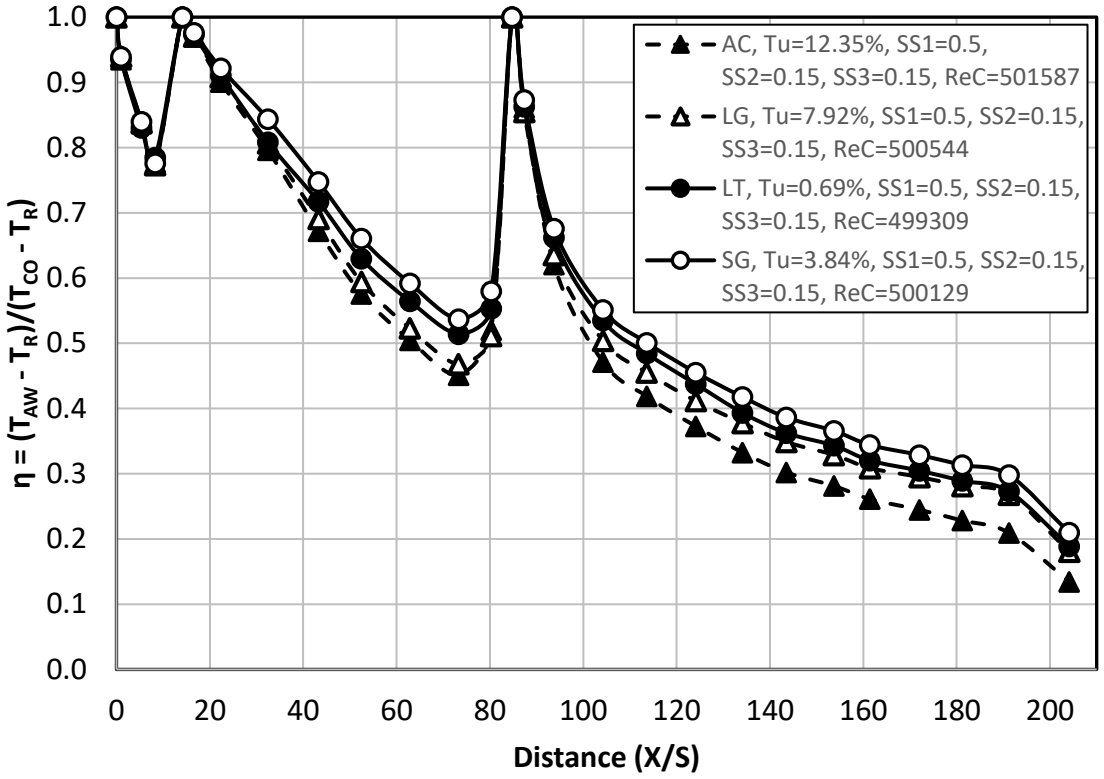


Figure 52. Influence of BRs ($M_{SS1}$ = 0.5, $M_{SS2}$ = 0.15, $M_{SS3}$ = 0.15) on film cooling distributions for various turbulence conditions at $Re_C$ = 500,000.

Multifaceted cooling schemes are developed not only to keep turbomachinery components under critical failure temperatures, but also to maintain tolerable temperature differences across components to meet desired fatigue life considerations. The film cooling distributions at all four inlet turbulence conditions tested with a Reynolds number of 500,000 at the lowest respective blowing ratios are presented in Figure 52. An ample amount of film cooling protection is displayed over the entire suction surface with relatively high effectiveness values downstream of the first two slots and substantial

cooling values downstream of the last coolant slot. There is even a reasonably substantial amount of film coverage left over the trailing edge. The effects of turbulence intensity on film cooling coverage can be seen, most notably in the downstream region where the value at the highest turbulence level approximately 2/3$^{rds}$ the value when compared to the lowest turbulence condition. A comparable trend with slightly higher effectiveness values is observed with higher downstream slot blowing ratios at the same Reynolds number (500,000) and turbulence conditions, which is shown in Figure 53.

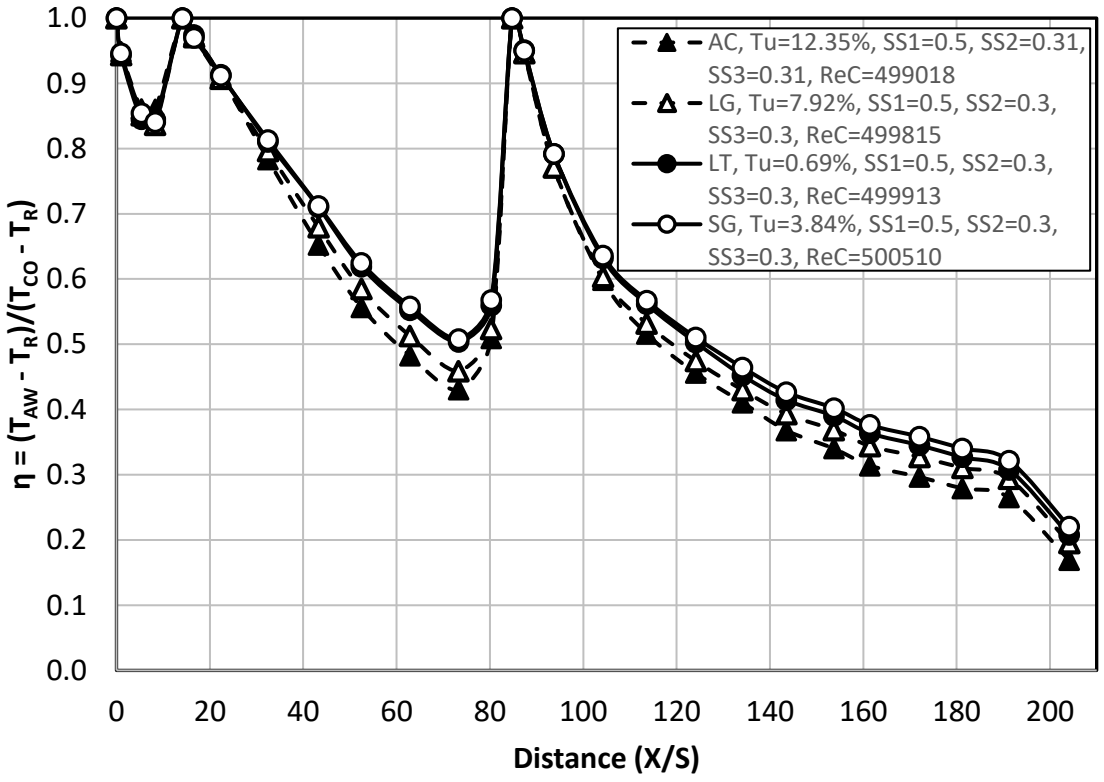


Figure 53. Influence of BRs ($M_{SS1}$ = 0.5, $M_{SS2}$ = 0.30, $M_{SS3}$ = 0.30) on film cooling distributions for various turbulence conditions at $Re_C$ = 500,000.

The impact varying blowing ratios while combining flow from all three suction surface coolant slots at $Re_C$ = 1,000,000 and the AC turbulence condition is shown in

Figure 54. As expected, the highest effectiveness levels are observed at the highest blowing ratios and the lowest effectiveness levels at the lowest blowing ratios. It is also observed that the first slot (SS1) at the lowest blowing ratio setting and the downstream slots (SS2 and SS3) at the highest blowing ratio settings produces higher produces higher film coverage values than when the converse blowing ratio settings are applied. These displayed data show effectiveness varies notably with changes blowing ratios, which is particularly apparent when comparing the AC turbulence condition to other tested turbulence conditions.

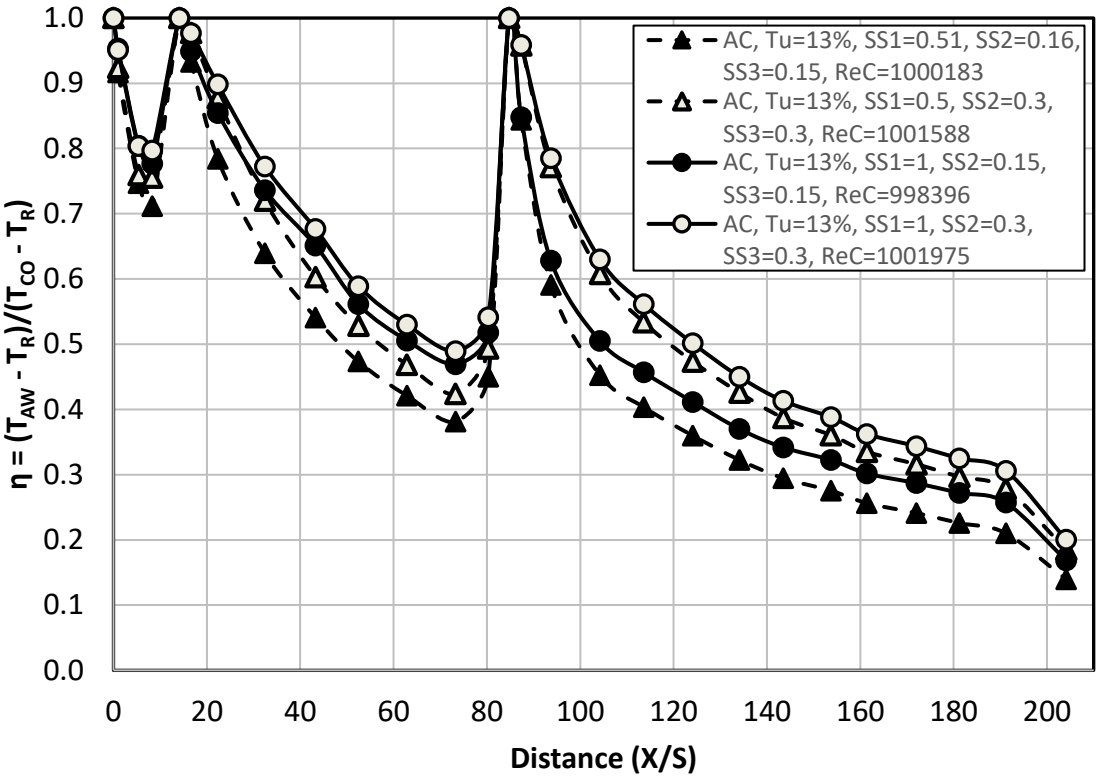


Figure 54. Influence of BR on film cooling distributions for the AC turbulence condition at $Re_C$ = 1,000,000.

Turbine blade cooling schemes usually consist of both internal and external cooling methods that are individually developed to cool specific areas along the blade surface. It is helpful to examine each or these areas, or regions, by itself to determine if adequate external film protection is present.

Figure 55 is displays the film cooling effectiveness with coolant air supplied solely to slot SS3, located furthest downstream, at blowing ratios of 0.15 and 0.30, and AC and SGF turbulence conditions. There is a slight reduction in effectiveness for the AC turbulence condition compared to the small grid far turbulence condition; however, the blowing ratio in this region has a much greater influence.

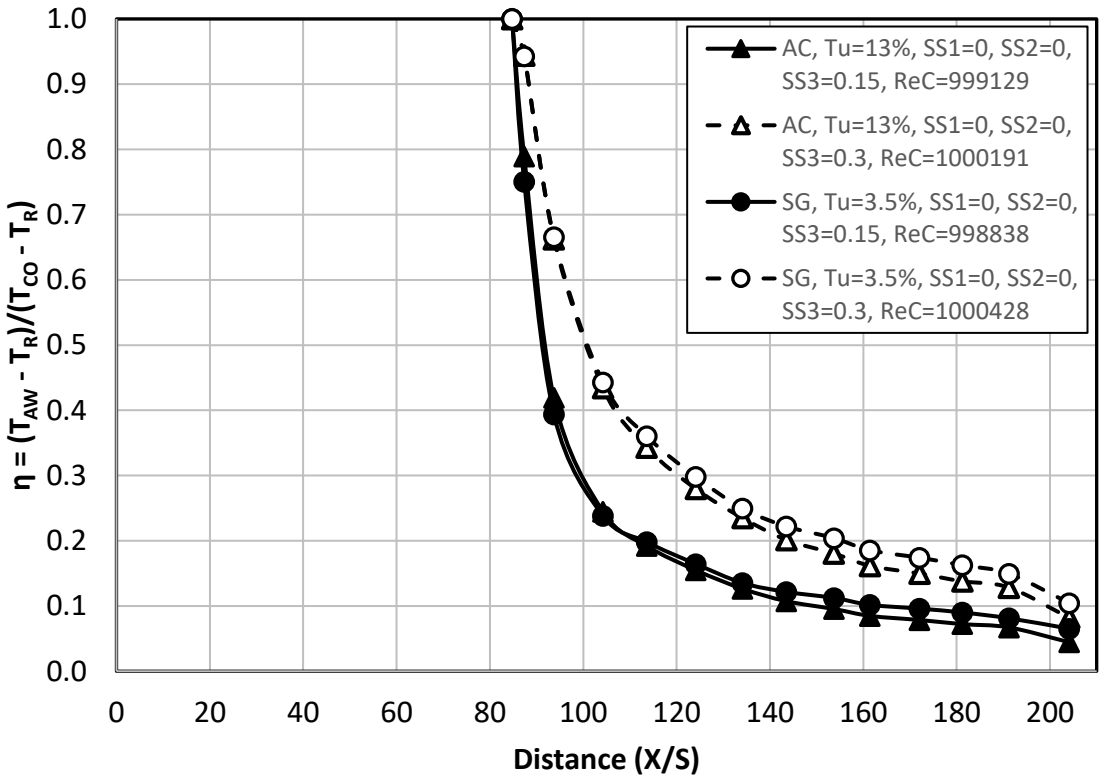


Figure 55. Influence of blowing ratio and turbulence conditions for middle slot (SS3), $Re_C$ = 1,000,000, AC and SGF, $M_{SS3}$ = 0.15 and 0.30.

Data collected with coolant air pushed through the middle slot (SS3) only at an $Re_C$ = 1,000,000 is displayed in Figure 56. Again, blowing ratios of 0.15 and 0.30 with AC and SGF turbulence conditions are shown for comparison. Similar to Figure 55, there is a slight reduction in effectiveness for the AC turbulence condition and the blowing ratio in this region has a much more dominate effect. The impact of the turbulence is more noticeable, especially further downstream from the slot.

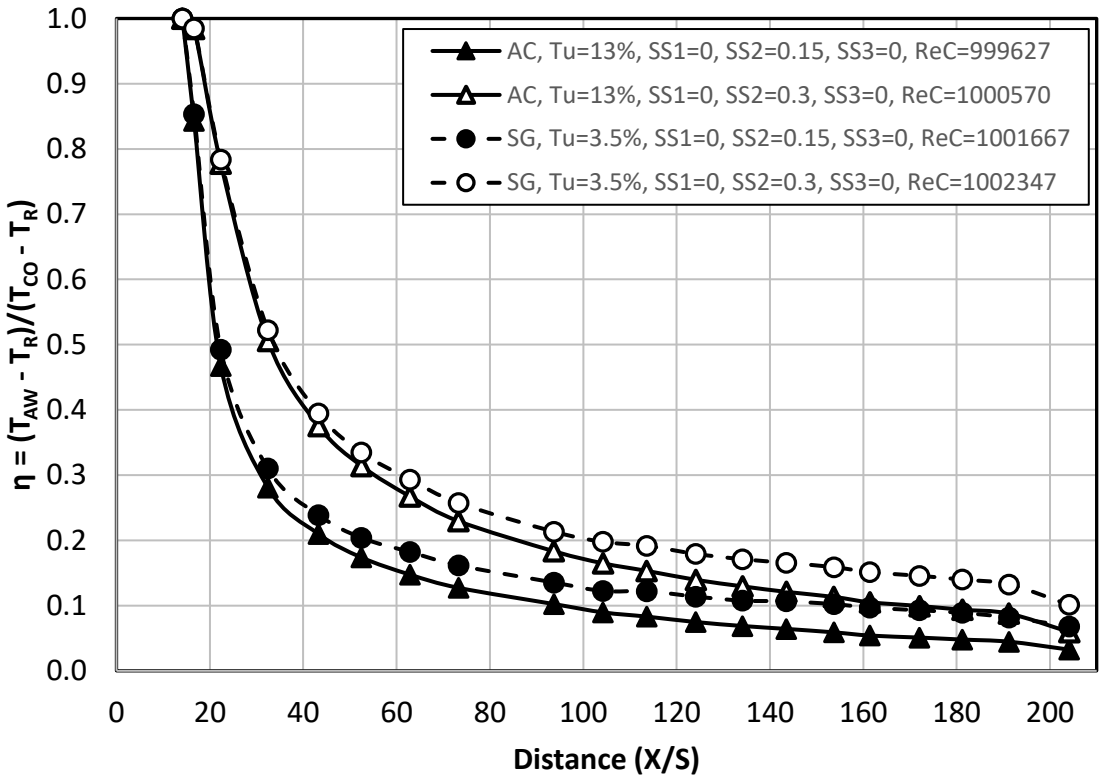


Figure 56. Influence of blowing ratio and turbulence conditions for middle slot (SS3), $Re_C$ = 1,000,000, AC and SGF, $M_{SS2}$ = 0.15 and 0.30.

The third comparison of blowing ratio and turbulence condition effects can be seen in Figure 57, which displays effectiveness coolant air flowing through the upstream slot (SS1) alone. Here, the blowing ratios are much higher at $M_{SS1}$ = 1.0 and $M_{SS1}$ = 0.50

than those in Figure 55 and Figure 56, although the Reynolds number and turbulence conditions are the same. The local free-stream velocity of each slot is 78%, 94% and 105% of $U_{EXIT}$ for SS1 ($U_{SS1}$), SS2 ($U_{SS2}$), and SS3 ($U_{SS3}$), respectively. There is approximately 2.74 and 2.43 times more mass addition for the upstream slot compared the middle and downstream slot, respectively, at both the higher and lower blowing ratios. The higher mass addition produces notably higher effectiveness levels that lean towards slower initial decay; yet, the effect of turbulence is greatly pronounced for SS1 compared to SS2 and SS3. Higher blowing ratios from the upstream slot result in more irregular film distributions for the lower (3.5%) small grid far turbulence condition.

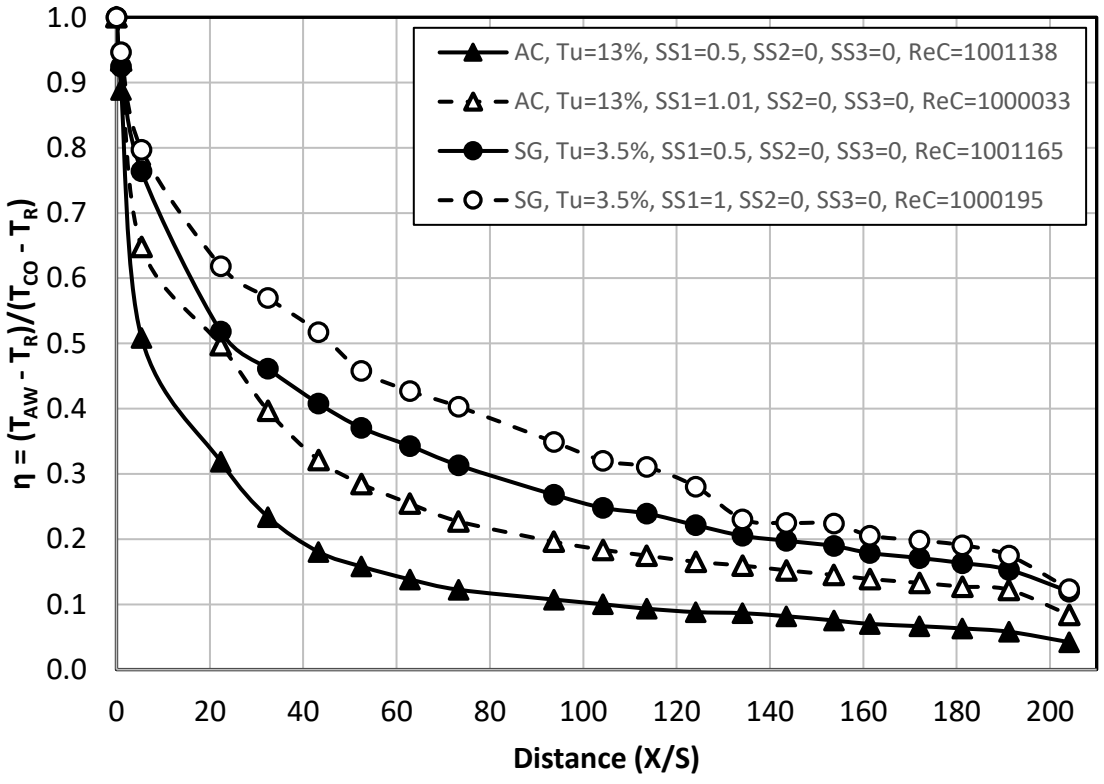


Figure 57. Influence of BR and turbulence conditions for upstream slot (SS3), $Re_C$ = 1,000,000, AC and SGF, $M_{SS1}$ = 1.0 and 0.50.

The Reynolds number effect on the film cooling distribution is generally limited in the current study. Considering the Goldstein and Haji-Sheikh's [50] model, a somewhat higher effectiveness level with higher Reynolds numbers would normally be expected given a turbulent boundary layer. The higher flows (Reynolds number) are thought to result in thinner boundary layers, which are assumed responsible for this effect.

**Effects of Reynolds Number at Given Turbulence Levels.** A contrast of effectiveness at all three exit chord Reynolds numbers for the SGF turbulence condition with a downstream slot (SS3) blowing ratio of 0.15 is given in Figure 58. The effectiveness increases notably in the near slot region for a $Re_C$ = 500,000 which can be understood when reviewing a previous study by Varty and Ames [3] that showed heat transfer outcomes with laminar flow on the suction surface. After X/S of 100, the precipitous drop in effectiveness is perhaps caused by transition from the boundary layer taking on low momentum fluid while entering a positive pressure gradient. The rapid decay of effectiveness in the near slot region for the $Re_C$ = 1,000,000 and 2,000,000 is expected considering the low blowing ratios. Past X/S of about 130, the effectiveness levels become relatively consistent; however, there is a slight elevation in effectiveness with higher Reynolds number.

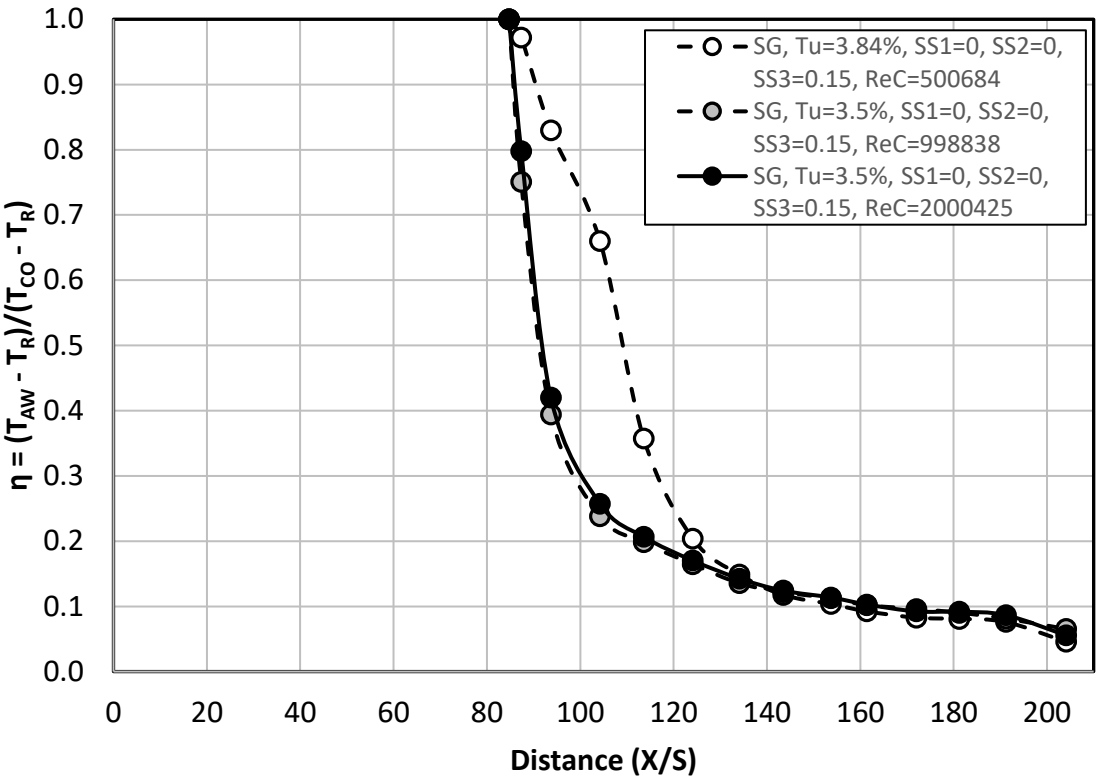


Figure 58. Influence of $Re_C$ for downstream slot (SS3), SGF, $M_{SS3} = 0.15$.

Figure 59 shows a set of data produced at the same parameters at those in Figure 58, except for having a blowing ratio $M_{SS3} = 0.3$. For the lowest Reynolds number the effectiveness is high in the near region to the slot but quickly decays to a level similar to the other two Reynolds numbers. Aside from this artifact, the influence of the Reynolds number is generally minimal when comparing all three trend lines.

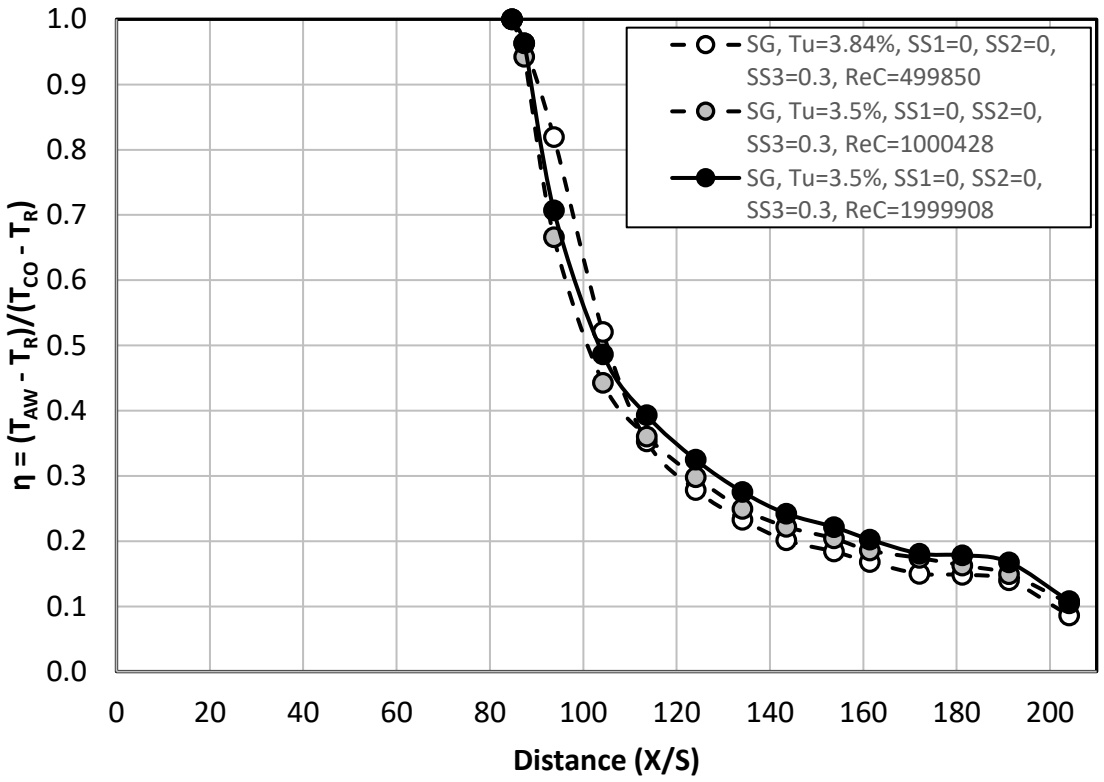


Figure 59. Influence of $Re_C$ for middle slot (SS2), SGF, $M_{SS3}$ = 0.30.

The effectiveness at the three tested exit chord Reynolds numbers for the small grid far (SGF) turbulence condition with middle slot (SS2) blowing ratios of 0.15 and 0.30 is plotted in Figure 60. When plotted, there is separation between the data from higher and lower blowing ratios, allowing for clear interpretation with all six trend lines included in a single figure. Looking at the lower blowing ratio data ($M_{SS3}$=0.15), the lowest Reynolds number again shows initial higher levels and quickly decays levels similar to the other two Reynolds numbers. With the exception of the first two data points, the effectiveness distributions at the higher blowing ratio ($M_{SS3}$=0.30) follow the same orderly pattern with a hierarchy that would be expected based on Reynolds number. Comparing the lower blowing ratio effectiveness to that of the higher blowing ratios, the

effect of the higher mass addition is very clear. The effectiveness is seemingly proportional to blowing ratio after an X/S of about 40. Notice, the data from thermocouples positioned between X/S of 73 and 94 are omitted due to the downstream slot (SS3) being taped over during testing.

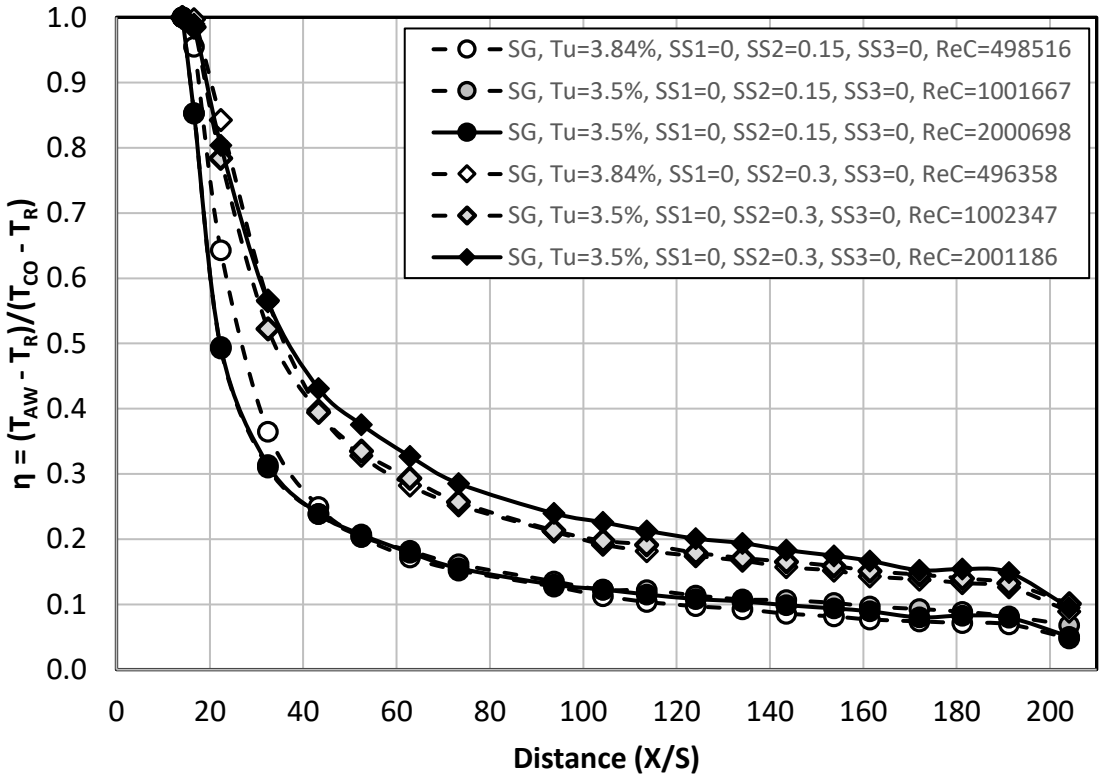


Figure 60. Influence of $Re_C$ for middle slot (SS3), SGF, $M_{SS3} = 0.15$ and $M_{SS3} = 0.30$.

Lastly, the Reynolds number influence on effectiveness is analyzed with an upstream slot (SS1) at a blowing ratio of $M_{SS1} = 0.5$ for the small grid far (SGF) turbulence condition as displayed in Figure 61. The lower blowing ratio for the upstream slot ($M_{SS1} = 0.5$ vice $M_{SS1} = 1.0$) is higher than the highest middle and downstream blowing ratio of 0.30. In addition, cooling air leaves the slot approximately 0.1085m from the stagnation point (Figure 34), which is a region of high acceleration.

Accelerating flows are proven to keep low Reynolds number flows laminar and improve film cooling which likely explains the higher effectiveness from the slot to and X/S of approximately 90.

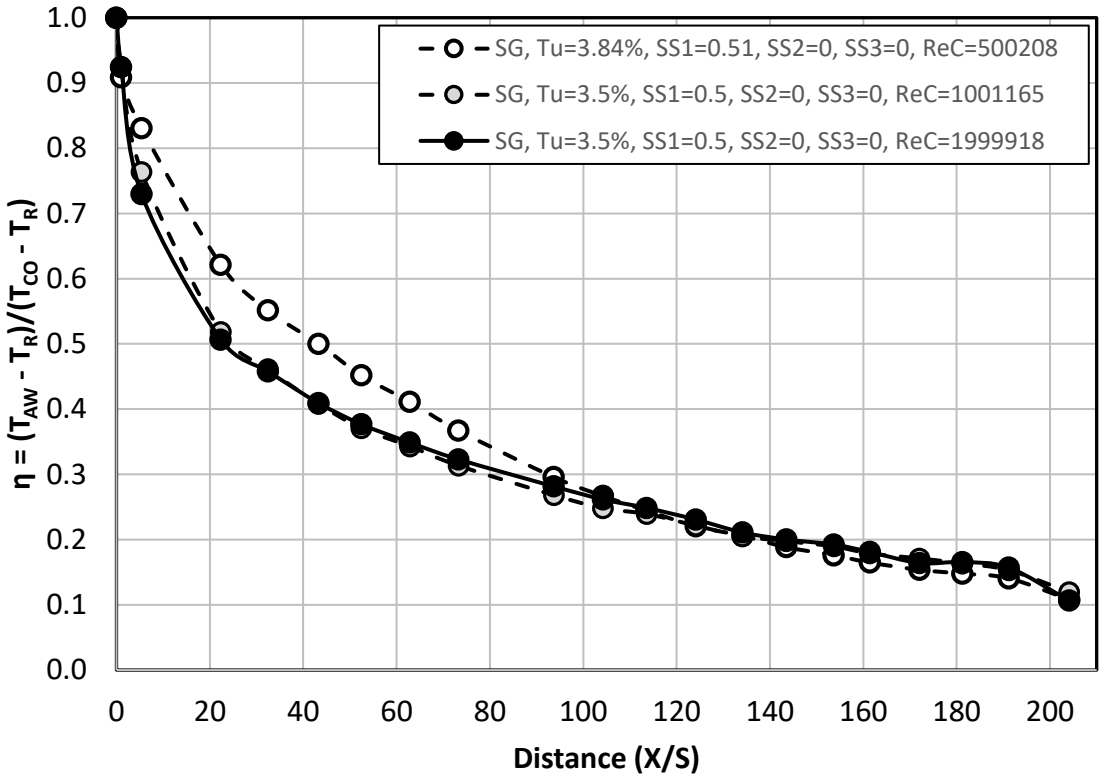


Figure 61. Influence of $Re_C$ for upstream slot (SS1), SGF, $M_{SS1} = 0.50$.

**Effects of Reynolds Number at Given Turbulence Levels with Superposition.** The property of superposition may be used with the thermal energy equation, as it is linear. Therefore, the combination of two or more inputs that produce individual outcomes is expected to produce the sum of the individual outcomes, or in other words, form a new solution. When applied to film cooling, superposition streamlines evaluation of the adiabatic wall temperature, which is the driving force for heat transfer. The following paragraphs presents superposition as it is applied in the present study.

The superposition plot of all three single slot blowing ratios ($M_{SS1}$ = 0.5, $M_{SS2}$ = 0.3 and $M_{SS3}$ = 0.3) for the Aerocombustor condition (AC) at an exit cord Reynolds number of 1,000,000 is displayed in Figure 62. The individual data of each single slot blowing ratio along with the integrated scheme of all three blowing ratios for the same conditions are also plotted for comparison. Compared to the integrated data, the superimposed data appears to be high between the first and second slot. The thermocouples adjacent and upstream to the middle and downstream plenums produce data the suggest conduction. The trend between the middle and downstream plenums mirrors the integrated data, but is slight low. Beyond the downstream slot, the superimposed data closely shadows the integrated data reasonably close. The superposition principal holds as long as the momentum equation does not change, altering the linear nature of the data. For this application, additional coolant air is added through two slots for the integrated cooling scheme compared to a single slot blowing ratio iteration. Therefore, the momentum equation is manipulated leading to inaccuracies in using superposition when the data from the single slot blowing ratios are superposed.

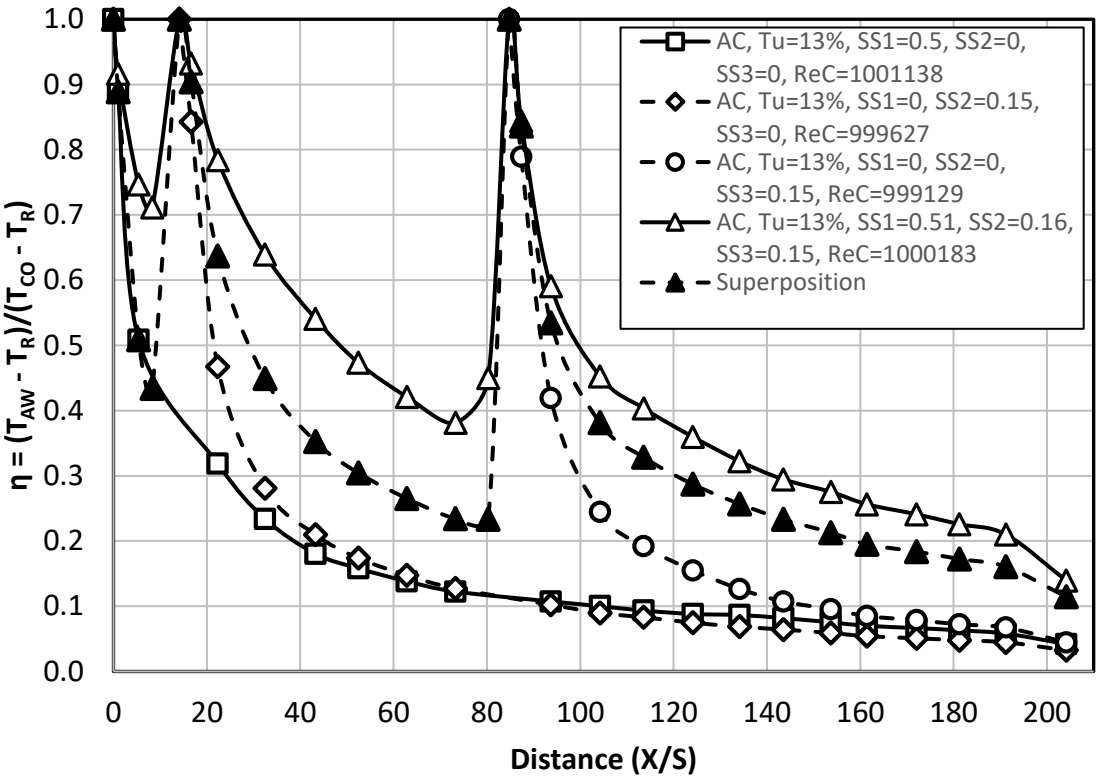


Figure 62. Influence of $Re_C$ on suction side under AC turbulence, $M_{SS1} = 1$, $M_{SS2} = 0.15$, and $M_{SS3} = 0.15$, including superposition plot.

Figure 63 makes a similar comparison as seen in Figure 62, except with the small grid far turbulence condition, a Reynolds number of 500,000, and downstream blowing ratios ($M_{SS2}$ and $M_{SS3}$) of 0.15, each. The flow preceding the third slot appears to undergo transition due to addition of upstream film that distinctly changes the boundary conditions. In addition, the superposition forecast is thrown off by the laminar behavior of the single slot data of SS3 near the exit of the downstream slot (SS3). As a result, the integrated film cooling distribution displays significantly less effectiveness near region aft of the slot.

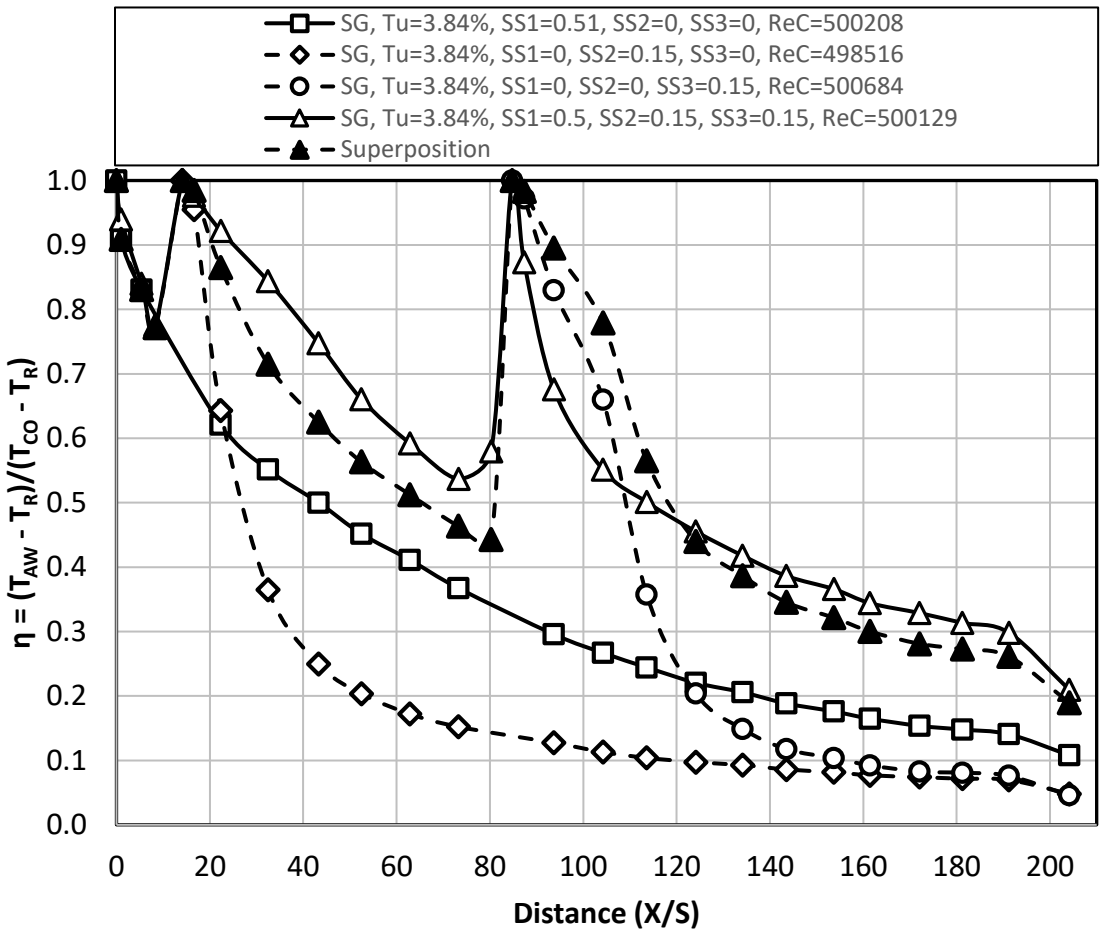


Figure 63. Influence of $Re_C$ on suction side under SGF turbulence, $M_{SS1}$ = 1, $M_{SS2}$ = 0.30, and $M_{SS3}$ = 0.30, including superposition plot.

**IR Camera Suction Side Vane Spanwise Surface Plots.** In general, the consistency of the film cooling coverage is relatively decent for the middle and downstream slot. However, spanwise variation in film cooling was evident at the highest blowing ratio for the upstream slot, particularly at the lower turbulence conditions, which warrants further investigation. The IR camera data provides media for visual interpretation to evaluate spanwise flow variations.

IR camera data were utilized to produce full surface film cooling effectiveness plots or film cooling contour plots. In these full surface figures, the lower IR camera position (Figure 11) picks up temperature profiles just downstream of the middle slot to the trailing edge, where film cooling effectiveness drops off. Laterally, the IR camera captures temperatures from the midspan to the endwall of the airfoil in both the upper and lower camera position. The upper IR camera position (also see Figure 11) records the surface temperature profiles further downstream with about a twenty to thirty pixel overlap with the lower IR camera, depending on the data run. The images were processed and merged together to produce full surface plots after calibration using thermocouple data. The emissivity correction displayed in Eq. 2, in appendix F, was incorporated into the calibration to minimize error due to radiation when needed. The overlapping data (between 0.4 and 0.45 meters) and camera "fish eye" effect (near the edges) sometimes resulted in slight distortions of the image; however, these distortions are minor, and if kept in mind, do not take away from the visualizing the trends.

The effects of secondary flows are apparent when viewing the bottom of the full surface contour plots which represents the region near the endwall. Each figure presents solid evidence of the "passage vortex in sweeping the film cooling away progressively in the region of the suction surface near the endwall" [45]. Secondary flows are believed to result from streamwise vorticity produced by vicious shear at the endwall and pressure gradients that develop along the flow path. The physics behind secondary flows is multifaceted and results from the synergy of several vortex systems. As categorized by Sieverding [51], the horseshoe vortex, the passage vortex, and the counter vortex comprise the three prominent vortices that exist in blade passages. The horseshoe vortex is comprised

of a two legs: the pressure side and suction side. The Langston [52] model can be viewed in Figure 64, which implies the leading edge vortex (horseshoe) is formed due to boundary layer separation and moves between the blades with a rotation oriented in the reverse direction. As the passage vortex meets the endwall, it engulfs mainstream flow between the blades. The counter vortex is far smaller and exists where the suction surface and endwall intersect. The effects of secondary flows should be considered when observing the following film cooling contour plots.

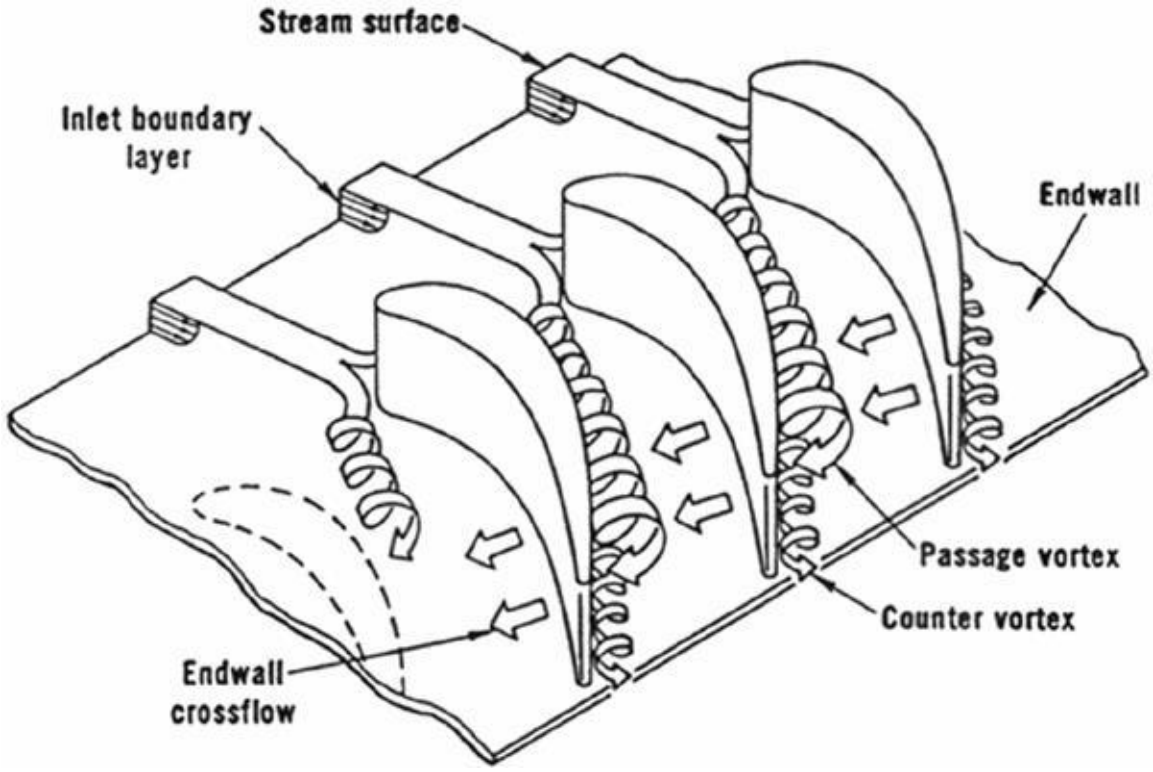


Figure 64. Depiction of endwall vortices as denoted by the Langston et al. model [52]

The full surface film cooling effectiveness at and $Re_C$ = 1,000,000 with the AC turbulence condition at blowing ratios for the upstream, middle and downstream slot of $M_{SS1}$ = 0.5, $M_{SS2}$ = 0.3 and $M_{SS3}$ = 0.3, respectively, is presented in Figure 65. There is

good uniformity upstream and downstream of the third slot (SS3). The sweeping effect of the passage vortex is evident as the film cooling layer is being carried away progressively in the region of the suction surface near the endwall (at the bottom of the figure).

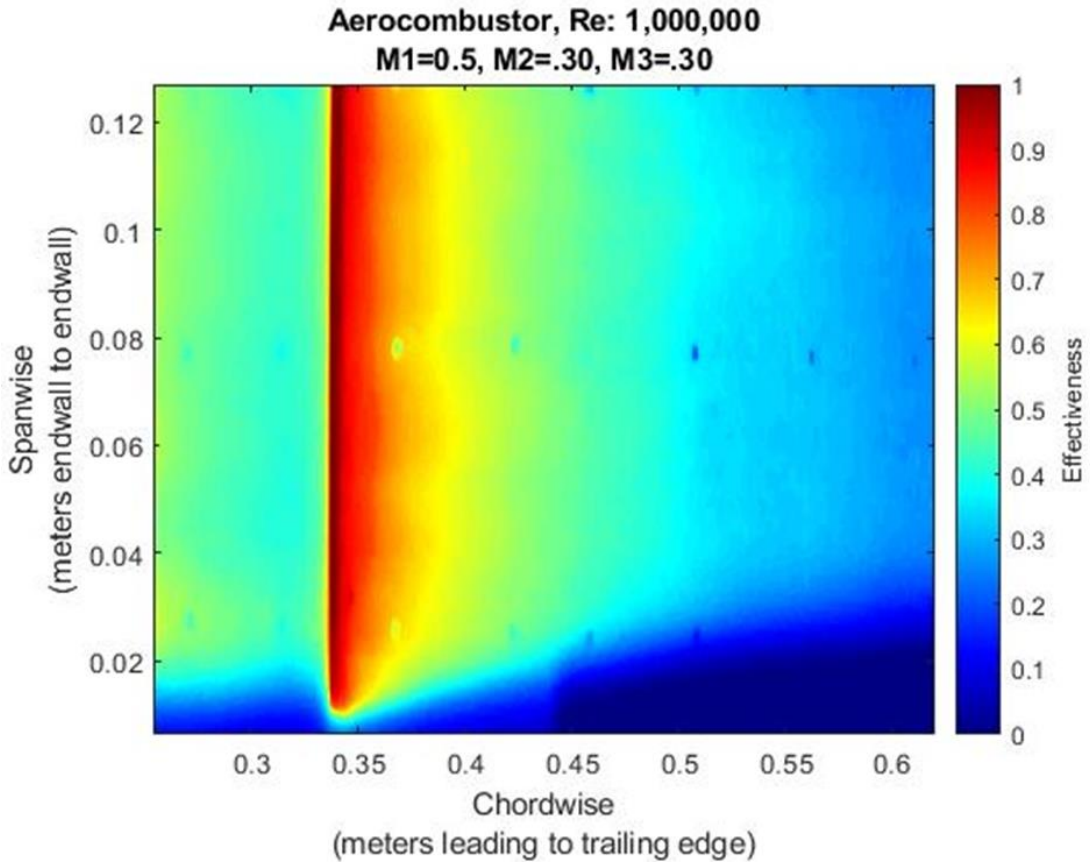


Figure 65. Contour plot of suction surface film cooling, $Re_C$ = 1,000,000, AC, $M_{SS1}$ = 0.5, $M_{SS2}$ = 0.3, $M_{SS3}$ = 0.3.

Figure 62 and Figure 65 both show the suction surface film cooling distribution at midspan of the vane while Figure 66 shows the correlation between these data. There is obviously a strong agreement between the thermocouple data points, in red, and the IR camera distribution in black. This lends credence to the trend data; however, it should be kept in mind that the thermocouple data was used to calibrate the magnitude of the IR

camera results. At a minimum, the data present a good two-dimensional visual representation of spanwise flow variation to complement the thermocouple data.

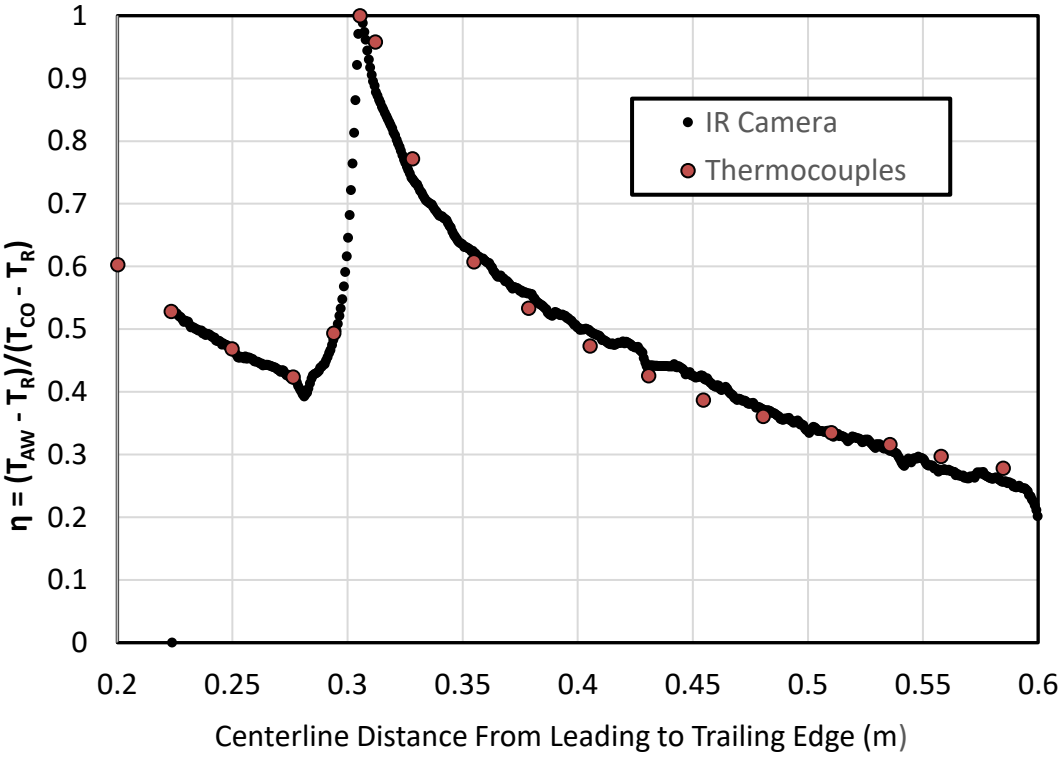


Figure 66. Centerline plot of IR camera temperature distribution compared to thermocouple measurements, suction surface film cooling, $Re_C$ = 1,000,000, AC, $M_{SS1}$ = 0.5, $M_{SS2}$ = 0.3, $M_{SS3}$ = 0.3.

Another full surface film cooling effectiveness plot with the AC turbulence condition and $Re_C$= 1,000,000 can be seen in Figure 67. For these data, the first slot was maintained at $M_{SS1}$ = 0.5, while the second and third slot were set to a blowing ratio of $M_{SS2}$ = 0.15 and $M_{SS3}$ = 0.15, respectively. Again, there is good uniformity upstream and downstream of the third slot and the film cooling layer appears to be swept away. Compared to Figure 65 the preservation of the cooling film layer downstream is slightly diminished which is expected due to the lower blowing ratio from SS3.

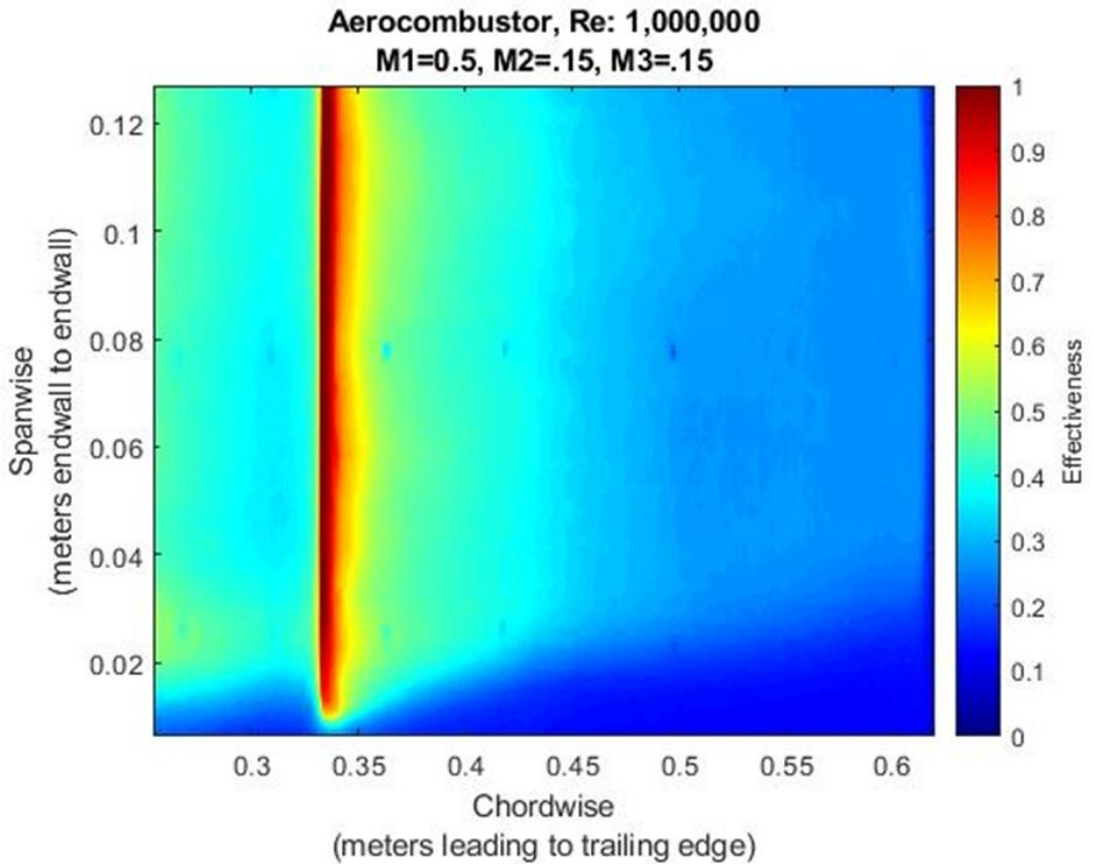


Figure 67. Contour plot of suction surface film cooling, $Re_C$ = 1,000,000, AC, $M_{SS1}$ = 0.5, $M_{SS2}$ = 0.15, $M_{SS3}$ = 0.15.

Similar to Figure 66, the centerline plots in Figure 68 show excellent correlation between the infrared camera and thermocouple measurements. As before, the calibration of IR camera data using thermocouple data should be kept in mind interpreting the full surface plots.

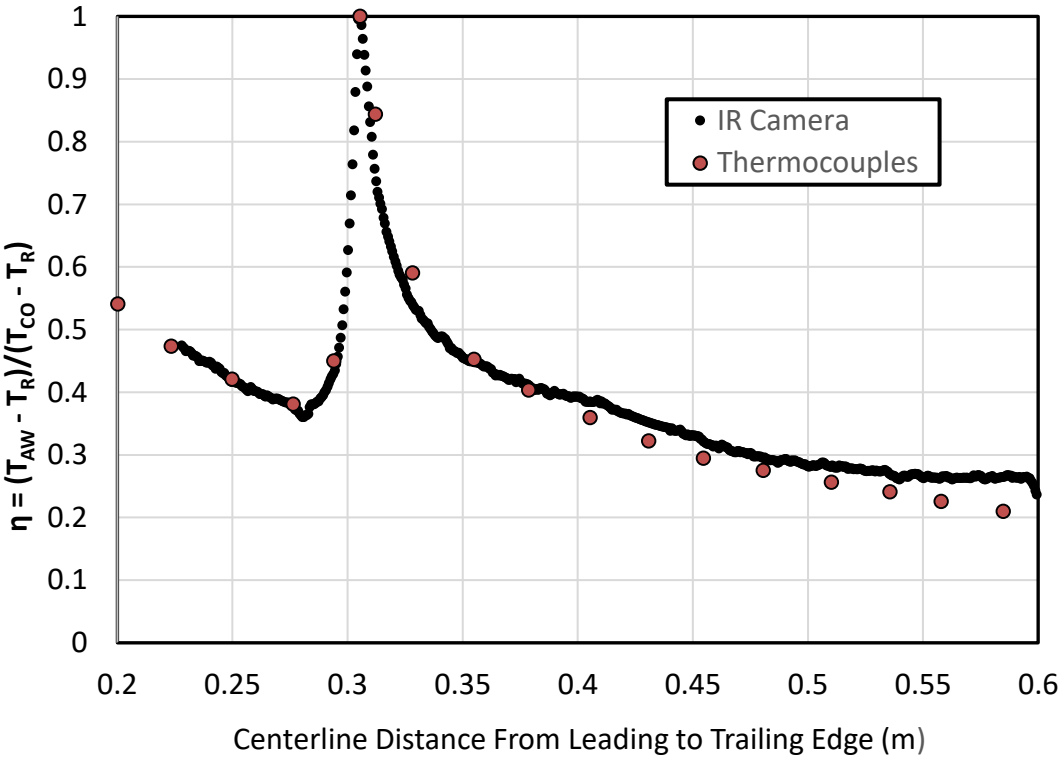


Figure 68. Centerline plot of IR camera temperature distribution compared to thermocouple measurements, suction surface film cooling, $Re_C$ = 1,000,000, AC, $M_{SS1}$ = 0.5, $M_{SS2}$ = 0.15, $M_{SS3}$ = 0.15.

A film cooling contour plot at the AC turbulence condition with $Re_C$ = 1,000,000 with blowing ratios of $M_{SS1}$ = 1.0, $M_{SS2}$ = 0.30 and $M_{SS3}$ = 0.30 is presented in Figure 69. Compared to Figure 65 and Figure 67, the flow upstream of the third slot is not as uniform showing slight effectiveness troughs that likely result from internal coolant flow maneuvering around pedestals inside the second flow plenum. The spanwise effectiveness is reasonably uniform downstream of the third coolant slot and the film cooling layer appears to be swept away as seen in the previous full surface plots. Compared to Figure 65 the preservation of the cooling film layer downstream is slightly more preserved which is expected due to the lower blowing ratio from SS3.

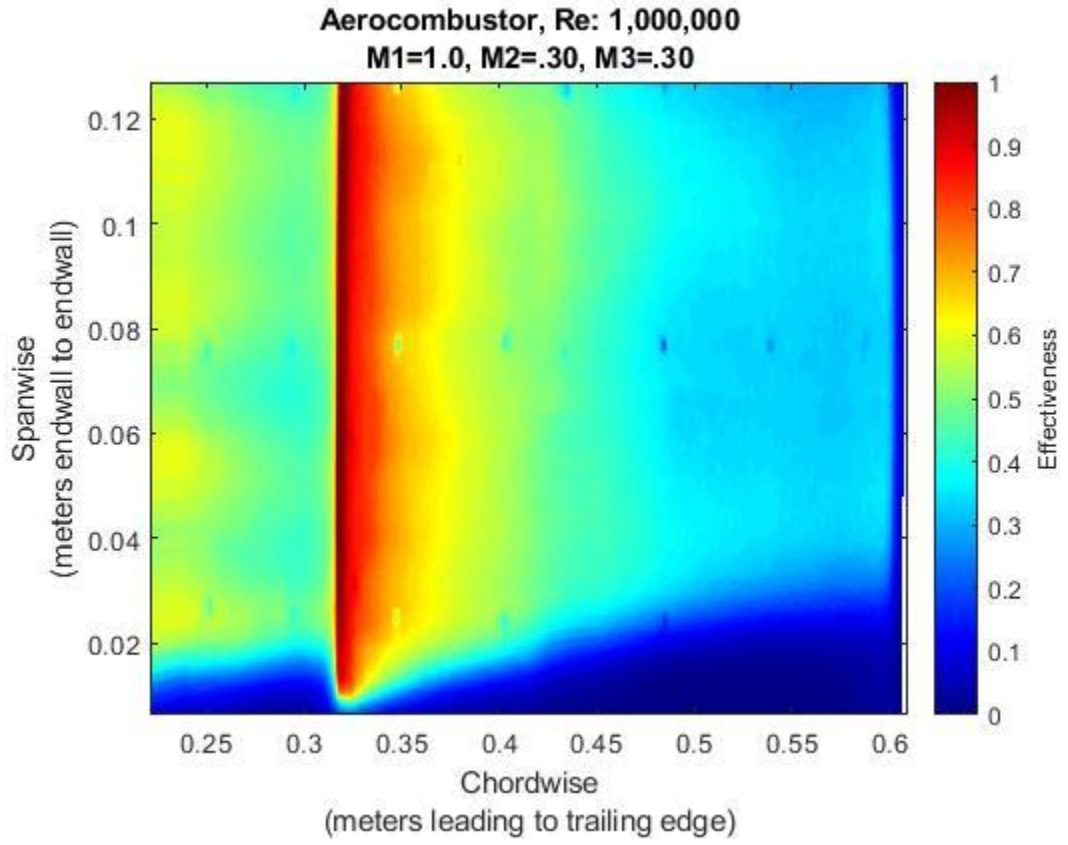


Figure 69. Contour plot of suction surface film cooling, $Re_C$ = 1,000,000, AC, $M_{SS1}$ = 0.5, $M_{SS2}$ = 0.30, $M_{SS3}$ = 0.30.

The plot correlating the centerline temperature to the contour plot in Figure 69 is displayed in Figure 70. The IR data is consistent with the thermocouple data from which it was calibrated.

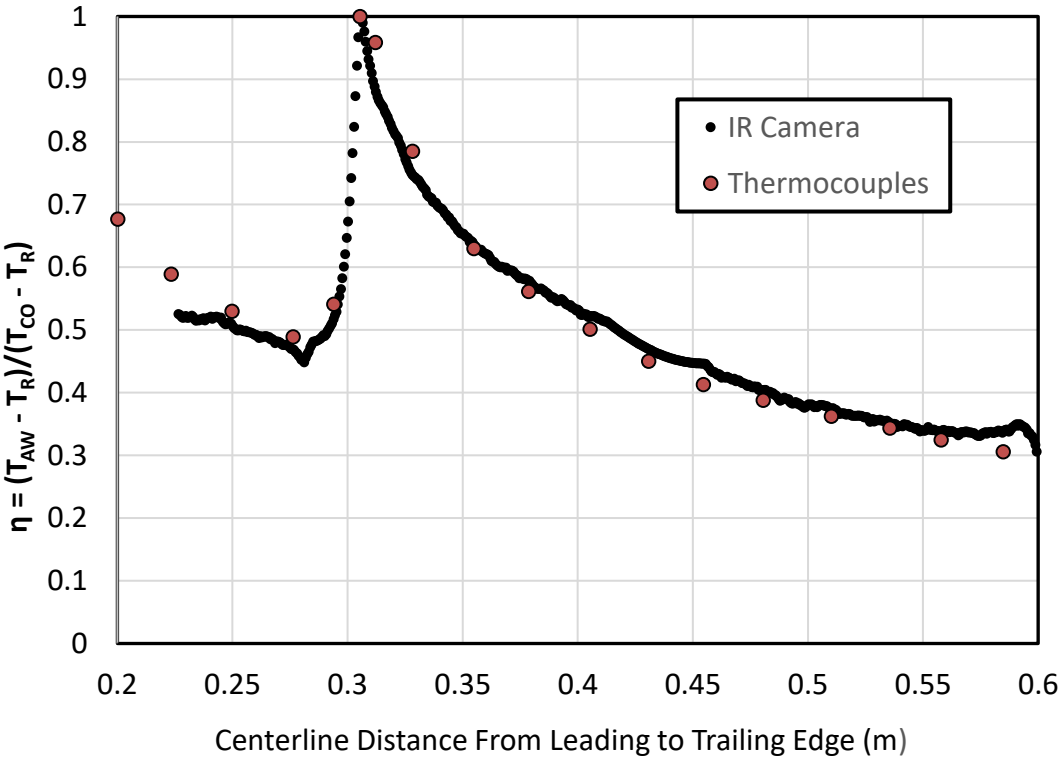


Figure 70. Centerline plot of IR camera temperature distribution compared to thermocouple measurements, suction surface film cooling, $Re_C$ = 1,000,000, AC, $M_{SS1}$ = 1.0, $M_{SS2}$ = 0.30, $M_{SS3}$ = 0.30.

Figure 71 displays the full surface plot at chord Reynolds number of 1,000,000 with blowing ratios of $M_{SS1}$ = 1.0, $M_{SS2}$ = 0.15 and $M_{SS3}$ = 0.15 at the AC turbulence condition. The flow upstream of the third slot shows some spanwise variation having slightly more pronounced effectiveness troughs upstream of the third coolant slot similar to what is shown in Figure 69. Similar to the other blowing ratio tested at the aerocombustor turbulence condition, the film cooling layer appears to be swept away due to the passage vortex downstream of the third coolant slot. The coolant film coverage appears to decay evenly spanwise and progressively streamwise after the final near lost region.

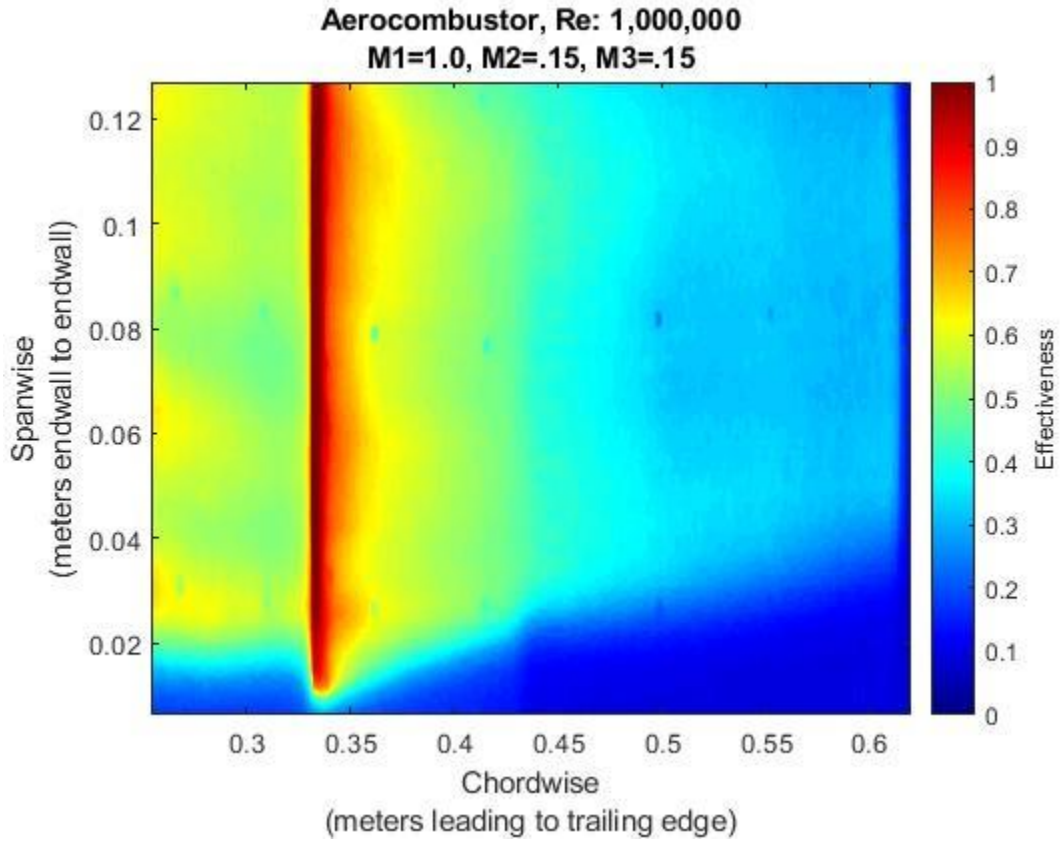


Figure 71. Contour plot of suction surface film cooling, $Re_C$ = 1,000,000, AC, $M_{SS1}$ = 1.0, $M_{SS2}$ = 0.15, $M_{SS3}$ = 0.15.

Correlation between the centerline temperatures from the thermocouples and the IR camera data for the full surface plot in Figure 71 is displayed in Figure 72. Upstream of the third coolant slot and in the near slot region, the IR data is not as closely fit to the thermocouple data. This variance is believed to exist due to the close proximity of the thermocouples to the effectiveness troughs that exist prior to and after the third coolant slot. Overall, the correlations suggest the full surface plot seen is Figure 71 is an accurate representation of the full surface effectiveness at the designated parameters.

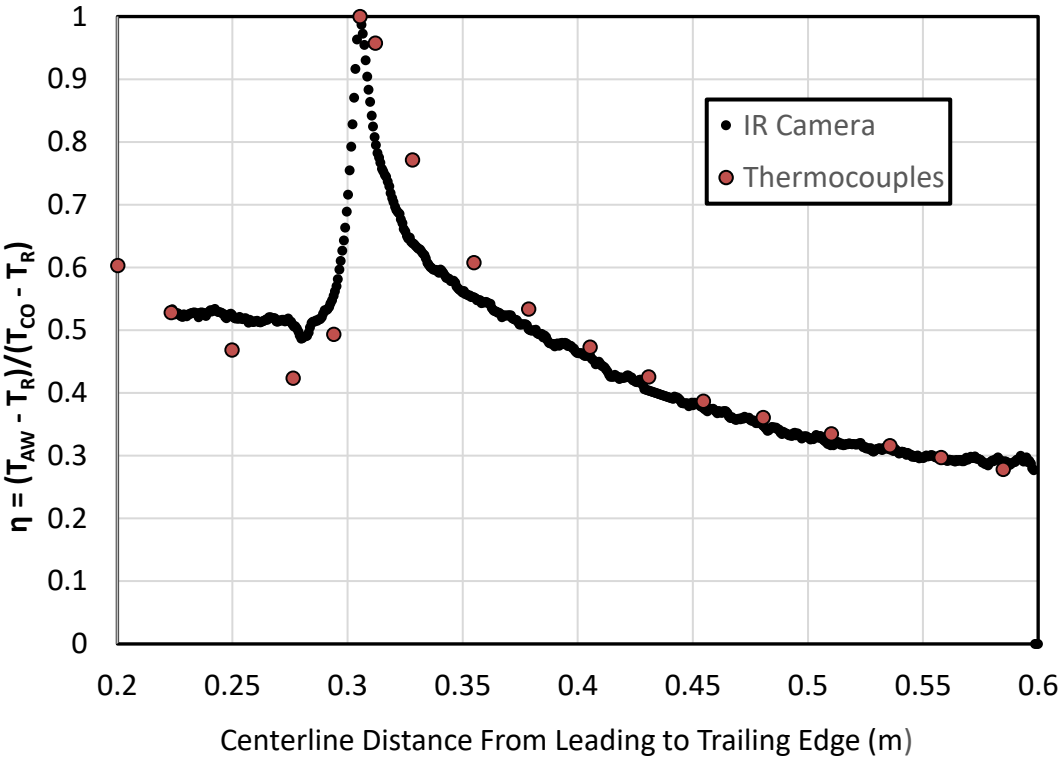


Figure 72. Centerline plot of IR camera temperature distribution compared to thermocouple measurements, suction surface film cooling, $Re_C$ = 1,000,000, AC, $M_{SS1}$ = 1.0, $M_{SS2}$ = 0.15, $M_{SS3}$ = 0.15.

The full surface film cooling effectiveness at $Re_C$= 1,000,000 with the small grid far turbulence condition having blowing ratios for the upstream, middle and downstream slot of $M_{SS1}$ = 0.5, $M_{SS2}$ = 0.3 and $M_{SS3}$ = 0.3, respectively, is presented in Figure 73. The spanwise flow is consistent upstream and downstream of the third slot, with the exception of the near slot region, which shows some uneven flow that is consistent with inter-pedestal passageways. As seen in the aerocombustor IR data plots, the bottom (near endwall) of the figure indicates the film cooling is progressively being swept away which is likely due to the passage vortex.

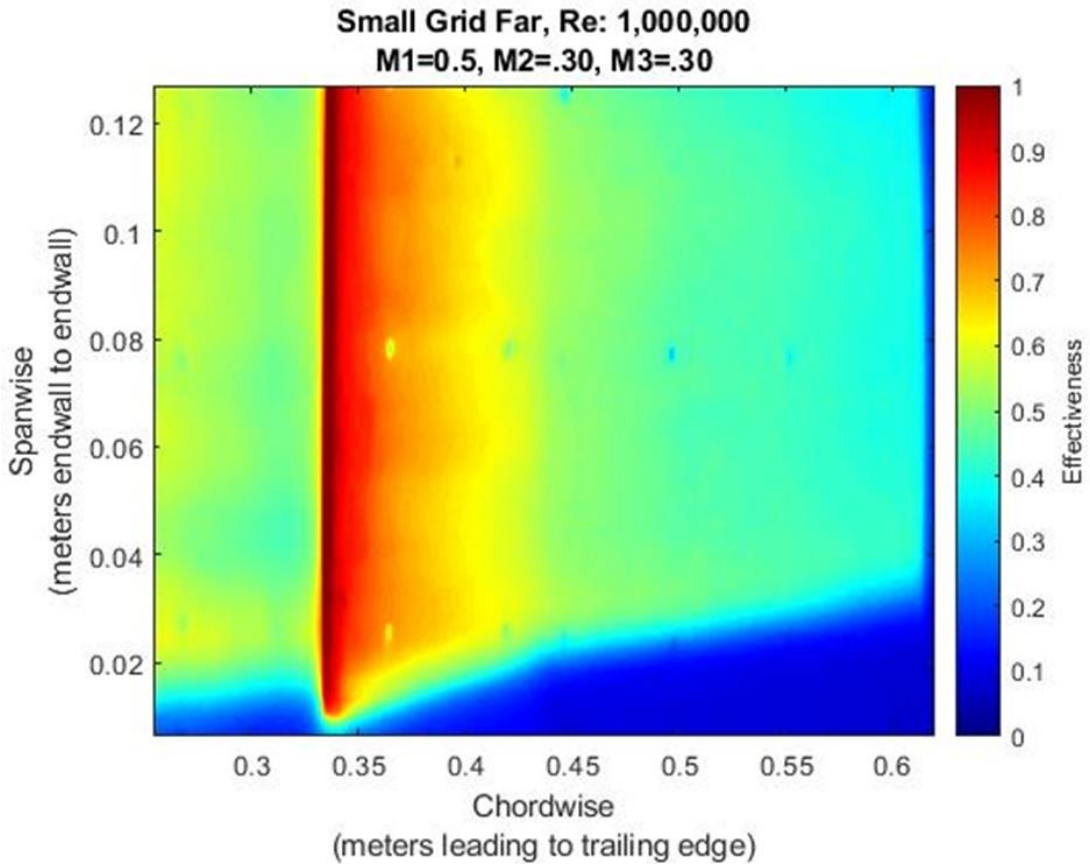


Figure 73. Contour plot of suction surface film cooling, $Re_C$ = 1,000,000, AC, $M_{SS1}$ = 0.5, $M_{SS2}$ = 0.3, $M_{SS3}$ = 0.3.

The correlation between the thermocouple centerline temperature and contour plot in Figure 73 is displayed in Figure 76. The IR data and thermocouple data diplay consistent trends. The dips in the IR readings are congruent with the placement of the gold flake dot that where painted for referencing position.

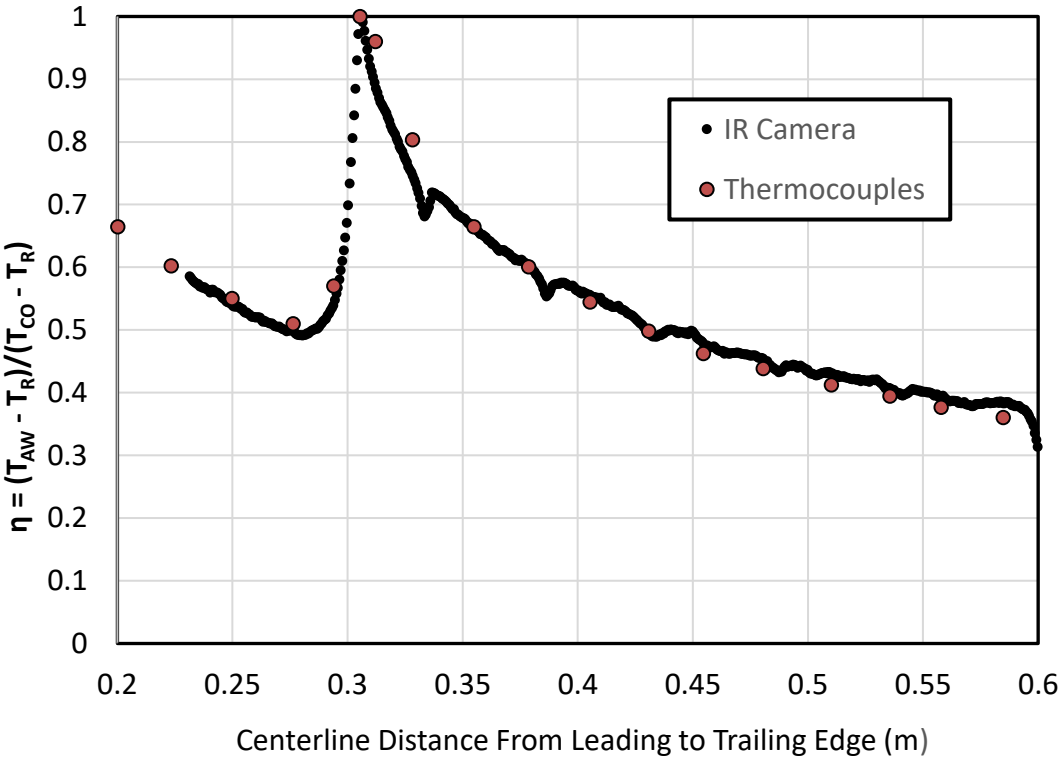


Figure 74. Centerline plot of IR camera temperature distribution compared to thermocouple measurements, suction surface film cooling, $Re_C$ = 1,000,000, AC, $M_{SS1}$ = 1.0 , $M_{SS2}$ = 0.30, $M_{SS3}$ = 0.30

A contour plot with the blowing ratios of 0.5, 0.15 and 0.15 for the first second and third slot, respectively, is displayed in Figure 75. These data were recorded at the SGF turbulence condition with nominal chord Reynolds number 1,000,000. The uniformity before and aft of the third coolant slot is fairly consistent, though there is some signs of ridges and troughs beginning to form from coolant air passing through the inner geometries of the second and third plenums. Near the endwall, the film coverage is swept inward progressively moving towards the trailing edge, which is likely due to the passage vortex effect. The film cooling effectiveness decays to low levels much closer to the coolant slot compared to other testing schemes at this turbulence condition, which is

consistent with the centerline averaged thermocouple effectiveness plots at these conditions.

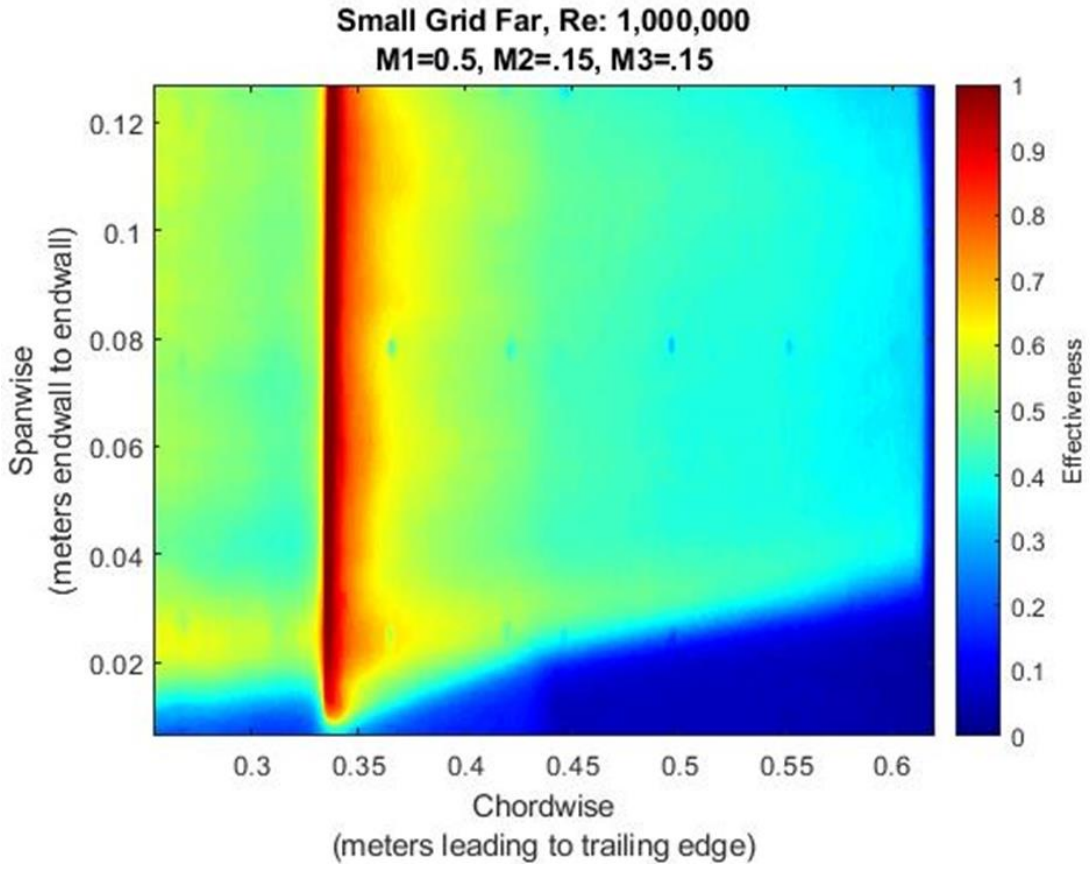


Figure 75. Contour plot of suction surface film cooling, $Re_C$ = 1,000,000, SGF, $M_{SS1}$ = 0.5, $M_{SS2}$ = 0.15, $M_{SS3}$ = 0.15.

Figure 76 displays the relationship between the thermocouple and IR camera centerline temperatures with reference to the full surface plot in Figure 75. These data show trends that are consistent; however, the IR camera shows slightly elevated effectiveness values moving towards to the trailing edge.

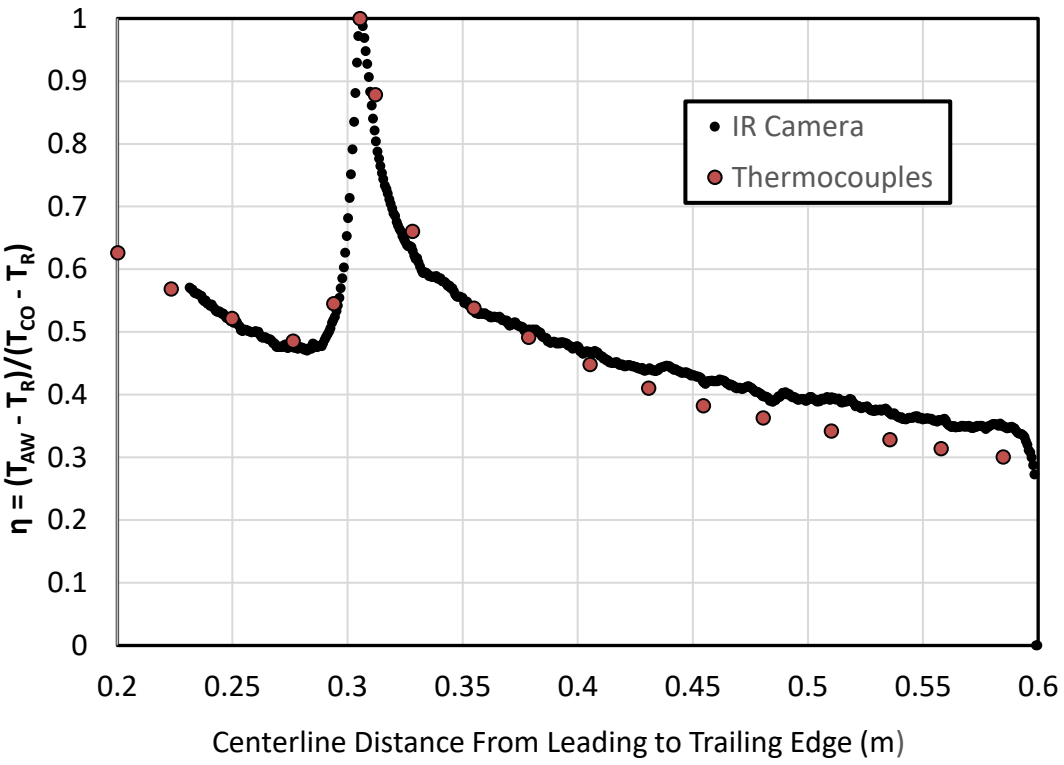


Figure 76. Centerline plot of IR camera temperature distribution compared to thermocouple measurements, suction surface film cooling, $Re_C$ = 1,000,000, SGF, $M_{SS1}$ = 0.5, $M_{SS2}$ = 0.15, $M_{SS3}$ = 0.15.

The full surface plot for the SGF turbulence condition at $Re_C$ = 1,000,000 with blowing ratios of $M_{SS1}$ = 1.0, $M_{SS2}$ = 0.30 and $M_{SS3}$ = 0.30 may be viewed in Figure 77. Ridges of higher effectiveness and valleys of lower effective before and aft of the third coolant slot are pronounced when compared to Figure 73 and Figure 75. This effect is assumed to be due to coolant air traversing the pedestal geometry within the coolant plenums at the high blowing ratio for SS1. This elevated spanwise variation at higher blowing ratios is consistent with the thermocouple centerline effectiveness plots presented earlier in this body of research. The influence of the higher blowing ratio from the first coolant slot is likely enabling the higher levels of film cooling effectiveness that

extend further down the surface in the streamwise direction. The coolant layer appears to be progressively swept away near the endwall as seen in the previous full surface plots. Again, this effect is likely due to the passage vortex.

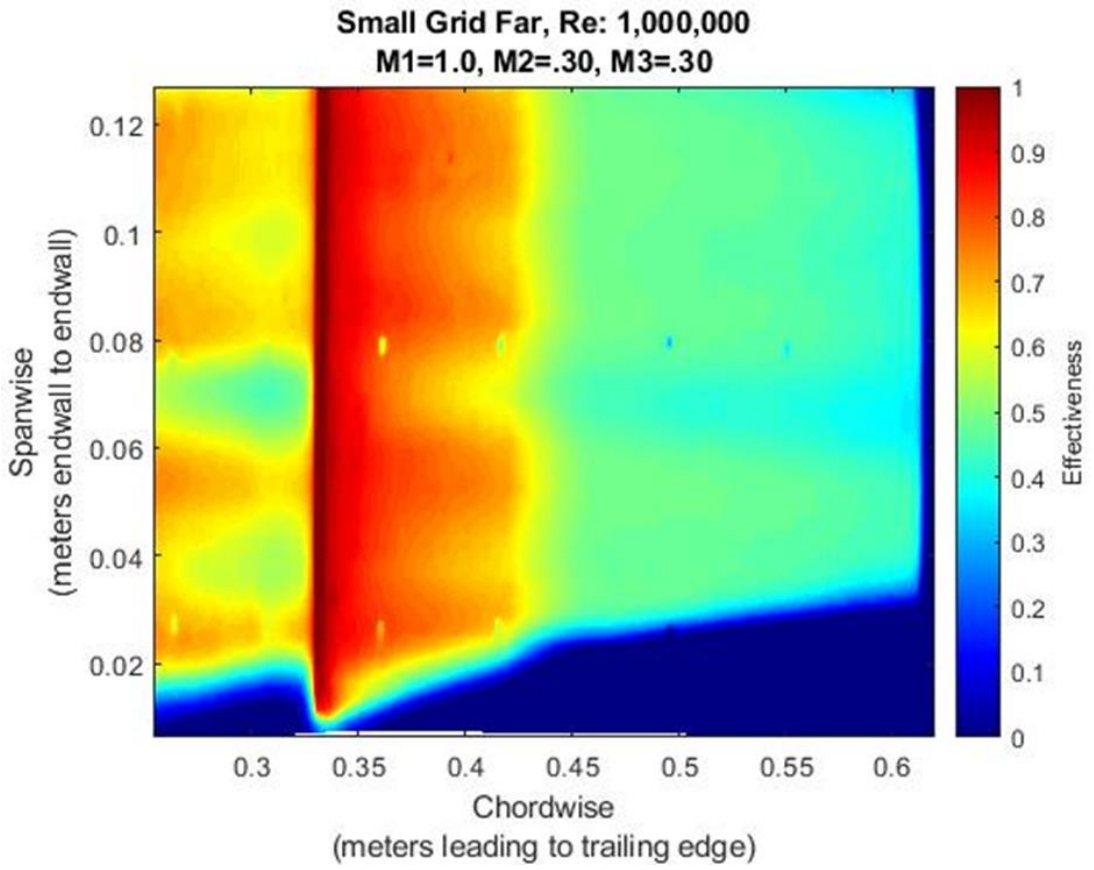


Figure 77. Contour plot of suction surface film cooling, $Re_C$ = 1,000,000, SGF, $M_{SS1}$ = 1.0, $M_{SS2}$ = 0.30, $M_{SS3}$ = 0.30.

Figure 78 displays the correlation between the IR camera centerline data and the thermocouple centerline data for the contour plot in Figure 77. The contour plot centerline fit is generally good; however, the spanwise variation produces bumps and dips in the IR camera results. The slight departures align with the fingers and valleys seen in the full surface plot.

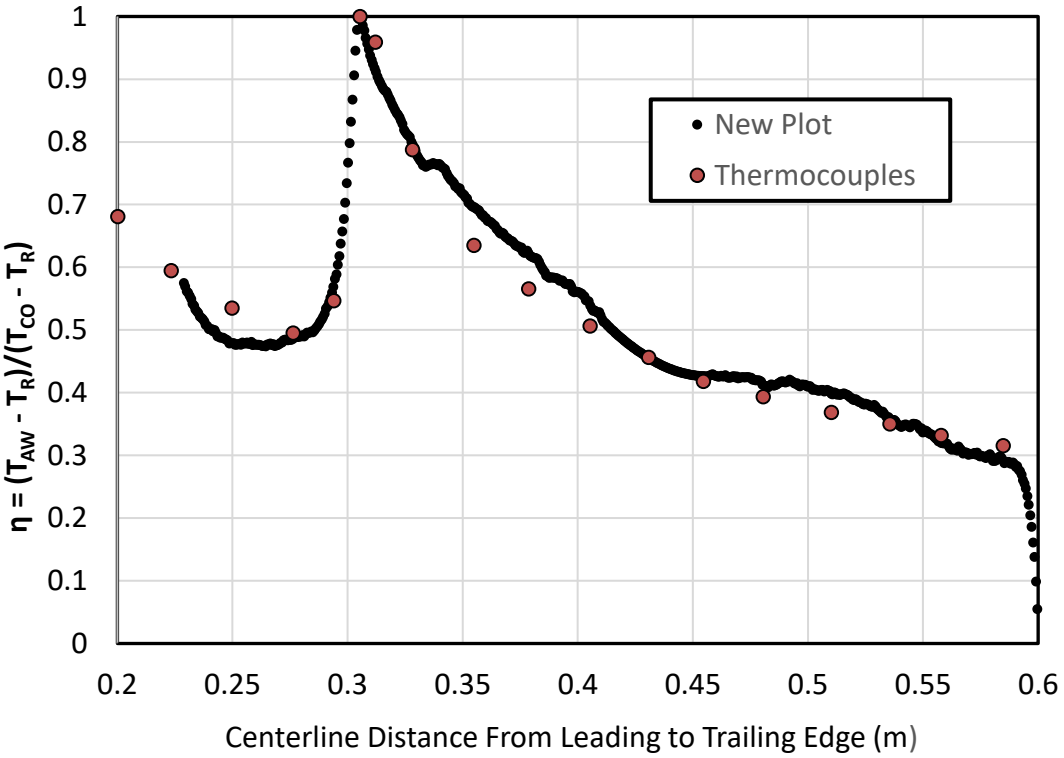


Figure 78. Centerline plot of IR camera temperature distribution compared to thermocouple measurements, suction surface film cooling, $Re_C$ = 1,000,000, SGF, $M_{SS1}$ = 1.0, $M_{SS2}$ = 0.30, $M_{SS3}$ = 0.30.

Figure 79 displays the contour plot at $Re_C$= 1,000,000 with blowing ratios of $M_{SS1}$ = 1.0, $M_{SS2}$ = 0.15 and $M_{SS3}$ = 0.15 at the SGF turbulence condition. The plot is slightly distorted near the Top left corner due to a slightly misaligned lower IR camera angle. Despite this distortion, the plot lends a good visual depiction of the spanwise effectiveness trends over the surface of the vane at the aforementioned conditions. The flow pattern matches Figure 77 closely; however, there is more robust film coverage upstream of the third slot. This is counter intuitive as the blowing ratio from the second coolant slot is at the lower setting (0.15). Consistent with other blowing ratios tested at the small grid far turbulence condition, the film cooling layer appears to be swept away

due to the passage vortex downstream of the third coolant slot. Otherwise, the coolant film coverage spread evenly in the spanwise direction after the final near lost region.

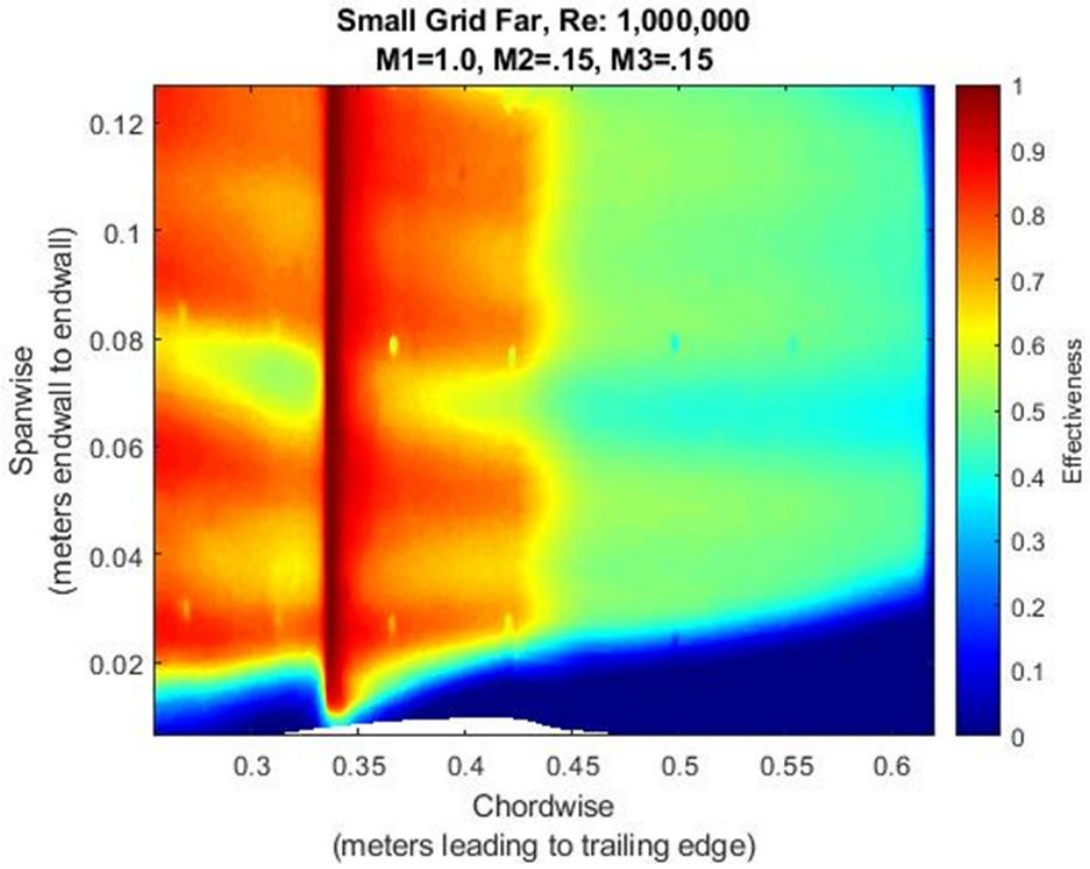


Figure 79. Contour plot of suction surface film cooling, $Re_C$ = 1,000,000, SGF, $M_{SS1}$ = 1.0, $M_{SS2}$ = 0.15, $M_{SS3}$ = 0.15.

Figure 80 displays the correlation between the IR camera centerline data and the thermocouple centerline data for the contour plot in Figure 79. The bumps and dips in the IR camera results are slightly more pronounced at these blowing ratios than those seen in Figure 78. Again, the slight departures align with the fingers and valleys seen in the full surface plot. Here, the thermocouple data also show a dip between 0.40 meters and 0.45 meters.

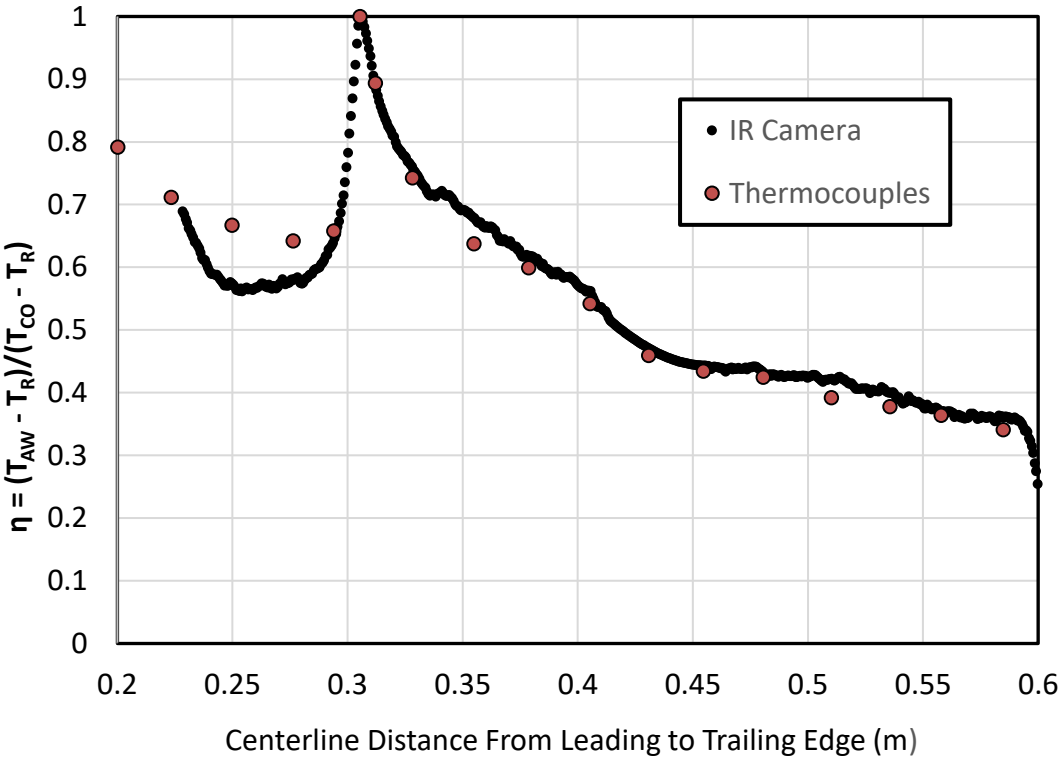


Figure 80. Centerline plot of IR camera temperature distribution compared to thermocouple measurements, suction surface film cooling, $Re_C$ = 1,000,000, SGF, $M_{SS1}$ = 0.5, $M_{SS2}$ = 0.15, $M_{SS3}$ = 0.15.

The contour plots for the LG and LT turbulence condition can be viewed in Appendix F. The sweeping effect of the passage vortex is evident as the film cooling layer is being carried away progressively in the region of the suction surface near the endwall is present in every plot. The inner plenum geometry appears to have a much greater impact on LG full surface plots. These contour plots show much more pronounced spanwise variation compared to the other turbulence conditions. The LT turbulence contour plots also show an elevation spanwise variation, but not to the degree of the LG surface plots. For both turbulence conditions, the spanwise variation increases with increased blowing ratios (coolant air mass addition).

# CHAPTER V

# CONCLUSIONS

This current study has produced a comprehensive database of film cooling effectiveness distributions for a pressure side vane with one coolant slot and a suction side vane with three coolant slots. The film cooling slot slot is located at 62% arc (-0.3 m) on the pressure surface of a vane while the suction side slots are placed at the locations corresponding to the vane cooling model. The interior of the slot plenums emulates a double walled cooling approach that includes high solidity pedestal arrays. Additionally, the first suction side and pressure side plenums include impingement jets incorporated into the final pedestal row. The recorded data consists film cooling effectiveness for individual and integrated blowing ratios over a range of three exit chord Reynolds numbers (500,000, 1,000,000, and 2,000,000) at five elevated turbulence conditions for the pressure side (Tu = 0.7%, 3.5%, 7.9%, 12.7%, and 17.4%) and four elevated turbulence conditions for the suction side (Tu = 0.7%, 3.5%, 7.9%, and 12.7%).

## Pressure Side Vane

Cooling effectiveness generally fell off precipitously downstream of the film cooling slots. The internal geometry of the slot, meant to emulate the internal cooling scheme, generated vorticity, inflow turbulence, and a velocity distribution that is likely responsible for rapid drop film cooling effectiveness. The high solidity pedestals in the

pressure side plenum have impingement jets imbedded in the aft of the last row, which may have engendered a robust vortex system. The synergy of the horseshoe vortex system created by the upstream pin fins merged with the wall jet from the impingement holes may have produced this condition.

The downstream rapid decay in the near slot region (X/S <30) is generally consistent with the exception of the lower turbulence conditions for exit chord Reynolds numbers of 500,000 and 1,000,000. These exceptions are thought to be caused by laminar or transitional flow in the near slot region.

The small grid far (SGF) and large grid (LG) conditions mostly exhibited minimal loss in film cooling effectiveness in contrast to the low turbulence conditions. Conversely, the aerocombustor turbulence level (AC) and the high turbulence aerocombustor (HT) conditions showed a significant drop in film cooling effectiveness levels, which decreased progressively along the length of the surface. The dissipation due to turbulence was most abrupt for the lowest blowing ratio (M=0.4) and tended to move further downstream with rising blowing ratios.

The higher blowing ratios resulted in film cooling effectiveness levels along the surface that were above those at lower blowing ratios. However, the lower blowing ratios proved to be substantially more effective on a per unit mass of coolant basis.

The suction side data are thought to offer a valuable set of slot film cooling data for comprehending the intricacies of inflow fluid dynamics caused by pertinent internal cooling geometries on downstream film cooling levels.

## Suction Side Vane

Blowing ratio was observed to have significant impact on the adiabatic film cooling effectiveness throughout the breadth of blowing ratios examined. The film cooling effectiveness rose nearly proportional to blowing ratio when cooling air was limited to one slot entirely. Raising the blowing ratio from 0.15 to 0.30 for both slot SS2 and SS3, with the aerocombustor (AC) turbulence condition increased the film cooling effectiveness by approximately 86%. For the small grid far (SGF) turbulence condition, the same change in blowing ratio boosted the effectiveness by about a 75% in the downstream region. These outcomes are likely due to the additive nature of the film cooling of these conditions.

The turbulence intensity (turbulence condition) effected the film cooling coverage dissipation the most. This was most notable near the first slot, which is subject to the highest local turbulence levels. The effect of the turbulence condition on film cooling coverage was diminished further down the turbine surface, having the least influence on film cooling after the third coolant slot. Film cooling coverage was impacted less at higher velocities.

The application of superposition using individual slot film cooling distributions to assess overall film cooling distribution was somewhat successful. Unfortunately, it was apparent that coolant air added from multiple slots altered the fluid dynamics, and the superposition correlation between single slot film cooling and multi-slot integrated film cooling became inconsistent and was no longer applicable.

Plotting the full surface film cooling distribution from IR Camera data added context and depth to the understanding flow patterns. The distributions showed the sweeping effect of the passage vortex, which carried away film cooling coverage progressively along the endwall. For all turbulence conditions tested, the spanwise variation increases with increased blowing ratios (coolant air mass addition), particularly from the upstream slot (SS1). In addition, the consistency between slot film cooling distributions was made evident.

The aerodynamic losses were not emphasized during this study, though it is assumed that the exiting coolant flow from coolant slots into high-speed mainstream flow regions of the suction surface would produce aerodynamic losses.

The suction side film cooling data, including the full surface plots, are useful to not only understanding the flow patterns associated with the present cooling configurations, but also to validate predictive models and computational methods used in industrial cooling schemes that include similar internal cooling geometries.

# APPENDICES

Appendix A

**Cascade Dimensions**

Note: All cascade dimensions in this appendix are in inches. The cascade and the following drawings were constructed by Justin Varty [41].

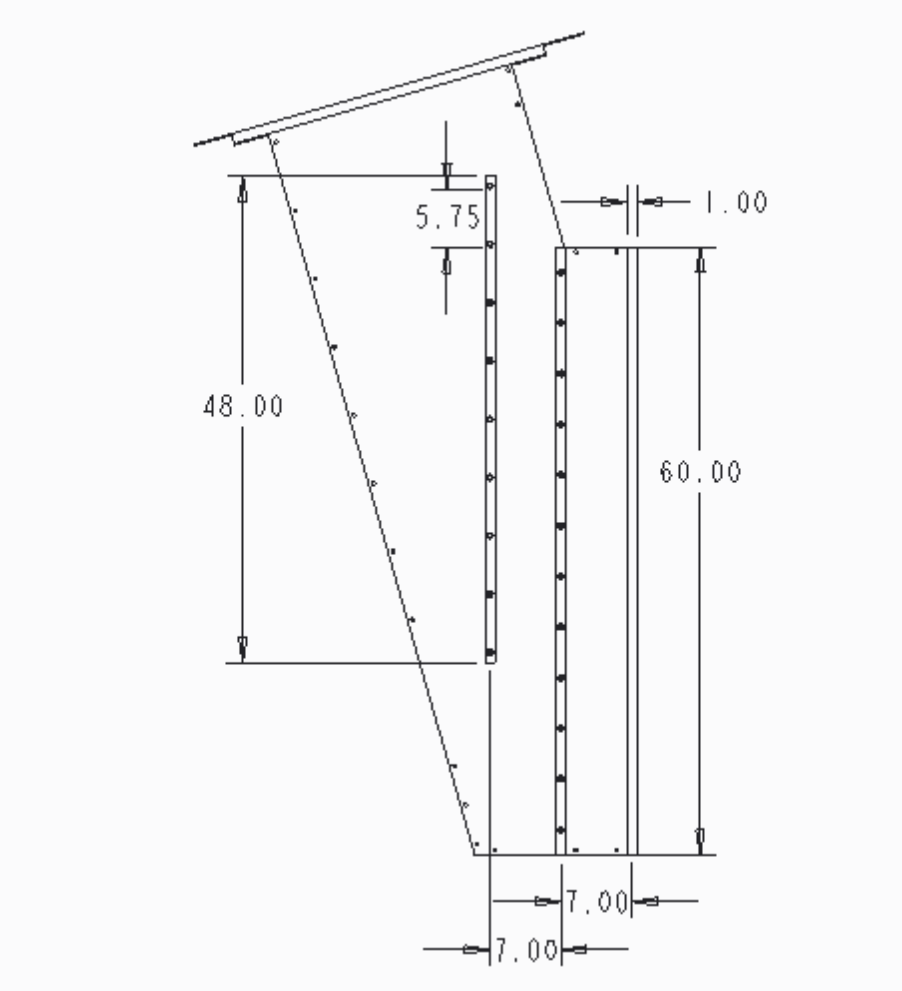


Figure 81. Cascade far endwall dimensions [41] .

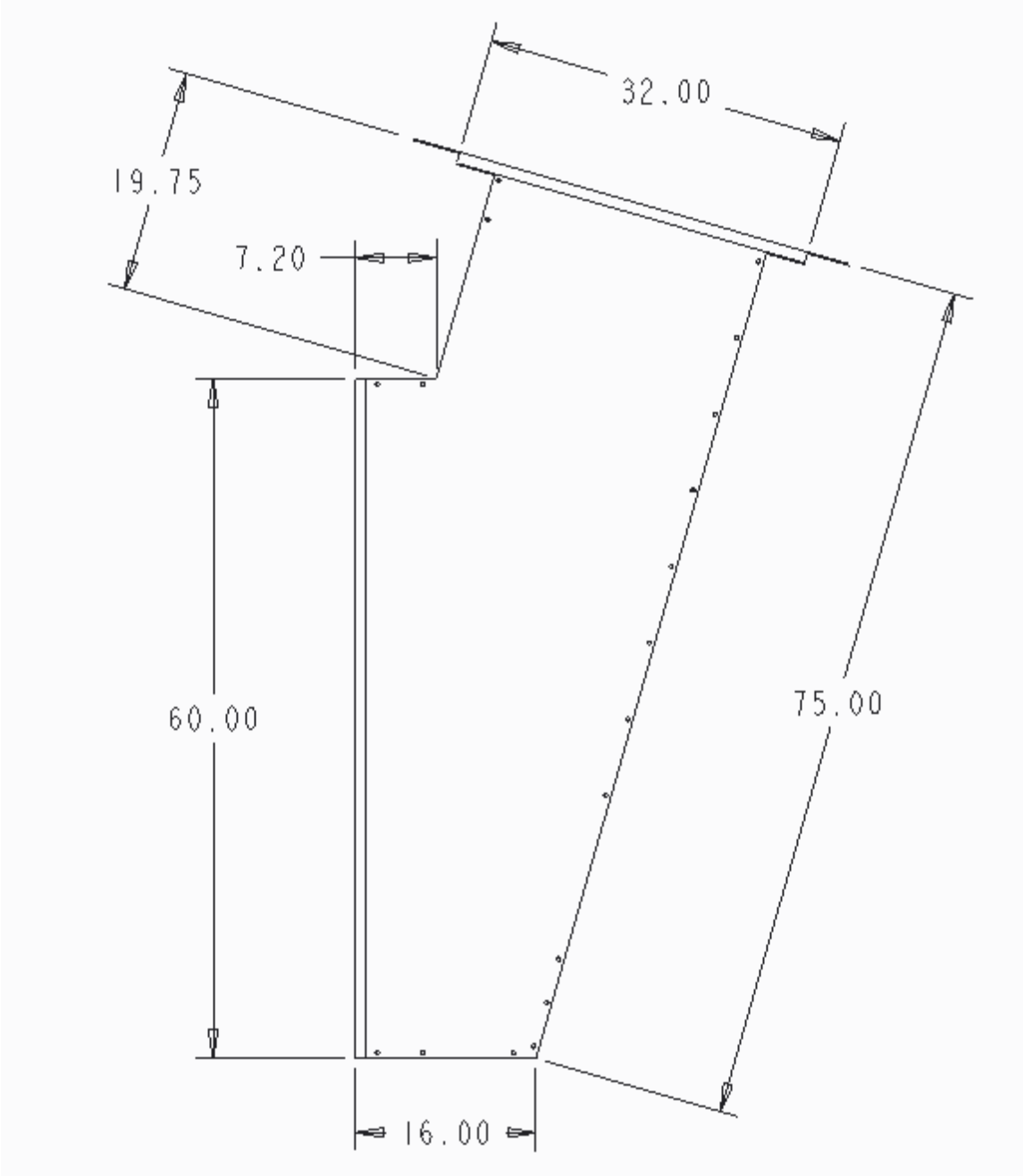


Figure 82. Cascade near endwall dimensions [41] .

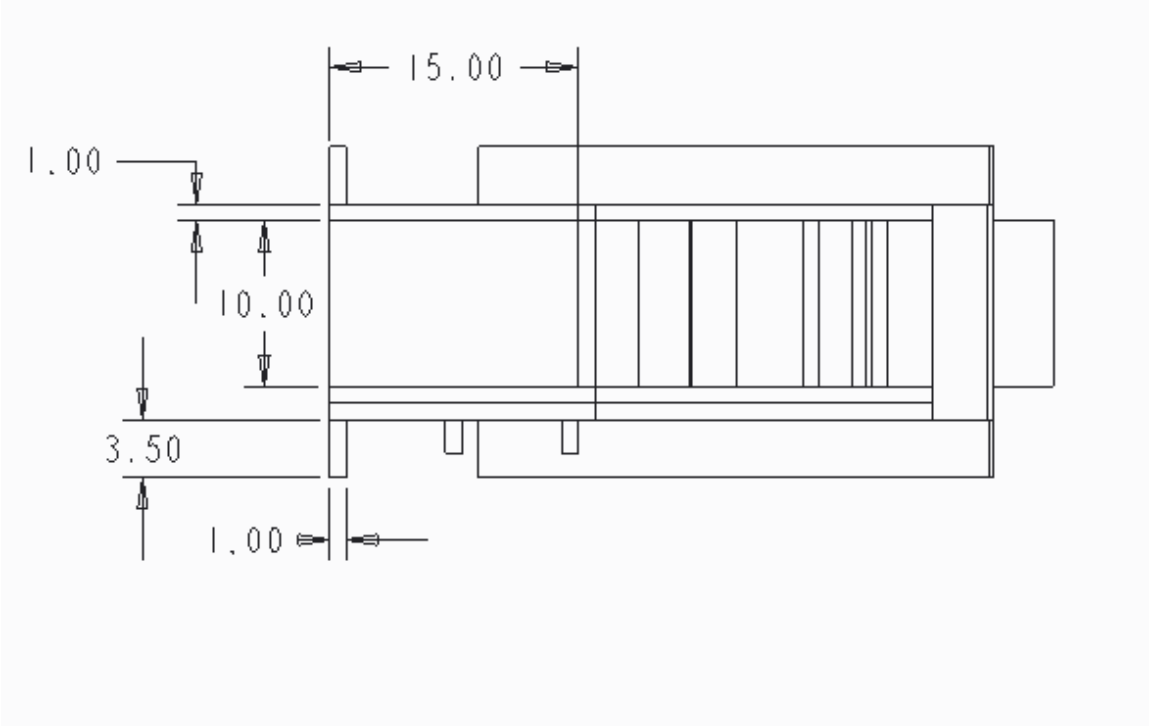


Figure 83. Cascade bottom dimensions [41] .

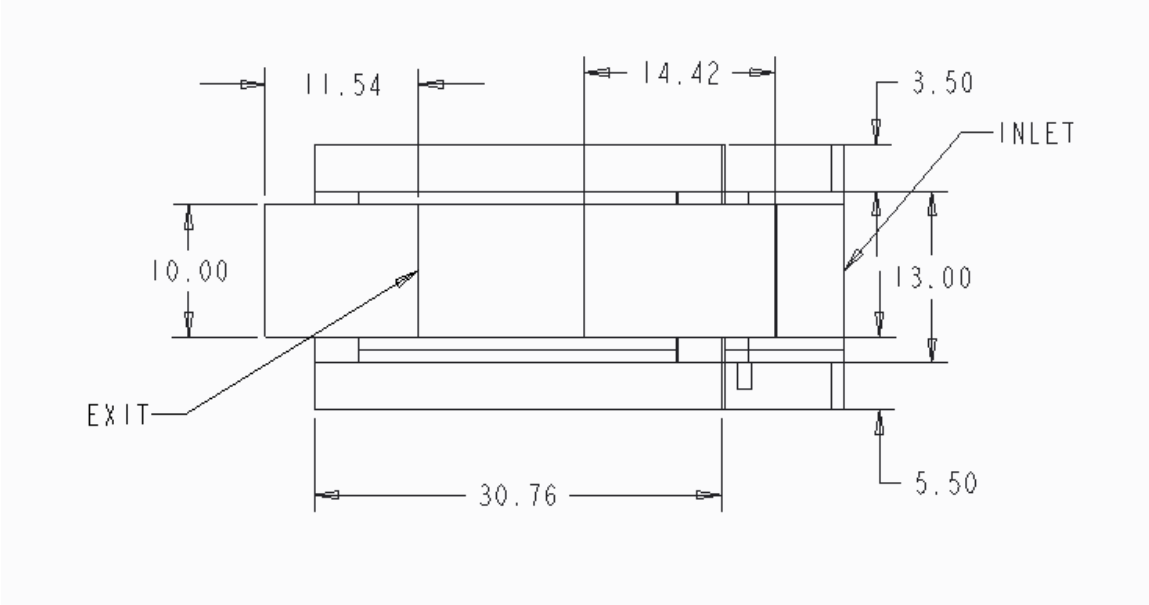


Figure 84. Cascade top dimensions [41] .

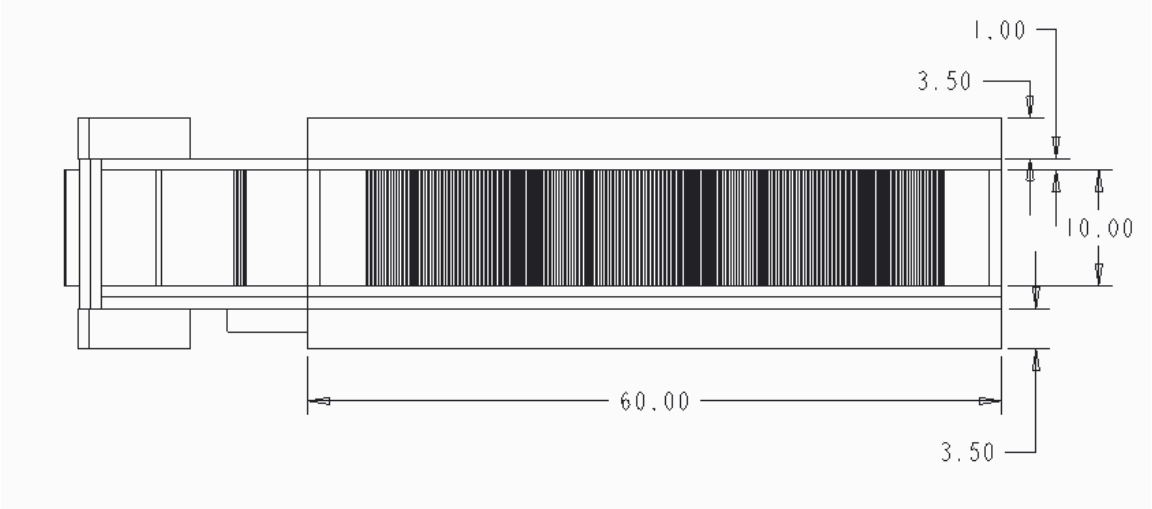


Figure 85. Cascade front dimensions [41] .

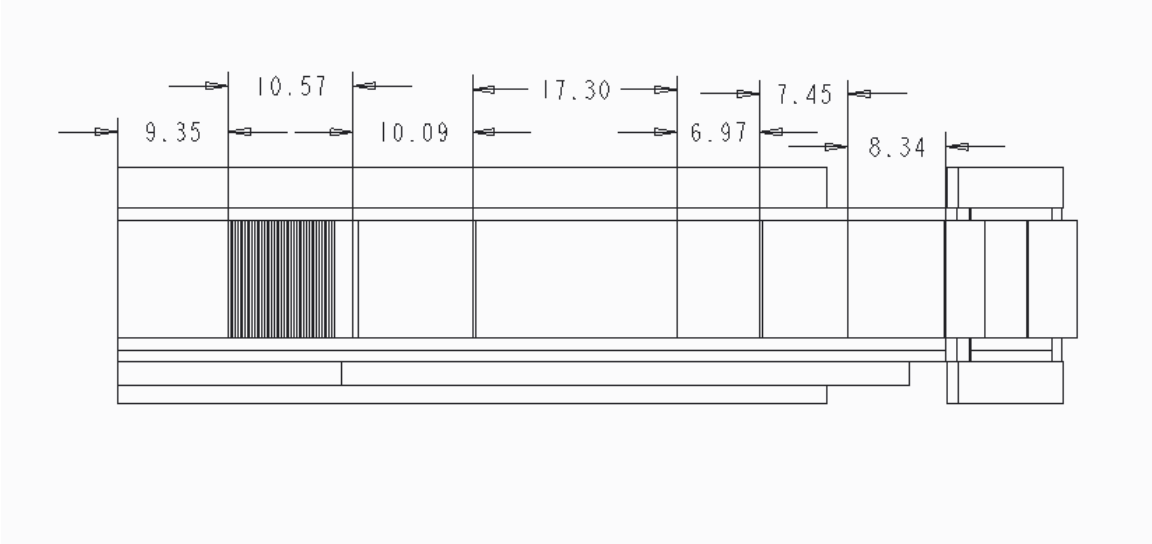


Figure 86. Cascade back dimensions [41] .

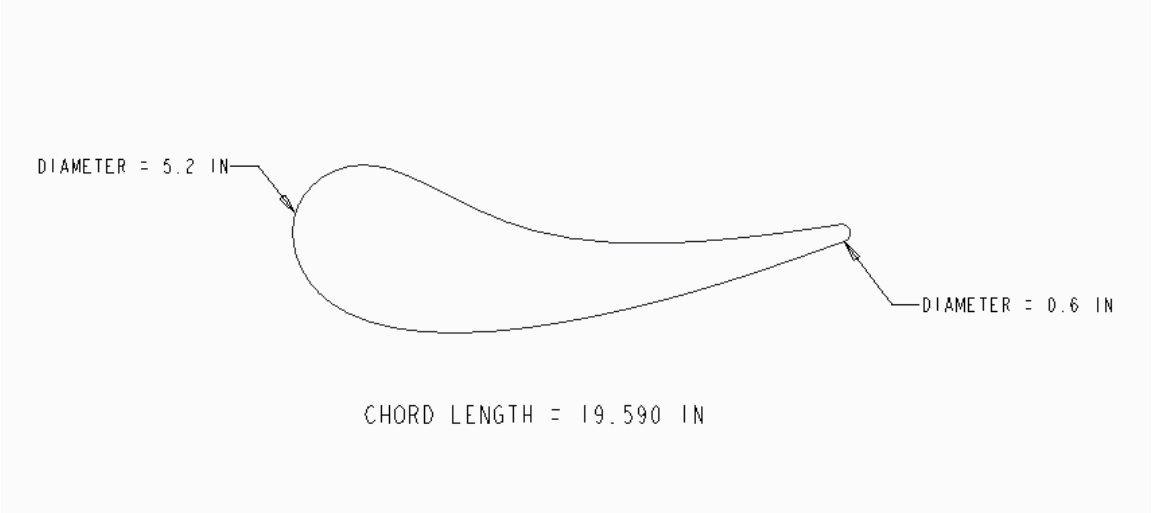


Figure 87. Vane dimensions [41] .

Appendix B

## Vane Thermocouple Layouts

Pressure Side Layout

Table 4. Thermocouple locations for Pressure Side Vane.

| Row | Indicated Channel(s) for Quick Basic | Label Number(s) | Distance from Trailing Edge (in) | Distance from Stagnation Point (in) | Distance from Trailing Edge (m) | Distance from Stagnation Point (m) |
|---|---|---|---|---|---|---|
| 9 | 27-29 | 27-29 | 0.00 | -18.70 | 0.00 | -0.47 |
| 8 | 24-26 | 24-26 | 1.23 | -17.47 | 0.03 | -0.44 |
| 7 | 21-23 | 21-23 | 2.17 | -16.53 | 0.06 | -0.42 |
| 6 | 19-20 | 19-20 | 3.15 | -15.54 | 0.08 | -0.39 |
| 5 | 15-17 | 15-17 | 4.19 | -14.51 | 0.11 | -0.37 |
| 4 | 12-14 | 12-14 | 5.15 | -13.55 | 0.13 | -0.34 |
| 3 | 9-11 | 9-11 | 6.17 | -12.52 | 0.16 | -0.32 |
| 2 | 6-8 | 6-8 | 6.79 | -11.90 | 0.17 | -0.30 |
| 1 | 1-5 | 1-5 | 7.31 | -11.38 | 0.19 | -0.29 |
| 24 | 44 | 44 | 13.41 | -5.29 | 0.34 | -0.13 |
| 23 | 43 | 43 | 15.44 | -3.26 | 0.39 | -0.08 |
| 22 | 42 | 42 | 17.50 | -1.20 | 0.44 | -0.03 |
| 21 | 41 | 41 | 19.44 | 0.74 | 0.49 | 0.02 |
| 20 | 40 | 40 | 21.50 | 2.81 | 0.55 | 0.07 |
| 19 | 39 | 39 | 23.41 | 4.71 | 0.59 | 0.12 |
| 18 | 38 | 38 | 25.44 | 6.74 | 0.65 | 0.17 |
| 17 | 37 | 37 | 27.44 | 8.74 | 0.70 | 0.22 |
| 16 | 36 | 36 | 29.50 | 10.81 | 0.75 | 0.27 |
| 15 | 35 | 35 | 31.41 | 12.71 | 0.80 | 0.32 |
| 14 | 34 | 34 | 33.41 | 14.71 | 0.85 | 0.37 |
| 13 | 33 | 33 | 35.41 | 16.71 | 0.90 | 0.42 |
| 12 | 32 | 32 | 37.47 | 18.77 | 0.95 | 0.48 |
| 11 | 31 | 31 | 39.44 | 20.74 | 1.00 | 0.53 |
| 10 | 30 | 30 | 41.50 | 22.81 | 1.05 | 0.58 |

Suction Side Layout

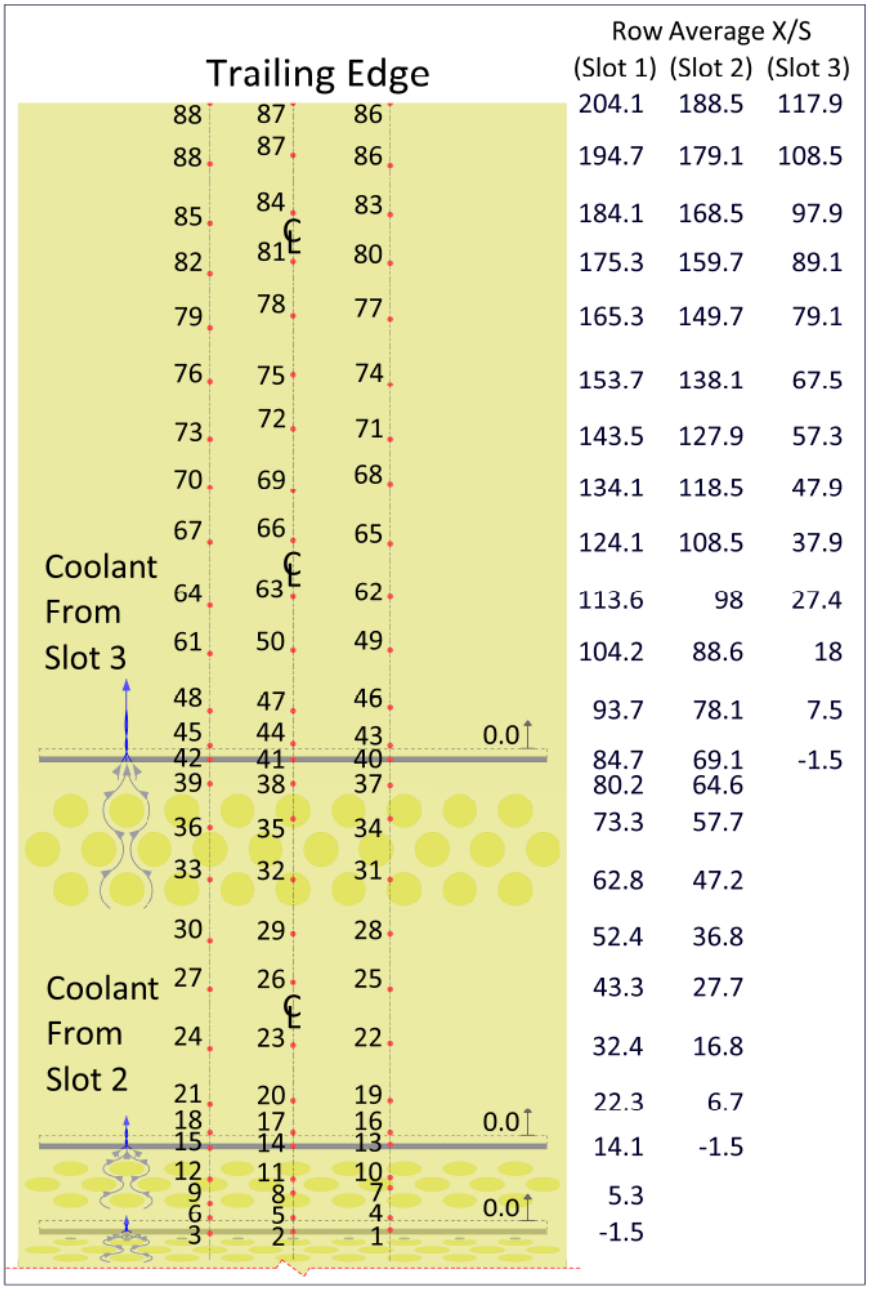


Figure 88. Schematic of suction side thermocouple layout.

Table 5. Thermocouple locations for Suction Side Vane.

| Row | Indicated Channel(s) for Quick Basic | Label Number(s) | Distance from Trailing Edge (in) | Distance from Stagnation Point (in) | Distance from Trailing Edge (m) | Distance from Stagnation Point (m) |
|---|---|---|---|---|---|---|
| 28 | 84 | 92 | 41.25 | -16.57 | 1.05 | -0.42 |
| 29 | 85 | 93 | 39.44 | -14.76 | 1.00 | -0.37 |
| 30 | 86 | 94 | 37.38 | -12.70 | 0.95 | -0.32 |
| 31 | 87 | 95 | 34.53 | -9.85 | 0.88 | -0.25 |
| 32 | 88 | 96 | 32.50 | -7.82 | 0.83 | -0.20 |
| 33 | 89 | 97 | 30.44 | -5.76 | 0.77 | -0.15 |
| 34 | 90 | 98 | 28.56 | -3.88 | 0.73 | -0.10 |
| 35 | 91 | 99 | 27.19 | -2.51 | 0.69 | -0.06 |
| 1 | 1-3 | 1-3 | 20.56 | 4.12 | 0.52 | 0.10 |
| 2 | 4-6 | 4-6 | 20.39 | 4.29 | 0.52 | 0.11 |
| 3 | 7-9 | 7-9 | 19.88 | 4.81 | 0.50 | 0.12 |
| 4 | 10-12 | 10-12 | 19.58 | 5.10 | 0.50 | 0.13 |
| 5 | 13-15 | 13-15 | 19.00 | 5.68 | 0.48 | 0.14 |
| 6 | 16-18 | 16-18 | 18.75 | 5.93 | 0.48 | 0.15 |
| 7 | 19-21 | 19-21 | 18.18 | 6.50 | 0.46 | 0.17 |
| 8 | 22-24 | 22-24 | 17.17 | 7.51 | 0.44 | 0.19 |
| 9 | 25-27 | 25-27 | 16.08 | 8.60 | 0.41 | 0.22 |
| 10 | 28-30 | 28-30 | 15.17 | 9.51 | 0.39 | 0.24 |
| 11 | 31-33 | 31-33 | 14.13 | 10.56 | 0.36 | 0.27 |
| 12 | 34-36 | 34-36 | 13.08 | 11.60 | 0.33 | 0.29 |
| 13 | 37-39 | 37-39 | 12.39 | 12.29 | 0.31 | 0.31 |
| 14 | 40-42 | 40-42 | 11.94 | 12.74 | 0.30 | 0.32 |
| 15 | 43-45 | 43-45 | 11.68 | 13.00 | 0.30 | 0.33 |
| 16 | 46-48 | 46-48 | 11.04 | 13.64 | 0.28 | 0.35 |
| 17 | 49,50,61 | 49,50,61 | 9.99 | 14.69 | 0.25 | 0.37 |
| 18 | 62-64 | 62-64 | 9.05 | 15.63 | 0.23 | 0.40 |
| 19 | 65-67 | 65-67 | 8.00 | 16.68 | 0.20 | 0.42 |
| 20 | 68-70 | 68-70 | 7.00 | 17.68 | 0.18 | 0.45 |
| 21 | 71-73 | 71-73 | 6.06 | 18.62 | 0.15 | 0.47 |
| 22 | 74-76 | 74-76 | 5.04 | 19.64 | 0.13 | 0.50 |
| 23 | 77 | 78 | 3.88 | 20.81 | 0.10 | 0.53 |
| 24 | 78 | 81 | 2.88 | 21.81 | 0.07 | 0.55 |
| 25 | 79 | 84 | 2.00 | 22.68 | 0.05 | 0.58 |
| 26 | 80 | 87 | 0.94 | 23.74 | 0.02 | 0.60 |
| 27 | 81-83 | 89-91 | 0.00 | 24.68 | 0.00 | 0.63 |

Appendix C

## Vane Test Matrices

Table 6. Pressure side test matrix.

| Turbulence | Blowing Ration configuration | | $Re_C$ | | |
|---|---|---|---|---|---|
| | # | PS1 | .5mil | 1mil | 2mil |
| High Turbulence | 0 | 0.00 | o | o | o |
| | 1 | 0.40 | o | o | o |
| | 2 | 0.70 | o | o | o |
| | 3 | 1.00 | o | o | o |
| Low Turbulence | 0 | 0.00 | o | o | o |
| | 1 | 0.40 | o | o | o |
| | 2 | 0.70 | o | o | o |
| | 3 | 1.00 | o | o | o |
| Large Grid | 0 | 0.00 | o | o | o |
| | 1 | 0.40 | o | o | o |
| | 2 | 0.70 | o | o | o |
| | 3 | 1.00 | o | o | o |
| Small Grid Far | 0 | 0.00 | o | o | o |
| | 1 | 0.40 | o | o | o |
| | 2 | 0.70 | o | o | o |
| | 3 | 1.00 | o | o | o |
| Aero-Combustor | 0 | 0.00 | o | o | o |
| | 1 | 0.40 | o | o | o |
| | 2 | 0.70 | o | o | o |
| | 3 | 1.00 | o | o | o |

Table 7. Suction side test matrix.

| Turbulence | Blowing Ratio (BR) Configuration | | | | $Re_C$ | | |
|---|---|---|---|---|---|---|---|
| | # | SS1 | SS2 | SS3 | .5mil | 1mil | 2mil |
| Low Turbulence Re = .5m, 1m and 2m with IR camera | 0 | 0.00 | 0.00 | 0.00 | o | o | o |
| | 1 | 0.50 | 0.15 | 0.15 | o | o | o |
| | 2 | 0.50 | 0.30 | 0.30 | o | o | o |
| | 3 | 1.00 | 0.15 | 0.15 | o | o | not capable |
| | 4 | 1.00 | 0.30 | 0.30 | o | o | not capable |
| Large Grid Re = 1m with IR camera | 0 | 0.00 | 0.00 | 0.00 | o | o | o |
| | 1 | 0.50 | 0.15 | 0.15 | o | o | o |
| | 2 | 0.50 | 0.30 | 0.30 | o | o | o |
| | 3 | 1.00 | 0.15 | 0.15 | o | o | not capable |
| | 4 | 1.00 | 0.30 | 0.30 | o | o | not capable |
| Small Grid Far Re = 1m with IR camera | 0 | 0.00 | 0.00 | 0.00 | o | o | o |
| | 1 | 0.50 | 0.15 | 0.15 | o | o | o |
| | 2 | 0.50 | 0.30 | 0.30 | o | o | o |
| | 3 | 1.00 | 0.15 | 0.15 | o | o | not capable |
| | 4 | 1.00 | 0.30 | 0.30 | o | o | not capable |
| | 5 | 0.50 | 0.00 | 0.00 | o | o | o |
| | 6 | 0.00 | 0.15 | 0.00 | o | o | o |
| | 7 | 0.00 | 0.00 | 0.15 | o | o | o |
| | 8 | 1.00 | 0.00 | 0.00 | o | o | not capable |
| | 9 | 0.00 | 0.30 | 0.00 | o | o | o |
| | z | 0.00 | 0.00 | 0.30 | o | o | o |
| Aero-Combustor - Re = .5m, 1m and 2m with IR camera | 0 | 0.00 | 0.00 | 0.00 | o | o | o |
| | 1 | 0.50 | 0.15 | 0.15 | o | o | o |
| | 2 | 0.50 | 0.30 | 0.30 | o | o | o |
| | 3 | 1.00 | 0.15 | 0.15 | o | o | not capable |
| | 4 | 1.00 | 0.30 | 0.30 | o | o | not capable |
| | 5 | 0.50 | 0.00 | 0.00 | o | o | o |
| | 6 | 0.00 | 0.15 | 0.00 | o | o | o |
| | 7 | 0.00 | 0.00 | 0.15 | o | o | o |
| | 8 | 1.00 | 0.00 | 0.00 | o | o | not capable |
| | 9 | 0.00 | 0.30 | 0.00 | o | o | o |
| | z | 0.00 | 0.00 | 0.30 | o | o | o |

# Appendix D

**Data Spreadsheets.** These following data sets were taken with the coolant slots inserts in the large leading edge aft loaded vane at the various turbulence intensities. Adiabatic effectiveness was calculated for each thermocouple using Eq. 1 [4] [50].

$$\eta = \frac{(T_{aw} - T_R)}{(T_{co} - T_R)} \qquad \text{Eq. 1}$$

Much of the data given here is illustrated in the figures throughout Chapter 4.

Table 8. Pressure side vane high turbulence condition data.

High Turbulence

| η | | | | | | | | | |
|---|---|---|---|---|---|---|---|---|---|
| ReC | 499984.27 | 499682.83 | 501452.43 | 1004216.67 | 1000810.50 | 1001114.45 | 1992962.50 | 2002420.67 | 1997762.67 |
| Blowing ratio | 0.40 | 0.68 | 1.01 | 0.39 | 0.68 | 1.00 | 0.39 | 0.69 | 0.96 |
| File name | BRP1R5HT | BRP2R5HT | BRP3R5HT | BRP1R1HT | BRP2R1HT | BRP3R1HT | BRP1R2HT | BRP2R2HT | BRP3R2HT |
| dist/slot height (X/S) | HT, Tu=17.44%, PS1 M=0.4, ReC=499984 | HT, Tu=17.44%, PS1 M=0.68, ReC=499683 | HT, Tu=17.44%, PS1 M=1.01, ReC=501452 | HT, Tu=17.44%, PS1 M=0.39, ReC=1004217 | HT, Tu=17.44%, PS1 M=0.68, ReC=1000811 | HT, Tu=17.44%, PS1 M=1, ReC=1001114 | HT, Tu=17.18%, PS1 M=0.39, ReC=1992963 | HT, Tu=17.18%, PS1 M=0.69, ReC=2002421 | HT, Tu=17.18%, PS1 M=0.96, ReC=1997763 |
| 0.00 | 1.00 | 1.00 | 1.00 | 1.00 | 1.00 | 1.00 | 1.00 | 1.00 | 1.00 |
| 2.34 | 0.88 | 0.87 | 0.87 | 0.89 | 0.86 | 0.88 | 0.87 | 0.88 | 0.89 |
| 8.53 | 0.71 | 0.67 | 0.66 | 0.67 | 0.64 | 0.66 | 0.61 | 0.65 | 0.68 |
| 18.80 | 0.49 | 0.48 | 0.50 | 0.42 | 0.47 | 0.51 | 0.39 | 0.47 | 0.51 |
| 28.38 | 0.37 | 0.39 | 0.43 | 0.30 | 0.39 | 0.44 | 0.29 | 0.40 | 0.44 |
| 38.74 | 0.28 | 0.32 | 0.37 | 0.23 | 0.32 | 0.38 | 0.22 | 0.32 | 0.37 |
| 48.59 | 0.22 | 0.27 | 0.33 | 0.18 | 0.27 | 0.33 | 0.18 | 0.27 | 0.33 |
| 57.96 | 0.18 | 0.23 | 0.29 | 0.15 | 0.23 | 0.29 | 0.15 | 0.23 | 0.29 |
| 70.25 | 0.06 | 0.07 | 0.09 | 0.05 | 0.07 | 0.09 | 0.04 | 0.07 | 0.09 |

Table 9. Pressure side vane aerocombustor turbulence condition data.

| Aerocombustor | | | | | | | | | |
|---|---|---|---|---|---|---|---|---|---|
| | η | | | | | | | | |
| ReC | 499669.47 | 499515.80 | 505633.02 | 1000101.93 | 998103.28 | 1000801.73 | 1976082.33 | 2000897.50 | 2008961.33 |
| Blowing ratio | 0.39 | 0.70 | 1.01 | 0.40 | 0.70 | 1.00 | 0.40 | 0.71 | 1.00 |
| File name | BRP1R5AC | BRP2R5AC | BRP3R5AC | BRP1R1AC | BRP2R1AC | BRP3R1AC | BRP1R2AC | BRP2R2AC | BRP3R2AC |
| dist/slot height (X/S) | AC, Tu=12.35%, PS1 M=0.39, ReC=499669 | AC, Tu=12.35%, PS1 M=0.7, ReC=499516 | AC, Tu=12.35%, PS1 M=1.01, ReC=505633 | AC, Tu=13.02%, PS1 M=0.4, ReC=1000102 | AC, Tu=13.02%, PS1 M=0.7, ReC=998103 | AC, Tu=13.02%, PS1 M=1, ReC=1000802 | AC, Tu=12.59%, PS1 M=0.4, ReC=1976082 | AC, Tu=12.59%, PS1 M=0.71, ReC=2000898 | AC, Tu=12.59%, PS1 M=1, ReC=2008961 |
| 1.00 | 1.00 | 1.00 | 1.00 | 1.00 | 1.00 | 1.00 | 1.00 | 1.00 | 1.00 |
| 0.88 | 0.88 | 0.87 | 0.88 | 0.90 | 0.88 | 0.88 | 0.90 | 0.89 | 0.90 |
| 0.68 | 0.71 | 0.67 | 0.68 | 0.70 | 0.67 | 0.67 | 0.66 | 0.68 | 0.70 |
| 0.52 | 0.50 | 0.48 | 0.52 | 0.45 | 0.50 | 0.52 | 0.43 | 0.50 | 0.53 |
| 0.44 | 0.38 | 0.40 | 0.44 | 0.34 | 0.42 | 0.45 | 0.33 | 0.41 | 0.46 |
| 0.39 | 0.29 | 0.34 | 0.39 | 0.25 | 0.35 | 0.39 | 0.26 | 0.35 | 0.39 |
| 0.35 | 0.24 | 0.29 | 0.35 | 0.20 | 0.30 | 0.35 | 0.21 | 0.30 | 0.35 |
| 0.31 | 0.20 | 0.25 | 0.31 | 0.17 | 0.26 | 0.31 | 0.18 | 0.26 | 0.31 |
| 0.11 | 0.06 | 0.08 | 0.11 | 0.05 | 0.09 | 0.10 | 0.06 | 0.09 | 0.11 |

Table 10. Pressure side vane large grid turbulence condition data.

Large Grid

| | η | | | | | | | | |
|---|---|---|---|---|---|---|---|---|---|
| ReC | 499387.10 | 500885.83 | 500501.65 | 1005065.17 | 999760.83 | 1002406.83 | 1976547.67 | 1998010.50 | 1999168.67 |
| Blowing ratio | 0.40 | 0.70 | 1.00 | 0.40 | 0.70 | 1.01 | 0.41 | 0.70 | 1.01 |
| File name | BRP1R5LG | BRP2R5LG | BRP3R5LG | BRP1R1LG | BRP2R1LG | BRP3R1LG | BRP1R2LG | BRP2R2LG | BRP3R2LG |
| dist/slot height (X/S) | LG, Tu=7.92%, PS1 M=0.4, ReC=499387 | LG, Tu=7.92%, PS1 M=0.7, ReC=500886 | LG, Tu=7.92%, PS1 M=1, ReC=500502 | LG, Tu=7.98%, PS1 M=0.4, ReC=1005065 | LG, Tu=7.98%, PS1 M=0.7, ReC=999761 | LG, Tu=7.98%, PS1 M=1.01, ReC=1002407 | LG, Tu=8.11%, PS1 M=0.41, ReC=1976548 | LG, Tu=8.11%, PS1 M=0.7, ReC=1998011 | LG, Tu=8.11%, PS1 M=1.01, ReC=1999169 |
| 1.00 | 1.00 | 1.00 | 1.00 | 1.00 | 1.00 | 1.00 | 1.00 | 1.00 | 1.00 |
| 0.89 | 0.89 | 0.87 | 0.88 | 0.90 | 0.89 | 0.89 | 0.90 | 0.89 | 0.90 |
| 0.67 | 0.73 | 0.68 | 0.67 | 0.73 | 0.67 | 0.68 | 0.68 | 0.68 | 0.70 |
| 0.50 | 0.55 | 0.50 | 0.52 | 0.49 | 0.50 | 0.53 | 0.46 | 0.51 | 0.54 |
| 0.42 | 0.42 | 0.41 | 0.44 | 0.37 | 0.42 | 0.45 | 0.35 | 0.42 | 0.47 |
| 0.37 | 0.34 | 0.35 | 0.40 | 0.29 | 0.37 | 0.40 | 0.29 | 0.37 | 0.42 |
| 0.32 | 0.27 | 0.31 | 0.36 | 0.24 | 0.32 | 0.37 | 0.24 | 0.32 | 0.39 |
| 0.29 | 0.23 | 0.28 | 0.34 | 0.20 | 0.29 | 0.33 | 0.21 | 0.29 | 0.36 |
| 0.10 | 0.08 | 0.09 | 0.12 | 0.06 | 0.10 | 0.12 | 0.07 | 0.10 | 0.13 |

Table 11. Pressure side vane small grid far turbulence condition data.

Small Grid Far

| | η | | | | | | | | |
|---|---|---|---|---|---|---|---|---|---|
| ReC | 500199.65 | 499930.48 | 500111.58 | 1000795.00 | 1000381.12 | 1001220.40 | 2000363.17 | 2000386.00 | 2000466.33 |
| Blowing ratio | 0.40 | 0.70 | 0.99 | 0.40 | 0.69 | 1.00 | 0.41 | 0.71 | 1.00 |
| File name | BRP1R5SG | BRP2R5SG | BRP3R5SG | BRP1R1SG | BRP2R1SG | BRP3R1SG | BRP1R2SG | BRP2R2SG | BRP3R2SG |
| dist/slot height (X/S) | SG, Tu=3.84%, PS1 M=0.4, ReC=500200 | SG, Tu=3.84%, PS1 M=0.7, ReC=499930 | SG, Tu=3.84%, PS1 M=0.99, ReC=500112 | SG, Tu=3.5%, PS1 M=0.4, ReC=1000795 | SG, Tu=3.5%, PS1 M=0.69, ReC=1000381 | SG, Tu=3.5%, PS1 M=1, ReC=1001220 | SG, Tu=3.48%, PS1 M=0.41, ReC=2000363 | SG, Tu=3.48%, PS1 M=0.71, ReC=2000386 | SG, Tu=3.48%, PS1 M=1, ReC=2000466 |
| 1.00 | 1.00 | 1.00 | 1.00 | 1.00 | 1.00 | 1.00 | 1.00 | 1.00 | 1.00 |
| 0.90 | 0.89 | 0.88 | 0.88 | 0.90 | 0.88 | 0.88 | 0.90 | 0.89 | 0.91 |
| 0.69 | 0.72 | 0.68 | 0.67 | 0.73 | 0.66 | 0.67 | 0.69 | 0.69 | 0.71 |
| 0.47 | 0.55 | 0.51 | 0.51 | 0.49 | 0.49 | 0.52 | 0.47 | 0.52 | 0.56 |
| 0.36 | 0.42 | 0.42 | 0.44 | 0.36 | 0.41 | 0.44 | 0.36 | 0.44 | 0.48 |
| 0.30 | 0.34 | 0.36 | 0.39 | 0.29 | 0.36 | 0.39 | 0.30 | 0.38 | 0.42 |
| 0.25 | 0.28 | 0.33 | 0.36 | 0.24 | 0.32 | 0.36 | 0.25 | 0.34 | 0.38 |
| 0.22 | 0.24 | 0.29 | 0.32 | 0.20 | 0.29 | 0.33 | 0.22 | 0.31 | 0.35 |
| 0.08 | 0.07 | 0.10 | 0.11 | 0.07 | 0.10 | 0.12 | 0.08 | 0.12 | 0.13 |

Table 12. Pressure side vane small grid far turbulence condition data.

Low Turbulence

| | η | | | | | | | |
|---|---|---|---|---|---|---|---|---|
| ReC | 500040.82 | 501280.25 | 500501.65 | 1000322.08 | 1005977.33 | 1002613.83 | 1995134.33 | 1998979.17 | 1999168.67 |
| Blowing ratio | 0.40 | 0.71 | 1.00 | 0.40 | 0.76 | 0.99 | 0.41 | 0.72 | 1.01 |
| File name | BRP1R5LT | BRP2R5LT | BRP3R5LT | BRP1R1LT | BRP2R1LT | BRP3R1LT | BRP1R2LT | BRP2R2LT | BRP3R2LT |
| dist/slot height (X/S) | LT, Tu=0.69%, PS1 M=0.4, ReC=500041 | LT, Tu=0.69%, PS1 M=0.71, ReC=501280 | LT, Tu=0.69%, PS1 M=1, ReC=500502 | LT, Tu=0.76%, PS1 M=0.4, ReC=1000322 | LT, Tu=0.76%, PS1 M=0.76, ReC=1005977 | LT, Tu=0.76%, PS1 M=0.99, ReC=1002614 | LT, Tu=0.6%, PS1 M=0.41, ReC=1995134 | LT, Tu=0.6%, PS1 M=0.72, ReC=1998979 | LT, Tu=0.6%, PS1 M=1.01, ReC=1999169 |
| 1.00 | 1.00 | 1.00 | 1.00 | 1.00 | 1.00 | 1.00 | 1.00 | 1.00 | 1.00 |
| 0.90 | 0.88 | 0.87 | 0.88 | 0.89 | 0.89 | 0.88 | 0.91 | 0.89 | 0.90 |
| 0.70 | 0.73 | 0.68 | 0.67 | 0.73 | 0.67 | 0.68 | 0.70 | 0.68 | 0.70 |
| 0.54 | 0.57 | 0.51 | 0.52 | 0.50 | 0.50 | 0.53 | 0.47 | 0.52 | 0.54 |
| 0.47 | 0.46 | 0.43 | 0.44 | 0.37 | 0.43 | 0.47 | 0.37 | 0.43 | 0.47 |
| 0.42 | 0.38 | 0.37 | 0.40 | 0.30 | 0.38 | 0.41 | 0.31 | 0.39 | 0.42 |
| 0.39 | 0.32 | 0.34 | 0.36 | 0.25 | 0.35 | 0.37 | 0.27 | 0.35 | 0.39 |
| 0.36 | 0.27 | 0.31 | 0.34 | 0.22 | 0.32 | 0.35 | 0.24 | 0.33 | 0.36 |
| 0.13 | 0.09 | 0.11 | 0.12 | 0.07 | 0.12 | 0.13 | 0.08 | 0.12 | 0.13 |

Table 13. Suction side vane aerocombustor turbulence condition data, $Re_C$ = 500,000.

| Aerocombustor | | | | | | | | | | | |
|---|---|---|---|---|---|---|---|---|---|---|---|
| η | | | | | | | | | | | |
| ReC | 501586.85 | 499018.12 | 498618.90 | 501671.93 | 500021.73 | 500258.30 | 499987.88 | 499498.50 | 499909.42 | 499132.23 | |
| SS1 | 0.50 | 0.50 | 1.02 | 1.00 | 0.50 | 0.00 | 0.00 | 1.02 | 0.00 | 0.00 | |
| SS2 | 0.15 | 0.31 | 0.15 | 0.30 | 0.00 | 0.15 | 0.00 | 0.00 | 0.30 | 0.00 | |
| SS3 | 0.15 | 0.31 | 0.16 | 0.30 | 0.00 | 0.00 | 0.15 | 0.00 | 0.00 | 0.31 | |
| Tu | 0.12 | 0.12 | 0.12 | 0.12 | 0.12 | 0.12 | 0.12 | 0.12 | 0.12 | 0.12 | |
| File name | BRS1R5AC | BSS2R5AC | BRS3R5AC | BRS4R5AC | BRS5R5AC | BRS6R5AC | BRS7R5AC | BRS8R5AC | BRS9R5AC | BRSZR5AC | |
| dist/slot height (X/S) | AC, Tu=12.35%, SS1=0.5, SS2=0.15, SS3=0.15, ReC=501587 | AC, Tu=12.35%, SS1=0.5, SS2=0.31, SS3=0.31, ReC=499018 | AC, Tu=12.35%, SS1=1.02, SS2=0.15, SS3=0.16, ReC=498619 | AC, Tu=12.35%, SS1=1, SS2=0.3, SS3=0.3, ReC=501672 | AC, Tu=12.35%, SS1=0.5, SS2=0, SS3=0, ReC=500022 | AC, Tu=12.35%, SS1=0, SS2=0.15, SS3=0, ReC=500258 | AC, Tu=12.35%, SS1=0, SS2=0, SS3=0.15, ReC=499988 | AC, Tu=12.35%, SS1=1.02, SS2=0, SS3=0, ReC=499499 | AC, Tu=12.35%, SS1=0, SS2=0.3, SS3=0, ReC=499909 | AC, Tu=12.35%, SS1=0, SS2=0, SS3=0.31, ReC=499132 | |
| 0.000 | 1.00 | 1.00 | 1.00 | 1.00 | 1.00 | 0.00 | 0.00 | 1.00 | 0.00 | 0.00 | |
| 1.000 | 0.93 | 0.95 | 0.93 | 0.93 | 0.87 | 0.00 | 0.00 | 0.89 | 0.00 | 0.00 | |
| 5.375 | 0.84 | 0.86 | 0.77 | 0.78 | 0.60 | 0.00 | 0.00 | 0.63 | 0.00 | 0.00 | |
| 8.292 | 0.78 | 0.86 | 0.72 | 0.75 | 0.54 | 0.00 | 0.00 | 0.57 | 0.00 | 0.00 | |
| 14.125 | 1.00 | 1.00 | 1.00 | 1.00 | 0.51 | 1.00 | 0.00 | 0.56 | 1.00 | 0.00 | |
| 16.625 | 0.97 | 0.97 | 0.98 | 0.97 | 0.42 | 0.95 | 0.00 | 0.52 | 1.00 | 0.00 | |
| 22.354 | 0.90 | 0.91 | 0.92 | 0.90 | 0.33 | 0.62 | 0.00 | 0.46 | 0.85 | 0.00 | |
| 32.458 | 0.80 | 0.78 | 0.81 | 0.79 | 0.24 | 0.34 | 0.00 | 0.36 | 0.56 | 0.00 | |
| 43.292 | 0.67 | 0.65 | 0.72 | 0.69 | 0.19 | 0.22 | 0.00 | 0.30 | 0.38 | 0.00 | |
| 52.458 | 0.58 | 0.56 | 0.63 | 0.61 | 0.16 | 0.18 | 0.00 | 0.26 | 0.31 | 0.00 | |
| 62.875 | 0.50 | 0.48 | 0.57 | 0.55 | 0.14 | 0.14 | 0.00 | 0.23 | 0.25 | 0.00 | |
| 73.292 | 0.45 | 0.43 | 0.53 | 0.50 | 0.12 | 0.12 | 0.00 | 0.20 | 0.21 | 0.00 | |
| 80.271 | 0.52 | 0.51 | 0.57 | 0.56 | 0.12 | 0.12 | 0.00 | 0.20 | 0.20 | 0.00 | |
| 84.750 | 1.00 | 1.00 | 1.00 | 1.00 | 0.11 | 0.14 | 1.00 | 0.18 | 0.19 | 1.00 | |
| 87.354 | 0.86 | 0.95 | 0.87 | 0.95 | 0.11 | 0.11 | 0.82 | 0.18 | 0.17 | 0.94 | |
| 93.708 | 0.62 | 0.77 | 0.68 | 0.78 | 0.10 | 0.09 | 0.47 | 0.17 | 0.16 | 0.69 | |
| 104.229 | 0.47 | 0.60 | 0.55 | 0.63 | 0.09 | 0.08 | 0.24 | 0.16 | 0.14 | 0.41 | |
| 113.604 | 0.42 | 0.52 | 0.50 | 0.56 | 0.09 | 0.07 | 0.17 | 0.15 | 0.13 | 0.31 | |
| 124.125 | 0.37 | 0.46 | 0.45 | 0.50 | 0.08 | 0.06 | 0.13 | 0.14 | 0.12 | 0.25 | |
| 134.125 | 0.33 | 0.41 | 0.41 | 0.45 | 0.08 | 0.05 | 0.11 | 0.14 | 0.11 | 0.20 | |
| 143.500 | 0.30 | 0.37 | 0.38 | 0.41 | 0.07 | 0.05 | 0.09 | 0.13 | 0.10 | 0.17 | |
| 153.708 | 0.28 | 0.34 | 0.35 | 0.38 | 0.07 | 0.04 | 0.07 | 0.12 | 0.09 | 0.15 | |
| 161.417 | 0.26 | 0.31 | 0.33 | 0.36 | 0.06 | 0.04 | 0.06 | 0.12 | 0.09 | 0.14 | |
| 172.042 | 0.24 | 0.30 | 0.32 | 0.34 | 0.06 | 0.03 | 0.06 | 0.11 | 0.08 | 0.12 | |
| 181.208 | 0.23 | 0.28 | 0.30 | 0.32 | 0.06 | 0.03 | 0.05 | 0.11 | 0.08 | 0.11 | |
| 191.208 | 0.21 | 0.26 | 0.28 | 0.30 | 0.05 | 0.03 | 0.05 | 0.10 | 0.07 | 0.10 | |
| 204.125 | 0.13 | 0.17 | 0.18 | 0.19 | 0.03 | 0.01 | 0.03 | 0.06 | 0.04 | 0.06 | |

Table 14. Suction side vane aerocombustor turbulence condition data, $Re_C$ = 1,000,000.

| Aerocombustor | | | | | | | | | | | |
|---|---|---|---|---|---|---|---|---|---|---|---|
| η | | | | | | | | | | | |
| ReC | 1000183.37 | 1001588.38 | 998396.02 | 1001974.93 | 1001138.02 | 999627.32 | 999129.13 | 1000032.54 | 1000570.48 | 1000190.80 |
| SS1 | 0.51 | 0.50 | 1.00 | 1.00 | 0.50 | 0.00 | 0.00 | 1.01 | 0.00 | 0.00 |
| SS2 | 0.16 | 0.30 | 0.15 | 0.30 | 0.00 | 0.15 | 0.00 | 0.00 | 0.30 | 0.00 |
| SS3 | 0.15 | 0.30 | 0.15 | 0.30 | 0.00 | 0.00 | 0.15 | 0.00 | 0.00 | 0.30 |
| Tu | 0.130 | 0.130 | 0.130 | 0.130 | 0.130 | 0.130 | 0.130 | 0.130 | 0.130 | 0.130 |
| File name | BRS1R1AC | BSP2R1AC | BRS3R1AC | BRS4R1AC | BRS5R1AC | BRS6R1AC | BRS7R1AC | BRS8R1AC | BRS9R1AC | BRSZR1AC |
| dist/slot height (X/S) | AC, Tu=13%, SS1=0.51, SS2=0.16, SS3=0.15, ReC=1000183 | AC, Tu=13%, SS1=0.5, SS2=0.3, SS3=0.3, ReC=1001588 | AC, Tu=13%, SS1=1, SS2=0.15, SS3=0.15, ReC=998396 | AC, Tu=13%, SS1=1, SS2=0.3, SS3=0.3, ReC=1001975 | AC, Tu=13%, SS1=0.5, SS2=0, SS3=0, ReC=1001138 | AC, Tu=13%, SS1=0, SS2=0.15, SS3=0, ReC=999627 | AC, Tu=13%, SS1=0, SS2=0, SS3=0.15, ReC=999129 | AC, Tu=13%, SS1=1.01, SS2=0, SS3=0, ReC=1000033 | AC, Tu=13%, SS1=0, SS2=0.3, SS3=0, ReC=1000570 | AC, Tu=13%, SS1=0, SS2=0, SS3=0.3, ReC=1000191 |
| 0.000 | 1.00 | 1.00 | 1.00 | 1.00 | 1.00 | 0.00 | 0.00 | 1.00 | 0.00 | 0.00 |
| 1.000 | 0.92 | 0.92 | 0.95 | 0.95 | 0.89 | 0.00 | 0.00 | 0.93 | 0.00 | 0.00 |
| 5.375 | 0.75 | 0.76 | 0.80 | 0.80 | 0.51 | 0.00 | 0.00 | 0.65 | 0.00 | 0.00 |
| 8.292 | 0.71 | 0.76 | 0.78 | 0.80 | 0.43 | 0.00 | 0.00 | 0.58 | 0.00 | 0.00 |
| 14.125 | 1.00 | 1.00 | 1.00 | 1.00 | 0.45 | 1.00 | 0.00 | 0.56 | 1.00 | 0.00 |
| 16.625 | 0.93 | 0.98 | 0.95 | 0.98 | 0.39 | 0.84 | 0.00 | 0.55 | 0.98 | 0.00 |
| 22.354 | 0.78 | 0.88 | 0.85 | 0.90 | 0.32 | 0.47 | 0.00 | 0.50 | 0.78 | 0.00 |
| 32.458 | 0.64 | 0.72 | 0.74 | 0.77 | 0.23 | 0.28 | 0.00 | 0.40 | 0.51 | 0.00 |
| 43.292 | 0.54 | 0.60 | 0.65 | 0.68 | 0.18 | 0.21 | 0.00 | 0.32 | 0.38 | 0.00 |
| 52.458 | 0.47 | 0.53 | 0.56 | 0.59 | 0.16 | 0.17 | 0.00 | 0.28 | 0.31 | 0.00 |
| 62.875 | 0.42 | 0.47 | 0.51 | 0.53 | 0.14 | 0.15 | 0.00 | 0.25 | 0.27 | 0.00 |
| 73.292 | 0.38 | 0.42 | 0.47 | 0.49 | 0.12 | 0.13 | 0.00 | 0.23 | 0.23 | 0.00 |
| 80.271 | 0.45 | 0.49 | 0.52 | 0.54 | 0.12 | 0.13 | 0.00 | 0.22 | 0.22 | 0.00 |
| 84.750 | 1.00 | 1.00 | 1.00 | 1.00 | 0.13 | 0.15 | 1.00 | 0.19 | 0.20 | 1.00 |
| 87.354 | 0.84 | 0.96 | 0.85 | 0.96 | 0.12 | 0.12 | 0.79 | 0.20 | 0.19 | 0.94 |
| 93.708 | 0.59 | 0.77 | 0.63 | 0.78 | 0.11 | 0.10 | 0.42 | 0.20 | 0.18 | 0.66 |
| 104.229 | 0.45 | 0.61 | 0.50 | 0.63 | 0.10 | 0.09 | 0.24 | 0.18 | 0.16 | 0.43 |
| 113.604 | 0.40 | 0.53 | 0.46 | 0.56 | 0.09 | 0.08 | 0.19 | 0.17 | 0.15 | 0.34 |
| 124.125 | 0.36 | 0.47 | 0.41 | 0.50 | 0.09 | 0.07 | 0.15 | 0.17 | 0.14 | 0.28 |
| 134.125 | 0.32 | 0.43 | 0.37 | 0.45 | 0.09 | 0.07 | 0.13 | 0.16 | 0.13 | 0.24 |
| 143.500 | 0.29 | 0.39 | 0.34 | 0.41 | 0.08 | 0.06 | 0.11 | 0.15 | 0.12 | 0.20 |
| 153.708 | 0.28 | 0.36 | 0.32 | 0.39 | 0.08 | 0.06 | 0.10 | 0.15 | 0.11 | 0.18 |
| 161.417 | 0.26 | 0.33 | 0.30 | 0.36 | 0.07 | 0.05 | 0.08 | 0.14 | 0.11 | 0.16 |
| 172.042 | 0.24 | 0.32 | 0.29 | 0.34 | 0.07 | 0.05 | 0.08 | 0.13 | 0.10 | 0.15 |
| 181.208 | 0.23 | 0.30 | 0.27 | 0.32 | 0.06 | 0.05 | 0.07 | 0.13 | 0.09 | 0.14 |
| 191.208 | 0.21 | 0.28 | 0.26 | 0.31 | 0.06 | 0.04 | 0.07 | 0.12 | 0.09 | 0.13 |
| 204.125 | 0.14 | 0.18 | 0.17 | 0.20 | 0.04 | 0.03 | 0.04 | 0.08 | 0.06 | 0.08 |

Table 15. Suction side vane aerocombustor turbulence condition data, $Re_C$ = 2,000,000.

| Aerocombustor | | | | | | | | |
|---|---|---|---|---|---|---|---|---|
| η | | | | | | | | |
| ReC | 1998005.83 | 2000162.67 | 2000366.83 | 2000698.17 | 2000508.33 | 2000031.17 | 2000208.67 | |
| SS1 | 0.49 | 0.50 | 0.49 | 0.00 | 0.00 | 0.00 | 0.00 | |
| SS2 | 0.15 | 0.30 | 0.00 | 0.15 | 0.00 | 0.31 | 0.00 | |
| SS3 | 0.15 | 0.30 | 0.00 | 0.00 | 0.15 | 0.00 | 0.30 | |
| Tu | 0.126 | 0.126 | 0.126 | 0.126 | 0.126 | 0.126 | 0.126 | |
| File name | BRS1R2AC | BRS2R2AC | BRS5R2AC | BRS6R2AC | BRS7R2AC | BRS9R2AC | BRS2R2AC | |
| dist/slot height (X/S) | AC, Tu=12.6%, SS1=0.49, SS2=0.15, SS3=0.15, ReC=1998006 | AC, Tu=12.6%, SS1=0.5, SS2=0.3, SS3=0.3, ReC=2000163 | AC, Tu=12.6%, SS1=0.49, SS2=0, SS3=0, ReC=2000367 | AC, Tu=12.6%, SS1=0, SS2=0.15, SS3=0, ReC=2000698 | AC, Tu=12.6%, SS1=0, SS2=0, SS3=0.15, ReC=2000508 | AC, Tu=12.6%, SS1=0, SS2=0.31, SS3=0, ReC=2000031 | AC, Tu=12.6%, SS1=0, SS2=0, SS3=0.3, ReC=2000209 | |
| 0.000 | 1.00 | 1.00 | 1.00 | 0.00 | 0.00 | 0.00 | 0.00 | |
| 1.000 | 0.95 | 0.95 | 0.92 | 0.00 | 0.00 | 0.00 | 0.00 | |
| 5.375 | 0.77 | 0.78 | 0.63 | 0.00 | 0.00 | 0.00 | 0.00 | |
| 8.292 | 0.75 | 0.77 | 0.60 | 0.00 | 0.00 | 0.00 | 0.00 | |
| 14.125 | 1.00 | 1.00 | 0.57 | 1.00 | 0.00 | 1.00 | 0.00 | |
| 16.625 | 0.94 | 0.99 | 0.46 | 0.95 | 0.00 | 1.00 | 0.00 | |
| 22.354 | 0.79 | 0.90 | 0.38 | 0.62 | 0.00 | 0.85 | 0.00 | |
| 32.458 | 0.64 | 0.75 | 0.29 | 0.34 | 0.00 | 0.56 | 0.00 | |
| 43.292 | 0.55 | 0.64 | 0.24 | 0.22 | 0.00 | 0.38 | 0.00 | |
| 52.458 | 0.48 | 0.57 | 0.21 | 0.18 | 0.00 | 0.31 | 0.00 | |
| 62.875 | 0.43 | 0.51 | 0.19 | 0.14 | 0.00 | 0.25 | 0.00 | |
| 73.292 | 0.39 | 0.46 | 0.18 | 0.12 | 0.00 | 0.21 | 0.00 | |
| 80.271 | 0.46 | 0.52 | 0.17 | 0.12 | 0.00 | 0.20 | 0.00 | |
| 84.750 | 1.00 | 1.00 | 0.19 | 0.14 | 1.00 | 0.19 | 1.00 | |
| 87.354 | 0.85 | 0.98 | 0.17 | 0.11 | 0.82 | 0.17 | 0.94 | |
| 93.708 | 0.60 | 0.80 | 0.16 | 0.09 | 0.47 | 0.16 | 0.69 | |
| 104.229 | 0.47 | 0.64 | 0.14 | 0.08 | 0.24 | 0.14 | 0.41 | |
| 113.604 | 0.42 | 0.57 | 0.14 | 0.07 | 0.17 | 0.13 | 0.31 | |
| 124.125 | 0.38 | 0.51 | 0.13 | 0.06 | 0.13 | 0.12 | 0.25 | |
| 134.125 | 0.34 | 0.46 | 0.12 | 0.05 | 0.11 | 0.11 | 0.20 | |
| 143.500 | 0.32 | 0.43 | 0.12 | 0.05 | 0.09 | 0.10 | 0.17 | |
| 153.708 | 0.30 | 0.40 | 0.11 | 0.04 | 0.07 | 0.09 | 0.15 | |
| 161.417 | 0.28 | 0.37 | 0.11 | 0.04 | 0.06 | 0.09 | 0.14 | |
| 172.042 | 0.26 | 0.35 | 0.10 | 0.03 | 0.06 | 0.08 | 0.12 | |
| 181.208 | 0.25 | 0.33 | 0.10 | 0.03 | 0.05 | 0.08 | 0.11 | |
| 191.208 | 0.24 | 0.32 | 0.09 | 0.03 | 0.05 | 0.07 | 0.10 | |
| 204.125 | 0.16 | 0.21 | 0.07 | 0.01 | 0.03 | 0.04 | 0.06 | |

Table 16. Suction side vane large grid turbulence condition data.

| Large Grid | | | | | | | | | | | |
|---|---|---|---|---|---|---|---|---|---|---|---|
| η | | | | | | | | | | | |
| ReC | 500543.83 | 499814.93 | 500372.27 | 499746.67 | 998873.35 | 1001170.50 | 1000827.93 | 999902.77 | 2000465.33 | 2001050.00 |
| SS1 | 0.50 | 0.50 | 1.01 | 1.00 | 0.50 | 0.50 | 1.00 | 1.00 | 0.50 | 0.51 |
| SS2 | 0.15 | 0.30 | 0.15 | 0.30 | 0.15 | 0.30 | 0.15 | 0.30 | 0.15 | 0.30 |
| SS3 | 0.15 | 0.30 | 0.15 | 0.30 | 0.15 | 0.30 | 0.15 | 0.30 | 0.15 | 0.30 |
| Tu | 0.08 | 0.08 | 0.08 | 0.08 | 0.080 | 0.080 | 0.080 | 0.080 | 0.081 | 0.081 |
| File name | BRS1R5LG | BSS2R5LG | BRS3R5LG | BRS4R5LG | BRS1R1LG | BSP2R1LG | BRS3R1LG | BRS4R1LG | BRS1R2LG | BRS2R2LG |
| dist/slot height (X/S) | LG, Tu=7.92%, SS1=0.5, SS2=0.15, SS3=0.15, ReC=500544 | LG, Tu=7.92%, SS1=0.5, SS2=0.3, SS3=0.3, ReC=499815 | LG, Tu=7.92%, SS1=1.01, SS2=0.15, SS3=0.15, ReC=500372 | LG, Tu=7.92%, SS1=1, SS2=0.3, SS3=0.3, ReC=499747 | LG, Tu=8%, SS1=0.5, SS2=0.15, SS3=0.15, ReC=998873 | LG, Tu=8%, SS1=0.5, SS2=0.3, SS3=0.3, ReC=1001171 | LG, Tu=8%, SS1=1, SS2=0.15, SS3=0.15, ReC=1000828 | LG, Tu=8%, SS1=1, SS2=0.3, SS3=0.3, ReC=999903 | LG, Tu=8.1%, SS1=0.5, SS2=0.15, SS3=0.15, ReC=2000465 | LG, Tu=8.1%, SS1=0.51, SS2=0.3, SS3=0.3, ReC=2001050 |
| 0.000 | 1.00 | 1.00 | 1.00 | 1.00 | 1.00 | 1.00 | 1.00 | 1.00 | 1.00 | 1.00 |
| 1.000 | 0.94 | 0.94 | 0.92 | 0.92 | 0.93 | 0.93 | 0.95 | 0.95 | 0.93 | 0.93 |
| 5.375 | 0.84 | 0.85 | 0.76 | 0.77 | 0.76 | 0.77 | 0.80 | 0.80 | 0.75 | 0.75 |
| 8.292 | 0.77 | 0.84 | 0.69 | 0.73 | 0.72 | 0.76 | 0.76 | 0.79 | 0.72 | 0.74 |
| 14.125 | 1.00 | 1.00 | 1.00 | 1.00 | 1.00 | 1.00 | 1.00 | 1.00 | 1.00 | 1.00 |
| 16.625 | 0.97 | 0.97 | 0.99 | 0.97 | 0.94 | 0.98 | 0.96 | 0.98 | 0.95 | 0.99 |
| 22.354 | 0.91 | 0.91 | 0.98 | 0.91 | 0.80 | 0.89 | 0.90 | 0.91 | 0.79 | 0.90 |
| 32.458 | 0.81 | 0.80 | 0.91 | 0.81 | 0.67 | 0.75 | 0.81 | 0.81 | 0.66 | 0.76 |
| 43.292 | 0.69 | 0.68 | 0.83 | 0.73 | 0.58 | 0.64 | 0.73 | 0.72 | 0.57 | 0.66 |
| 52.458 | 0.59 | 0.58 | 0.73 | 0.64 | 0.51 | 0.57 | 0.64 | 0.64 | 0.51 | 0.59 |
| 62.875 | 0.52 | 0.51 | 0.67 | 0.59 | 0.46 | 0.51 | 0.59 | 0.59 | 0.46 | 0.53 |
| 73.292 | 0.47 | 0.46 | 0.62 | 0.54 | 0.43 | 0.47 | 0.55 | 0.55 | 0.42 | 0.49 |
| 80.271 | 0.51 | 0.52 | 0.63 | 0.59 | 0.49 | 0.54 | 0.58 | 0.59 | 0.47 | 0.54 |
| 84.750 | 1.00 | 1.00 | 1.00 | 1.00 | 1.00 | 1.00 | 1.00 | 1.00 | 1.00 | 1.00 |
| 87.354 | 0.85 | 0.95 | 0.87 | 0.94 | 0.85 | 0.96 | 0.86 | 0.96 | 0.86 | 0.98 |
| 93.708 | 0.64 | 0.77 | 0.72 | 0.79 | 0.62 | 0.79 | 0.68 | 0.80 | 0.61 | 0.81 |
| 104.229 | 0.50 | 0.60 | 0.60 | 0.64 | 0.49 | 0.64 | 0.56 | 0.66 | 0.49 | 0.67 |
| 113.604 | 0.46 | 0.53 | 0.56 | 0.58 | 0.45 | 0.57 | 0.51 | 0.60 | 0.44 | 0.60 |
| 124.125 | 0.41 | 0.47 | 0.50 | 0.51 | 0.40 | 0.51 | 0.46 | 0.53 | 0.40 | 0.54 |
| 134.125 | 0.38 | 0.43 | 0.45 | 0.46 | 0.37 | 0.47 | 0.40 | 0.47 | 0.37 | 0.49 |
| 143.500 | 0.35 | 0.39 | 0.42 | 0.42 | 0.34 | 0.43 | 0.37 | 0.43 | 0.34 | 0.46 |
| 153.708 | 0.33 | 0.37 | 0.40 | 0.40 | 0.32 | 0.40 | 0.36 | 0.41 | 0.33 | 0.43 |
| 161.417 | 0.31 | 0.34 | 0.38 | 0.37 | 0.30 | 0.38 | 0.33 | 0.38 | 0.31 | 0.41 |
| 172.042 | 0.30 | 0.33 | 0.36 | 0.36 | 0.29 | 0.36 | 0.32 | 0.37 | 0.29 | 0.39 |
| 181.208 | 0.28 | 0.31 | 0.35 | 0.34 | 0.28 | 0.34 | 0.31 | 0.35 | 0.28 | 0.37 |
| 191.208 | 0.27 | 0.29 | 0.33 | 0.33 | 0.26 | 0.33 | 0.29 | 0.33 | 0.27 | 0.35 |
| 204.125 | 0.18 | 0.20 | 0.22 | 0.22 | 0.19 | 0.23 | 0.20 | 0.23 | 0.19 | 0.24 |

Table 17. Suction side vane low turbulence turbulence condition data.

| Low Trubulence | | | | | | | | | | | |
|---|---|---|---|---|---|---|---|---|---|---|---|
| η | | | | | | | | | | | |
| ReC | 499309.23 | 499913.37 | 499569.03 | 499482.83 | 999963.73 | 999418.42 | 999629.45 | 1000292.67 | 2000417.50 | 1999926.50 |
| SS1 | 0.50 | 0.50 | 1.00 | 1.00 | 0.50 | 0.50 | 1.00 | 1.00 | 0.50 | 0.50 |
| SS2 | 0.15 | 0.30 | 0.15 | 0.30 | 0.15 | 0.30 | 0.15 | 0.30 | 0.15 | 0.30 |
| SS3 | 0.15 | 0.30 | 0.15 | 0.30 | 0.15 | 0.30 | 0.15 | 0.30 | 0.15 | 0.30 |
| Tu | 0.01 | 0.01 | 0.01 | 0.01 | 0.008 | 0.008 | 0.008 | 0.008 | 0.006 | 0.006 |
| File name | BRS1R5LT | BSS2R5LT | BRS3R5LT | BRS4R5LT | BRS1R1LT | BSP2R1LT | BRS3R1LT | BRS4R1LT | BRS1R2LT | BRS2R2LT |
| dist/slot height (X/S) | LT, Tu=0.69%, SS1=0.5, SS2=0.15, SS3=0.15, ReC=499309 | LT, Tu=0.69%, SS1=0.5, SS2=0.3, SS3=0.3, ReC=499913 | LT, Tu=0.69%, SS1=1, SS2=0.15, SS3=0.15, ReC=499569 | LT, Tu=0.69%, SS1=1, SS2=0.3, SS3=0.3, ReC=499483 | LT, Tu=0.8%, SS1=0.5, SS2=0.15, SS3=0.15, ReC=999964 | LT, Tu=0.8%, SS1=0.5, SS2=0.3, SS3=0.3, ReC=999418 | LT, Tu=0.8%, SS1=1, SS2=0.15, SS3=0.15, ReC=999629 | LT, Tu=0.8%, SS1=1, SS2=0.3, SS3=0.3, ReC=1000293 | LT, Tu=0.6%, SS1=0.5, SS2=0.15, SS3=0.15, ReC=2000418 | LT, Tu=0.6%, SS1=0.5, SS2=0.3, SS3=0.3, ReC=1999927 |
| 0.000 | 1.00 | 1.00 | 1.00 | 1.00 | 1.00 | 1.00 | 1.00 | 1.00 | 1.00 | 1.00 |
| 1.000 | 0.94 | 0.94 | 0.92 | 0.93 | 0.91 | 0.92 | 0.94 | 0.95 | 0.89 | 0.89 |
| 5.375 | 0.83 | 0.85 | 0.76 | 0.77 | 0.75 | 0.75 | 0.80 | 0.80 | 0.65 | 0.65 |
| 8.292 | 0.78 | 0.84 | 0.70 | 0.75 | 0.71 | 0.74 | 0.77 | 0.80 | 0.60 | 0.63 |
| 14.125 | 1.00 | 1.00 | 1.00 | 1.00 | 1.00 | 1.00 | 1.00 | 1.00 | 1.00 | 1.00 |
| 16.625 | 0.97 | 0.97 | 0.99 | 0.97 | 0.93 | 0.98 | 0.95 | 0.97 | 0.92 | 0.99 |
| 22.354 | 0.91 | 0.91 | 0.95 | 0.91 | 0.78 | 0.88 | 0.88 | 0.91 | 0.71 | 0.87 |
| 32.458 | 0.81 | 0.81 | 0.88 | 0.81 | 0.66 | 0.74 | 0.80 | 0.81 | 0.57 | 0.71 |
| 43.292 | 0.72 | 0.71 | 0.81 | 0.72 | 0.59 | 0.64 | 0.74 | 0.74 | 0.49 | 0.60 |
| 52.458 | 0.63 | 0.62 | 0.74 | 0.66 | 0.53 | 0.58 | 0.67 | 0.68 | 0.44 | 0.54 |
| 62.875 | 0.56 | 0.55 | 0.70 | 0.61 | 0.49 | 0.53 | 0.63 | 0.63 | 0.39 | 0.49 |
| 73.292 | 0.51 | 0.50 | 0.67 | 0.58 | 0.46 | 0.49 | 0.61 | 0.61 | 0.36 | 0.44 |
| 80.271 | 0.55 | 0.56 | 0.68 | 0.62 | 0.52 | 0.55 | 0.63 | 0.64 | 0.43 | 0.50 |
| 84.750 | 1.00 | 1.00 | 1.00 | 1.00 | 1.00 | 1.00 | 1.00 | 1.00 | 1.00 | 1.00 |
| 87.354 | 0.86 | 0.95 | 0.90 | 0.95 | 0.86 | 0.96 | 0.89 | 0.96 | 0.85 | 0.97 |
| 93.708 | 0.66 | 0.79 | 0.77 | 0.82 | 0.64 | 0.80 | 0.73 | 0.83 | 0.58 | 0.80 |
| 104.229 | 0.53 | 0.63 | 0.67 | 0.68 | 0.52 | 0.66 | 0.63 | 0.71 | 0.45 | 0.65 |
| 113.604 | 0.48 | 0.56 | 0.64 | 0.62 | 0.47 | 0.59 | 0.59 | 0.66 | 0.39 | 0.57 |
| 124.125 | 0.44 | 0.50 | 0.58 | 0.56 | 0.43 | 0.53 | 0.54 | 0.60 | 0.34 | 0.51 |
| 134.125 | 0.39 | 0.45 | 0.50 | 0.48 | 0.39 | 0.48 | 0.46 | 0.52 | 0.29 | 0.45 |
| 143.500 | 0.36 | 0.41 | 0.47 | 0.45 | 0.36 | 0.45 | 0.43 | 0.49 | 0.26 | 0.41 |
| 153.708 | 0.34 | 0.39 | 0.46 | 0.43 | 0.34 | 0.43 | 0.43 | 0.47 | 0.24 | 0.38 |
| 161.417 | 0.32 | 0.36 | 0.42 | 0.40 | 0.32 | 0.40 | 0.39 | 0.44 | 0.22 | 0.35 |
| 172.042 | 0.30 | 0.35 | 0.41 | 0.38 | 0.31 | 0.38 | 0.38 | 0.42 | 0.20 | 0.33 |
| 181.208 | 0.29 | 0.33 | 0.39 | 0.36 | 0.29 | 0.36 | 0.36 | 0.41 | 0.18 | 0.31 |
| 191.208 | 0.27 | 0.31 | 0.36 | 0.33 | 0.28 | 0.34 | 0.34 | 0.38 | 0.16 | 0.29 |
| 204.125 | 0.19 | 0.21 | 0.24 | 0.20 | 0.20 | 0.25 | 0.22 | 0.25 | 0.07 | 0.16 |

Table 18. Suction side vane small grid far turbulence condition data, $Re_C$ = 500,000.

| | | Small Grid Far | | | | | | | | | | |
|---|---|---|---|---|---|---|---|---|---|---|---|---|
| | | n | | | | | | | | | | |
| ReC | | 500129.27 | 500510.37 | 500031.20 | 499361.37 | 500208.23 | 498515.87 | 500684.33 | 500696.10 | 496357.93 | 499849.67 | |
| SS1 | | 0.50 | 0.50 | 1.00 | 1.00 | 0.51 | 0.00 | 0.00 | 1.02 | 0.00 | 0.00 | |
| SS2 | | 0.15 | 0.30 | 0.15 | 0.30 | 0.00 | 0.15 | 0.00 | 0.00 | 0.30 | 0.00 | |
| SS3 | | 0.15 | 0.30 | 0.15 | 0.30 | 0.00 | 0.00 | 0.15 | 0.00 | 0.00 | 0.30 | |
| Tu | | 0.04 | 0.04 | 0.04 | 0.04 | 0.04 | 0.04 | 0.04 | 0.04 | 0.04 | 0.04 | |
| File name | | BRS1R5SG | BSS2R5SG | BRS3R5SG | BRS4R5SG | BRS5R5SG | BRS6R5SG | BRS7R5SG | BRS8R5SG | BRS9R5SG | BRSZR5SG | |
| dist/slot height (X/S) | | SG, Tu=3.84%, SS1=0.5, SS2=0.15, SS3=0.15, ReC=500129 | SG, Tu=3.84%, SS1=0.5, SS2=0.3, SS3=0.3, ReC=500510 | SG, Tu=3.84%, SS1=1, SS2=0.15, SS3=0.15, ReC=500031 | SG, Tu=3.84%, SS1=1, SS2=0.3, SS3=0.3, ReC=499361 | SG, Tu=3.84%, SS1=0.51, SS2=0, SS3=0, ReC=500208 | SG, Tu=3.84%, SS1=0, SS2=0.15, SS3=0, ReC=498516 | SG, Tu=3.84%, SS1=0, SS2=0, SS3=0.15, ReC=500684 | SG, Tu=3.84%, SS1=1.02, SS2=0, SS3=0, ReC=500696 | SG, Tu=3.84%, SS1=0, SS2=0.3, SS3=0, ReC=496358 | SG, Tu=3.84%, SS1=0, SS2=0, SS3=0.3, ReC=499850 | |
| 0.000 | | 1.00 | 1.00 | 1.00 | 1.00 | 1.00 | 0.00 | 0.00 | 1.00 | 0.00 | 0.00 | |
| 1.000 | | 0.94 | 0.95 | 0.93 | 0.93 | 0.91 | 0.00 | 0.00 | 0.93 | 0.00 | 0.00 | |
| 5.375 | | 0.84 | 0.85 | 0.77 | 0.78 | 0.83 | 0.00 | 0.00 | 0.77 | 0.00 | 0.00 | |
| 8.292 | | 0.78 | 0.84 | 0.70 | 0.75 | 0.77 | 0.00 | 0.00 | 0.72 | 0.00 | 0.00 | |
| 14.125 | | 1.00 | 1.00 | 1.00 | 1.00 | 0.69 | 1.00 | 0.00 | 0.66 | 1.00 | 0.00 | |
| 16.625 | | 0.98 | 0.97 | 1.00 | 0.97 | 0.66 | 0.95 | 0.00 | 0.62 | 1.00 | 0.00 | |
| 22.354 | | 0.92 | 0.91 | 0.99 | 0.91 | 0.62 | 0.64 | 0.00 | 0.58 | 0.84 | 0.00 | |
| 32.458 | | 0.84 | 0.81 | 0.93 | 0.83 | 0.55 | 0.36 | 0.00 | 0.54 | 0.57 | 0.00 | |
| 43.292 | | 0.75 | 0.71 | 0.86 | 0.75 | 0.50 | 0.25 | 0.00 | 0.50 | 0.40 | 0.00 | |
| 52.458 | | 0.66 | 0.62 | 0.78 | 0.68 | 0.45 | 0.20 | 0.00 | 0.45 | 0.33 | 0.00 | |
| 62.875 | | 0.59 | 0.56 | 0.73 | 0.63 | 0.41 | 0.17 | 0.00 | 0.42 | 0.28 | 0.00 | |
| 73.292 | | 0.54 | 0.51 | 0.70 | 0.60 | 0.37 | 0.15 | 0.00 | 0.40 | 0.25 | 0.00 | |
| 80.271 | | 0.58 | 0.57 | 0.71 | 0.64 | 0.34 | 0.16 | 0.00 | 0.36 | 0.25 | 0.00 | |
| 84.750 | | 1.00 | 1.00 | 1.00 | 1.00 | 0.29 | 0.21 | 1.00 | 0.30 | 0.30 | 1.00 | |
| 87.354 | | 0.87 | 0.95 | 0.90 | 0.95 | 0.29 | 0.16 | 0.97 | 0.32 | 0.25 | 0.96 | |
| 93.708 | | 0.68 | 0.79 | 0.78 | 0.82 | 0.30 | 0.13 | 0.83 | 0.34 | 0.21 | 0.82 | |
| 104.229 | | 0.55 | 0.64 | 0.68 | 0.69 | 0.27 | 0.11 | 0.66 | 0.31 | 0.19 | 0.52 | |
| 113.604 | | 0.50 | 0.57 | 0.64 | 0.63 | 0.24 | 0.10 | 0.36 | 0.29 | 0.18 | 0.35 | |
| 124.125 | | 0.46 | 0.51 | 0.58 | 0.57 | 0.22 | 0.10 | 0.20 | 0.26 | 0.17 | 0.28 | |
| 134.125 | | 0.42 | 0.46 | 0.50 | 0.50 | 0.21 | 0.09 | 0.15 | 0.21 | 0.17 | 0.23 | |
| 143.500 | | 0.39 | 0.43 | 0.48 | 0.46 | 0.19 | 0.09 | 0.12 | 0.20 | 0.16 | 0.20 | |
| 153.708 | | 0.37 | 0.40 | 0.46 | 0.44 | 0.18 | 0.08 | 0.10 | 0.20 | 0.15 | 0.18 | |
| 161.417 | | 0.34 | 0.38 | 0.43 | 0.41 | 0.16 | 0.08 | 0.09 | 0.18 | 0.14 | 0.17 | |
| 172.042 | | 0.33 | 0.36 | 0.42 | 0.40 | 0.15 | 0.07 | 0.08 | 0.16 | 0.14 | 0.15 | |
| 181.208 | | 0.31 | 0.34 | 0.40 | 0.38 | 0.15 | 0.07 | 0.08 | 0.17 | 0.13 | 0.15 | |
| 191.208 | | 0.30 | 0.32 | 0.37 | 0.36 | 0.14 | 0.07 | 0.08 | 0.16 | 0.13 | 0.14 | |
| 204.125 | | 0.21 | 0.22 | 0.26 | 0.24 | 0.11 | 0.05 | 0.05 | 0.11 | 0.09 | 0.09 | |

Table 19. Suction side vane small grid far turbulence condition data, $Re_C$ = 1,000,000.

| Small Grid Far | | | | | | | | | | | | |
|---|---|---|---|---|---|---|---|---|---|---|---|---|
| n | | | | | | | | | | | | |
| ReC | 1000343.27 | 999454.35 | 1000066.03 | 1001974.93 | 1001164.50 | 1001666.83 | 998837.93 | 1000195.25 | 1002347.33 | 1000427.50 | | |
| SS1 | 0.50 | 0.50 | 1.01 | 1.00 | 0.50 | 0.00 | 0.00 | 1.00 | 0.00 | 0.00 | | |
| SS2 | 0.15 | 0.30 | 0.15 | 0.30 | 0.00 | 0.15 | 0.00 | 0.00 | 0.30 | 0.00 | | |
| SS3 | 0.15 | 0.30 | 0.15 | 0.30 | 0.00 | 0.00 | 0.15 | 0.00 | 0.00 | 0.30 | | |
| Tu | 0.035 | 0.035 | 0.035 | 0.035 | 0.035 | 0.035 | 0.035 | 0.035 | 0.035 | 0.035 | | |
| File name | BRS1R1SG | BRP2R1SG | BRS3R1SG | BRS4R1SG | BRS5R1SG | BRS6R1SG | BRS7R1SG | BRS8R1SG | BRS9R1SG | BRSZR1SG | | |
| dist/slot height (X/S) | SG, Tu=3.5%, SS1=0.5, SS2=0.15, SS3=0.15, ReC=1000343 | SG, Tu=3.5%, SS1=0.5, SS2=0.3, SS3=0.3, ReC=999454 | SG, Tu=3.5%, SS1=1.01, SS2=0.15, SS3=0.15, ReC=1000066 | SG, Tu=3.5%, SS1=1, SS2=0.3, SS3=0.3, ReC=1001975 | SG, Tu=3.5%, SS1=0.5, SS2=0, SS3=0, ReC=1001165 | SG, Tu=3.5%, SS1=0, SS2=0.15, SS3=0, ReC=1001667 | SG, Tu=3.5%, SS1=0, SS2=0, SS3=0.15, ReC=998838 | SG, Tu=3.5%, SS1=1, SS2=0, SS3=0, ReC=1000195 | SG, Tu=3.5%, SS1=0, SS2=0.3, SS3=0, ReC=1002347 | SG, Tu=3.5%, SS1=0, SS2=0, SS3=0.3, ReC=1000428 | | |
| 0.000 | 1.00 | 1.00 | 1.00 | 1.00 | 1.00 | 0.00 | 0.00 | 1.00 | 0.00 | 0.00 | | |
| 1.000 | 0.92 | 0.92 | 0.95 | 0.95 | 0.92 | 0.00 | 0.00 | 0.95 | 0.00 | 0.00 | | |
| 5.375 | 0.76 | 0.76 | 0.80 | 0.81 | 0.76 | 0.00 | 0.00 | 0.80 | 0.00 | 0.00 | | |
| 8.292 | 0.71 | 0.75 | 0.76 | 0.80 | 0.69 | 0.00 | 0.00 | 0.75 | 0.00 | 0.00 | | |
| 14.125 | 1.00 | 1.00 | 1.00 | 1.00 | 0.63 | 1.00 | 0.00 | 0.68 | 1.00 | 0.00 | | |
| 16.625 | 0.95 | 0.98 | 0.97 | 0.98 | 0.56 | 0.85 | 0.00 | 0.65 | 0.98 | 0.00 | | |
| 22.354 | 0.82 | 0.89 | 0.93 | 0.90 | 0.52 | 0.49 | 0.00 | 0.62 | 0.78 | 0.00 | | |
| 32.458 | 0.71 | 0.76 | 0.86 | 0.78 | 0.46 | 0.31 | 0.00 | 0.57 | 0.52 | 0.00 | | |
| 43.292 | 0.63 | 0.66 | 0.79 | 0.68 | 0.41 | 0.24 | 0.00 | 0.52 | 0.39 | 0.00 | | |
| 52.458 | 0.57 | 0.60 | 0.71 | 0.59 | 0.37 | 0.20 | 0.00 | 0.46 | 0.34 | 0.00 | | |
| 62.875 | 0.52 | 0.55 | 0.67 | 0.53 | 0.34 | 0.18 | 0.00 | 0.43 | 0.29 | 0.00 | | |
| 73.292 | 0.49 | 0.51 | 0.64 | 0.50 | 0.31 | 0.16 | 0.00 | 0.40 | 0.26 | 0.00 | | |
| 80.271 | 0.55 | 0.57 | 0.66 | 0.55 | 0.29 | 0.16 | 0.00 | 0.36 | 0.24 | 0.00 | | |
| 84.750 | 1.00 | 1.00 | 1.00 | 1.00 | 0.24 | 0.16 | 1.00 | 0.29 | 0.21 | 1.00 | | |
| 87.354 | 0.88 | 0.96 | 0.89 | 0.96 | 0.26 | 0.15 | 0.75 | 0.32 | 0.21 | 0.94 | | |
| 93.708 | 0.66 | 0.80 | 0.74 | 0.79 | 0.27 | 0.14 | 0.39 | 0.35 | 0.21 | 0.67 | | |
| 104.229 | 0.54 | 0.66 | 0.64 | 0.63 | 0.25 | 0.12 | 0.24 | 0.32 | 0.20 | 0.44 | | |
| 113.604 | 0.49 | 0.60 | 0.60 | 0.57 | 0.24 | 0.12 | 0.20 | 0.31 | 0.19 | 0.36 | | |
| 124.125 | 0.45 | 0.54 | 0.54 | 0.51 | 0.22 | 0.11 | 0.16 | 0.28 | 0.18 | 0.30 | | |
| 134.125 | 0.41 | 0.50 | 0.46 | 0.46 | 0.21 | 0.11 | 0.14 | 0.23 | 0.17 | 0.25 | | |
| 143.500 | 0.38 | 0.46 | 0.43 | 0.42 | 0.20 | 0.11 | 0.12 | 0.22 | 0.17 | 0.22 | | |
| 153.708 | 0.36 | 0.44 | 0.42 | 0.39 | 0.19 | 0.10 | 0.11 | 0.22 | 0.16 | 0.20 | | |
| 161.417 | 0.34 | 0.41 | 0.39 | 0.37 | 0.18 | 0.10 | 0.10 | 0.21 | 0.15 | 0.19 | | |
| 172.042 | 0.33 | 0.39 | 0.38 | 0.35 | 0.17 | 0.09 | 0.10 | 0.20 | 0.15 | 0.17 | | |
| 181.208 | 0.31 | 0.38 | 0.36 | 0.33 | 0.16 | 0.09 | 0.09 | 0.19 | 0.14 | 0.16 | | |
| 191.208 | 0.30 | 0.36 | 0.34 | 0.32 | 0.15 | 0.08 | 0.08 | 0.17 | 0.13 | 0.15 | | |
| 204.125 | 0.22 | 0.26 | 0.24 | 0.21 | 0.12 | 0.07 | 0.07 | 0.12 | 0.10 | 0.10 | | |

Table 20. Suction side vane small grid far turbulence condition data, $Re_C$ = 1,000,000.

| Small Grid Far | | | | | | | | | |
|---|---|---|---|---|---|---|---|---|---|
| | η | | | | | | | | |
| ReC | 2000827.67 | 2000089.67 | 1999918.33 | 2000698.17 | 2000425.00 | 2001186.00 | 1999908.33 | | |
| SS1 | 0.50 | 0.50 | 0.50 | 0.00 | 0.00 | 0.00 | 0.00 | | |
| SS2 | 0.15 | 0.30 | 0.00 | 0.15 | 0.00 | 0.30 | 0.00 | | |
| SS3 | 0.15 | 0.30 | 0.00 | 0.00 | 0.15 | 0.00 | 0.30 | | |
| Tu | 0.035 | 0.035 | 0.035 | 0.035 | 0.035 | 0.035 | 0.035 | | |
| File name | BRS1R2SG | BRS2R2SG | BRS5R2SG | BRS6R2SG | BRS7R2SG | BRS9R2SG | BRSZR2SG | | |
| dist/slot height (X/S) | SG, Tu=3.5%, SS1=0.5, SS2=0.15, SS3=0.15, ReC=2000828 | SG, Tu=3.5%, SS1=0.5, SS2=0.3, SS3=0.3, ReC=2000090 | SG, Tu=3.5%, SS1=0.5, SS2=0, SS3=0, ReC=1999918 | SG, Tu=3.5%, SS1=0, SS2=0.15, SS3=0, ReC=2000698 | SG, Tu=3.5%, SS1=0, SS2=0, SS3=0.15, ReC=2000425 | SG, Tu=3.5%, SS1=0, SS2=0.3, SS3=0, ReC=2001186 | SG, Tu=3.5%, SS1=0, SS2=0, SS3=0.3, ReC=1999908 | | |
| 0.000 | 1.00 | 1.00 | 1.00 | 0.00 | 0.00 | 0.00 | 0.00 | | |
| 1.000 | 0.92 | 0.93 | 0.92 | 0.00 | 0.00 | 0.00 | 0.00 | | |
| 5.375 | 0.74 | 0.74 | 0.73 | 0.00 | 0.00 | 0.00 | 0.00 | | |
| 8.292 | 0.70 | 0.73 | 0.66 | 0.00 | 0.00 | 0.00 | 0.00 | | |
| 14.125 | 1.00 | 1.00 | 0.61 | 1.00 | 0.00 | 1.00 | 0.00 | | |
| 16.625 | 0.96 | 0.97 | 0.55 | 0.85 | 0.00 | 0.99 | 0.00 | | |
| 22.354 | 0.81 | 0.91 | 0.51 | 0.49 | 0.00 | 0.80 | 0.00 | | |
| 32.458 | 0.70 | 0.78 | 0.46 | 0.31 | 0.00 | 0.56 | 0.00 | | |
| 43.292 | 0.62 | 0.69 | 0.41 | 0.24 | 0.00 | 0.43 | 0.00 | | |
| 52.458 | 0.56 | 0.63 | 0.38 | 0.21 | 0.00 | 0.38 | 0.00 | | |
| 62.875 | 0.52 | 0.58 | 0.35 | 0.18 | 0.00 | 0.33 | 0.00 | | |
| 73.292 | 0.48 | 0.54 | 0.32 | 0.16 | 0.00 | 0.29 | 0.00 | | |
| 80.271 | 0.53 | 0.58 | 0.30 | 0.14 | 0.00 | 0.27 | 0.00 | | |
| 84.750 | 1.00 | 1.00 | 0.27 | 0.11 | 1.00 | 0.21 | 1.00 | | |
| 87.354 | 0.88 | 0.98 | 0.28 | 0.13 | 0.80 | 0.23 | 0.96 | | |
| 93.708 | 0.66 | 0.84 | 0.28 | 0.13 | 0.42 | 0.24 | 0.71 | | |
| 104.229 | 0.54 | 0.70 | 0.26 | 0.12 | 0.26 | 0.23 | 0.49 | | |
| 113.604 | 0.50 | 0.64 | 0.25 | 0.12 | 0.21 | 0.21 | 0.39 | | |
| 124.125 | 0.45 | 0.58 | 0.23 | 0.11 | 0.17 | 0.20 | 0.32 | | |
| 134.125 | 0.41 | 0.53 | 0.21 | 0.10 | 0.14 | 0.19 | 0.28 | | |
| 143.500 | 0.39 | 0.50 | 0.20 | 0.10 | 0.12 | 0.18 | 0.24 | | |
| 153.708 | 0.37 | 0.47 | 0.19 | 0.09 | 0.11 | 0.17 | 0.22 | | |
| 161.417 | 0.35 | 0.45 | 0.18 | 0.09 | 0.10 | 0.17 | 0.20 | | |
| 172.042 | 0.33 | 0.43 | 0.16 | 0.08 | 0.09 | 0.15 | 0.18 | | |
| 181.208 | 0.32 | 0.41 | 0.17 | 0.08 | 0.09 | 0.15 | 0.18 | | |
| 191.208 | 0.31 | 0.39 | 0.16 | 0.08 | 0.09 | 0.15 | 0.17 | | |
| 204.125 | 0.21 | 0.26 | 0.11 | 0.05 | 0.06 | 0.10 | 0.11 | | |

Appendix E

**Uncertainty Calculations.** Uncertainty estimates for this study were done using the root sum square method shown by Moffat [53]. These uncertainties arise from several possible sources of error in data acquisition equipment, procedure, and fabrication error. All uncertainties were calculated with 95% confidence interval.

**Pressure Side Vane.** The blowing ratio ($M_{PS1}$) uncertainty incorporated the individual uncertainties in flow rate, local velocity and slot height that were 2%, 2.5%, and 2.5%, respectively. The given uncertainty including these factors is 4% at an average blowing ratio of $M_{PS1} = 0.7$ and a nominal exit chord Reynolds number of $Re_C = 1{,}000{,}000$. About +/- 5% blowing ratio uncertainty is estimated at the lowest Reynolds number. The film cooling effectiveness ($\eta$) uncertainty ranged from +/- 0.08 at the highest two blowing ratios to +/- 0.05 at the lowest blowing ratio. The local spanwise averaged effectiveness uncertainty was projected employing a sparse array that included a +/- 0.2 C uncertainty in local temperature measurements.

**Suction Side Vane.** The local streamwise film cooling effectiveness uncertainty results is taken as the lesser of +/- 0.05 or +/- 8% with the exception of the highest blowing ratio for the small grid far turbulence condition in which the lesser of +/- 0.08 or +/-10% is taken for the near slot uncertainty because of the variation in spanwise data. The blowing ratio uncertainties ($M_{SS1}$, $M_{SS2}$ and $M_{SS3}$) were approximated at +/- 4%, +/- 4% , and +/- 5% at the 2,000,000, 1000,000,000 and 5000,000 Reynolds numbers, respectively.

Appendix F

**Full Surface Plots.** IR camera data was processed to produce the following images. Room temperatures were monitored. For large variations in surrounding room temperature, the radiation heat transfer was accounted for using Eq. 2.

$$T_{target} = \sqrt[4]{\frac{\left(T_{Sensor}^4 - (1-\varepsilon) * T_{background}^4\right)}{\varepsilon}} \quad \text{Eq. 2}$$

Where: $T_{backround}$ = room temperature and $\varepsilon = 0.94$ (paint, flat, black)

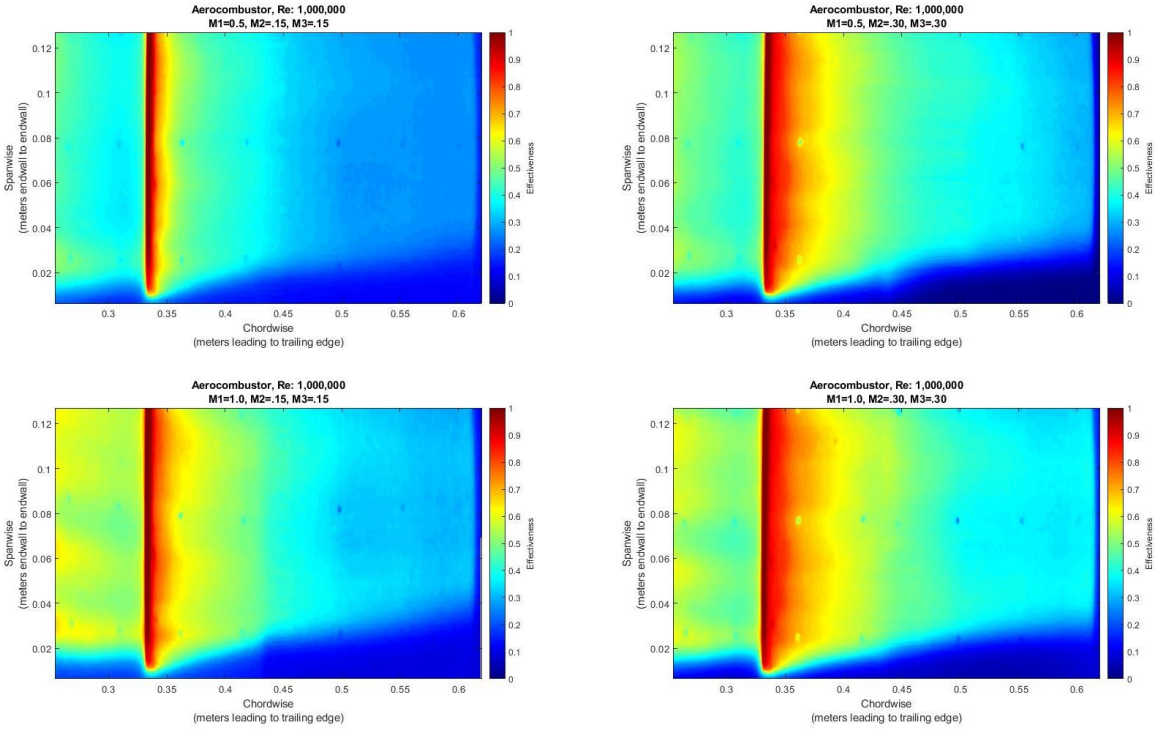


Figure 89. Contour plots of integrated suction surface film cooling for the AC turbulence condition at $Re_C$ = 1,000,000.

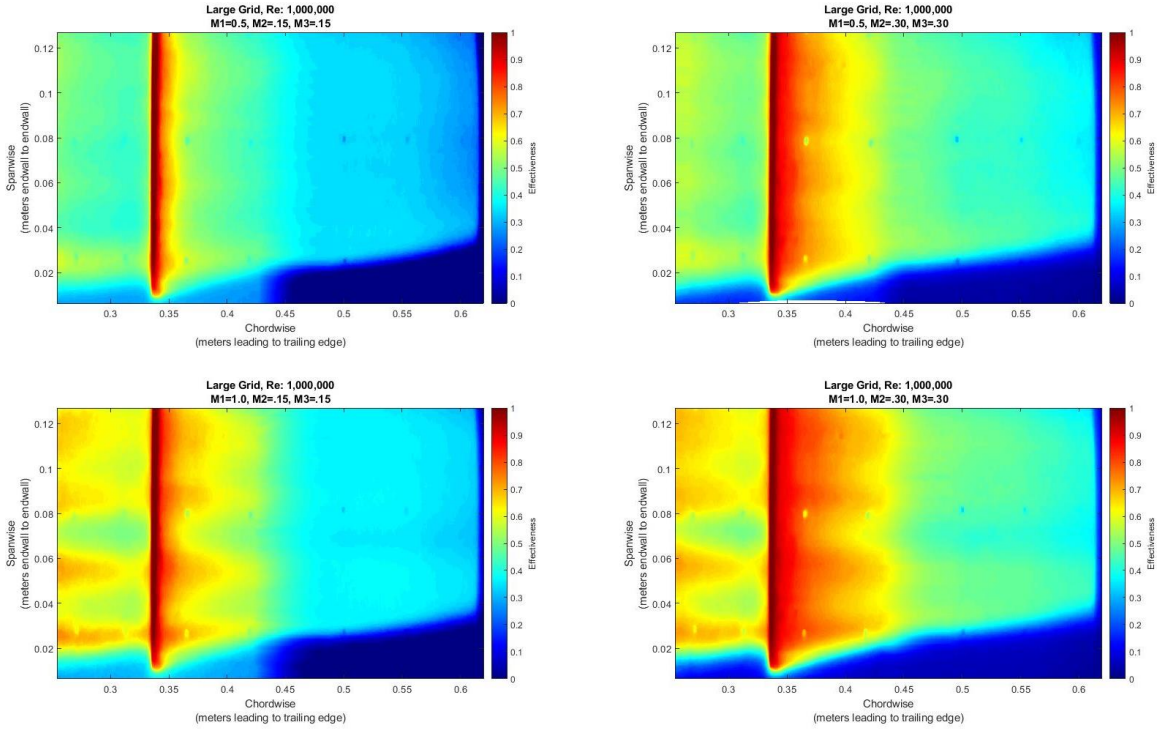


Figure 90. Contour plots of integrated suction surface film cooling for the LG turbulence condition at $Re_C$ = 1,000,000.

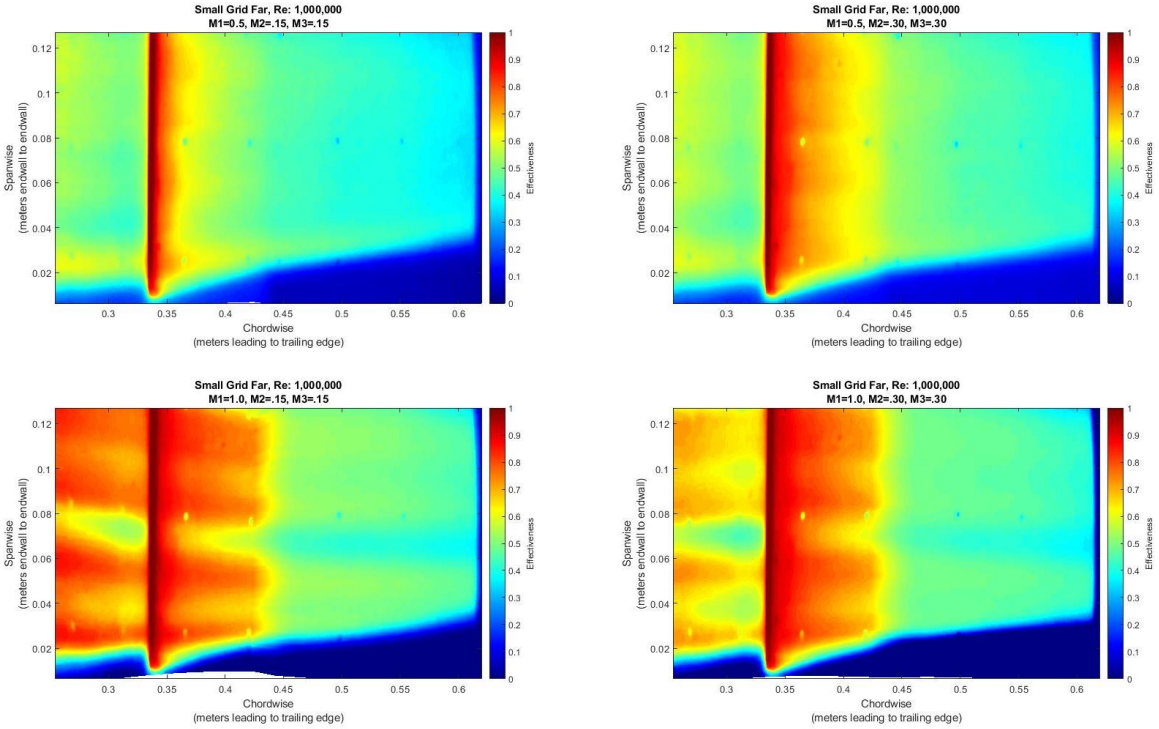


Figure 91. Contour plots of integrated suction surface film cooling for the SGF turbulence condition at $Re_C$ = 1,000,000.

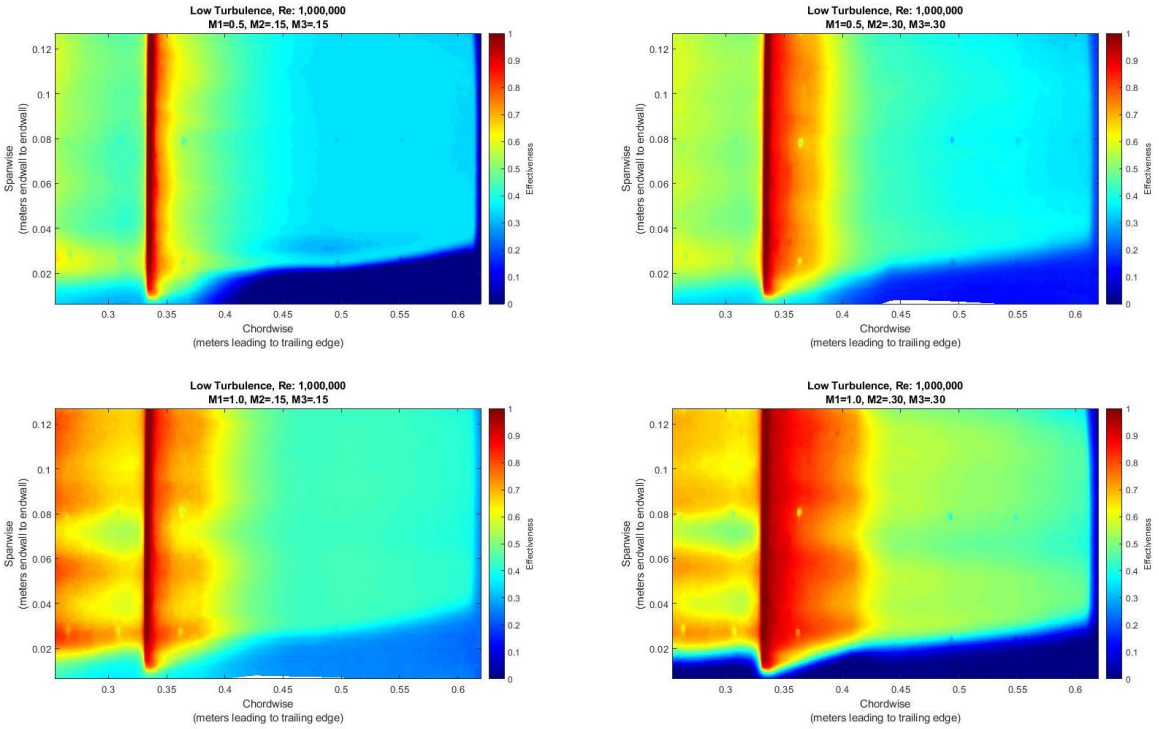


Figure 92. Contour plots of integrated suction surface film cooling for the LT turbulence condition at $Re_C$ = 1,000,000.

# REFERENCES


[1] M. L. Busche, J. Kingery and F. E. Ames, "Slot Film Cooling in an Accelerating Boundary Layer with High Free-stream Turbulence," ASME Paper No. GT2014-25360, 2014.

[2] J. P. Bons, Cooling Strategies for Vane Leading Edges in a Syngas Environment Including Effects of Deposition and Turbulence, Columbus: Department of Energy/National Energy Technology Laboratory, 2015.

[3] J. W. Varty and F. E. Ames, "Experimental Heat Transfer Distributions Over An Aft Loaded Vane With a Large Leading Edge At Very High Turbulence Levels," ASME Paper No. IMECE2016-67029, 2016.

[4] Y. Kanani, S. Acharya and F. Ames, Simulations of Slot Film-Cooling with Freestream Acceleration and Turbulence, Proceedings of ASME Turbo Expo, ASME Paper No. GT2017-65050, 2017.

[5] J. E. Bruce-Black, D. G. Bogard, F. T. Davidson and D. R. Johns, "Practical Slot Configurations for Turbine Film Cooling Applications," ASME Paper No. GT2009-59674, 2009.

[6] R. S. Bunker, "A Study of Mesh-Fed Slot Film Cooling," *J. Turbomachinery,* vol. 133, pp. 1-11., 2011.

[7] F. F. Simon, "Jet Model for Slot Film Cooling with Effect of Free-Steam and Coolant Trubulence," NASA Technical Paper No. 2655, pp. 1-18, 1986.

[8] M. L'Ecuyer and F. Soechting, "A Model for Correlating Flat Plate Film Cooling Effectiveness for Rows of Round Holes," in *Heat Transfer and Cooling in Gas Turbines: AGARD Conference Proceedings No. 390,* 1985.

[9] D. R. Pederson, E. R. G. Eckert and R. J. Goldstein, "Film Cooing with Large Density Differences Between the Mainstream and the Secondary Fluid Measured by the Heat-Mass Transfer Analogy," *J. Heat Transfer,* vol. 99, pp. 620-627, 1977.

[10] A. K. Sinha, D. Bogard and M. E. Crawford, "Film Cooling Effectiveness Downstream of a Single Row of Holes with Variable Density Ratio," ASME Paper No. 90-GT-43, 1990.

[11] K. Liu, S. Yang and J. Han, "Influence of Coolant Density on Turbine Blade Film Cooling with Compound Angle Shaped Holes," ASME Paper No. GT2012-69117, 2012.

[12] N. W. Foster and D. Lampard, "The Flow and Film Cooling Effectiveness Following Injection through a Row of Holes," *J. Eng. Gas Turbines Power,* vol. 102, pp. 584-588, 1980.

[13] C. Leiss, "Experimental Investigation of Film Cooling with Ejection from a Row of Holes for the Application to Gas Turbine Blades," *J. Eng. Gas Turbines Power, v. 97, pp. 21-27.,* vol. 97, pp. 21-27, 1975.

[14] Y. Qin, J. Ren and H. Jiang, "Effects of Streamwise Pressure Gradient and Convex Curvature on Film Cooling Effectiveness," ASME Paper No. GT2014-25808, 2014.

[15] J. F. Muska, R. W. Fish and M. Suo, "The Additive Nature of Film Cooling from Rows of Holes," *J. Eng. Gas Turbines Power,* vol. 94, pp. 457-463, 1976.

[16] J. E. Kingery and F. E. Ames, Full Coverage Shaped-Hole Film Cooling in an Accelerating Boundary Layer With High Freestream Turbulence, Journal of Turbomachinery v. 138, July, 2016.

[17] B. Laveau and R. Abhari, "Influence of Flow Structure on Shaped Hole Film Cooling Performance," ASME Paper No. GT2010-23032, 2010.

[18] R. S. Bunker, "A Review of Shaped Hole Turbine Film Cooling Technology," *J. Heat Transfer,* vol. 127, pp. 441-453, 2005.

[19] R. S. Bunker, "Film Cooling: Breaking the Limits of Diffusion Shaped Holes," *Heat Transfer Research,* vol. 41, pp. 627-650, 2010.

[20] J. Dittmar, A. Schulz and S. Witting, "Assessment of Various Film Cooling Configurations Including Shaped and Compound Angle Holes Based on Large-Scale Experiments," *J. Turbomachinery,* vol. 125, pp. 57-64, 2003.

[21] C. Saumweber and A. Schulz, "Effect of Geometry Variations on the Cooling Performance of Fan-Shaped Cooling Holes," *J. Turbomachinery,* vol. 134, pp. 1-16, 2012.

[22] Y. Yu, C.-H. Yen, T.-P. Shih, M. K. Chyu and S. Gogieni, "Film Cooling Effectiveness and Heat Transfer Coefficient Distribution Around Diffusion Shaped Holes," *J. Heat Transfer*, vol. 124, pp. 820-827, 2002.

[23] W. Colban, K. Thole and M. Haendler, "A Comparison of Cylindrical and Fan-Shaped Film Cooling Holes on a Vane Endwall at Low and High Free-Stream Turbulence Levels," ASME Paper No. GT2006-90021, 2006.

[24] C. Saumweber and A. Schulz, "Interaction of Film Cooling Rows: Effects of Hole Geometry and Row Spacing on the Cooling Performance Downstream of the Second Row of Holes," *J. Turbomachinery*, vol. 126, pp. 237-246, 2004.

[25] D. Brauckmann and J. Von Wolfersdorf, "Influence of Compound Angle on Adiabatic Film Cooling Effectiveness and Heat Transfer Coefficient for a Row of Shaped Film Cooling Holes," ASME Paper No. GT2005-68036, 2005.

[26] W. Colban, A. Gratton, K. Thole and M. Haendler, "Heat Transfer and Film Cooling Measurements on a Stator Vane with Fan-Shaped Cooling Holes," ASME Paper No. GT2005-68258, 2005.

[27] S. Mhetras, J. Han and R. Rudolph, "Film Cooling Effectiveness from Shaped Film Cooling Holes for a Gas Turbine Blade," ASME Paper No. GT2008-50916, 2008.

[28] R. P. Schroeder and K. Thole, "Adiabatic Effectiveness Measurements for a Baseline Shaped Film Cooling Hole," ASME Paper No. GT2014-25992, 2014.

[29] C. Saumweber, A. Schulz and S. Wittig, "Free-Stream Turbulence Effects on Film Cooling with Shaped Holes," *J. Turbomachinery*, vol. 125, pp. 65-73, 2003.

[30] C. Saumweber and A. Schulz, "Free-Stream Effects on the Cooling Performance of Cylindrical and Fan-Shaped Cooling Holes," *J. Turbomachinery*, vol. 134, pp. 1-12, 2012.

[31] J. E. Mayhew, J. W. Baughn and A. R. Byerley, "The Effect of Free-Stream Turbulence on Film Cooling Adiabatic Effectiveness," ASME Paper No. GT2002-30172, 2002.

[32] J. E. Mayhew, J. W. Baughn and A. R. Byerley, "The Effect of Free-Stream Turbulence on Film Cooling Heat Transfer," ASME Paper No. GT2002-30173, 2002.

[33] F. E. Ames, "Aspects of Vane Film Cooling with High Turbulence: Part I-Heat Transfer," *J. Turbomachinery,* vol. 120, pp. 768-776, 1998.

[34] F. E. Ames, "Aspects of Vane Film Cooling with High Turbulence: Part II-Adiabatic Effectiveness," *J. Turbomachinery,* vol. 120, pp. 777-784., 1998.

[35] J. M. Cutbirth and D. G. Bogard, "Evaluation of Pressure Side Film Cooling with Flow and Thermal Field Measurements—Part II: Turbulence Effects," *J. Turbomachinery,* vol. 124, pp. 678-685, 2002.

[36] J. E. Mayhew, J. W. Baughn and A. R. Byerley, "The Effect of Free-Stream Turbulence on Film Cooling Heat Transfer Coefficient and Adiabatic Effectiveness using Compound Angle Holes," ASME Paper No. GT2004-53230, 2004.

[37] M. W. Wright, S. T. McClain and M. D. Clemenson, "PIV Investigation of the Effect of Free-Stream Turbulence Intensity on Film Cooling from Fan-Shaped Holes," ASME Paper No. GT2011-46127, 2011.

[38] F. T. Davidson, J. E. Bruce-Black, D. G. Bogard and D. R. Johns, "Adiabatic Effectiveness on the Suction Side of a Turbine Vane and the Effects of Curvature at the Point of Injection," ASME Paper No. GT2008-51350, 2008.

[39] J. E. Kingery, "An Experimantal Investigation into the Effects of High Freestream Turbulence on Full Coverage Shaped Hole Film Cooling in An Accelerating Boundary Layer," University of North Dakota, Grand Forks, 2015.

[40] M. L. Busche, "Experimental Investigation of the Effect of Turbulence on Slot-Fed Film Cooling Adiabatic Effectiveness and Downstream Heat Transfer," University of North Dakota, Grand Forks, ND, 2013.

[41] J. Varty, "Experimental Heat Transfer Distribution Over and Aft Loaded Vane With A Large Leading Edge at Very High Trubulence Levels," University of North Dakota, Grand Forks, 2016.

[42] I. Jaswal, "Aerodynamic Losses and Heat Transfer for a Covered Trailing Edge Turbine Vane with a High Solidity Low Pressure Drop Pedestal Pin Fin Array and Variable Coolant Ejection," University of North Dakota, Grand Forks, ND, 2008.

[43] I. Jaswal, "Aerodynamic Losses and Heat Transfer for a Covered Trailing Edge Turbine Vane with a High Solidity Low Pressure Drop Pedestal Pin Fin Array and Variable Coolant Ejection," University of North Dakota, 2008, 2008.

[44] J. E. Kingery and F. E. Ames, "Stagnation Region Heat Transfer Augmentation at Very High Turbulence Levels," ASME Paper No. GT2015-42420, 2015.

[45] L. W. Soma and F. E. Ames, "The Influence of Turbulence and Reynolds numb on Multiple Slot Film Colling Over Suction Surface," ASME, Proceeding of ASMETurbo Expo, London, England (Cancled due to COVID19), 2020.

[46] J. A. Kingerly, F. E. Ames, J. Downs, S. Acharya and B. J. Barler, "An Analysis of a Deposition Toleran Colling Approach for Nozzle Guide Vanes," in *ASME Paper No. GT2015-42419*, 2015.

[47] A. A. Shiekhmohamed, L. W. Soma, F. E. Ames and S. Acharya, "Heat Transfer and Pressure Drop Measurements in a High Solidity Pin Fin Array with Variable Hole Size Incremental Impingement," in *ASME Paper No. GT2017-65046*.

[48] M. L. Busche, L. P. Moualeu, C. Tang and F. E. Ames, "Heat Transfer and Pressure Drop Measurements in High Solidity Pin Fin Cooling Arrays with INcremental Replenishment," *ASME J. Turbomachinery,* vol. 135, pp. 041011-1-9, 2013.

[49] J. W. Varty, L. W. Soma, F. E. Ames and S. Acharya, "Vane Suction Surgace Heat Transfer in Regions of Secondary Flow: The Infuence of Turbulence Level, Reynolds number and Endwall Boundary Condition," *ASME. J. Turbomachinery,* 2017.

[50] R. J. Goldstein and A. Haji-Sheikh, "A Prediction of Film Cooling Effectiveness," JSME, Seimi-Internation Symposium, Tokyo, 1967.

[51] C. H. Sieverding, "Recent Progress in the Understanding of Basic Aspects of Secondary Flows in Turbine Blade Passages," *Journal of Engineering for Gas Turbines and Power,* vol. 107, pp. 248-257, 1984.

[52] L. S. Langston, M. L. Nice and R. M. Hooper, "Three-dimensional Flow Within a Turbine Cascade Passage," *ASME Journal of Engineering for Power,* pp. 21-28, January, 1977.

[53] R. J. Moffat, "Describing the Uncertainties in Experimental Results," *Experimental Thermal and Fluid Science,* vol. 1, pp. 3-17, 1988.

[54] J. P. Downs and K. K. Landis, "Turbine Cooling Systems Design—Past, Present and Future," ASME Paper No. GT2009-59991, 2009.

[55] N. Sundaram and K. A. Thole, "Effects of Surface Deposition, Hole Blockage, and TBC Spallation on Vane Endwall Film Cooling," ASME Paper No. GT2006-90379., 2006.

[56] P. Gandavarapu, "The Influence of High Turbulence Intensity and Large Leading Edge Reynolds Numbers on Stagnation Region Heat Transfer," University of North Dakota, Grand Forks, ND, 2011.

[57] N. K. Chowdhury and F. E. Ames, "The Response of High Intensity Turbulence in the Presence of Large Stagnation Regions," ASME Paper No. GT2013-95055, 2013.

[58] W. Kays, M. Crawford and B. Weigand, Convective Heat and Mass Transfer, New York: McGraw-Hill, pp. 546, 2005.

[59] F. E. Ames and R. J. Moffat, "Heat Transfer with High Intensity, Large Scale Turbulence: The Flat Plate Turbulent Boundary Layer and the Cylindrical Stagnation Point," Stanford University, Palo Alto, CA., 1990.

[60] L. W. Soma, F. E. Ames and S. Acharya, "Heat Transfer and Pressure Drop in a Converging Pedestal Array with Exit Area Variation," in *ASME Paper No. GT2018-75578*, 2018.

[61] P. Evenson, "Calculation of Multiple Regression with Three Independent Variables Using a Programable Pocket Calculator," Agricultural Experiment Station Technical Bulletins. 55, South Dakota State University, 1978.